
Laser ion acceleration from a double-layer metal foil

Laser-Ionenbeschleunigung aus einer metallischen Folie

Zur Erlangung des Grades eines Doktors der Naturwissenschaften (Dr. rer. nat.)

genehmigte Dissertation von M.Sc. Zsolt Lécz aus Székelyhíd, Rumänien

March, 2013 – Darmstadt – D 17



TECHNISCHE
UNIVERSITÄT
DARMSTADT

Fachbereich Elektrotechnik und Infor-
mationstechnik
Institut für Theorie Elektromagnetischer
Felder

Laser ion acceleration from a double-layer metal foil
Laser-Ionenbeschleunigung aus einer metallischen Folie

Genehmigte Dissertation von M.Sc. Zsolt Lécz aus Székelyhíd, Rumänien

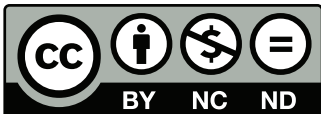
1. Gutachten: Prof. Dr. rer. nat. Oliver-Boine Frankenheim
2. Gutachten: Prof. Dr. Markus Roth

Tag der Einreichung: 14. May, 2013
Tag der Prüfung: 30. September, 2013

Darmstadt – D 17

Bitte zitieren Sie dieses Dokument als:
URN: urn:nbn:de:tuda-tuprints-urn:nbn:de:tuda-tuprints-33359
URL: <http://tuprints.ulb.tu-darmstadt.de/3335>

Dieses Dokument wird bereitgestellt von tuprints,
E-Publishing-Service der TU Darmstadt
<http://tuprints.ulb.tu-darmstadt.de>
tuprints@ulb.tu-darmstadt.de



Die Veröffentlichung steht unter folgender Creative Commons Lizenz:
Namensnennung – Keine kommerzielle Nutzung – Keine Bearbeitung 2.0 Deutschland
<http://creativecommons.org/licenses/by-nc-nd/2.0/de/>

Erklärung zur Dissertation

Hiermit versichere ich, die vorliegende Dissertation ohne Hilfe Dritter nur mit den angegebenen Quellen und Hilfsmitteln angefertigt zu haben. Alle Stellen, die aus Quellen entnommen wurden, sind als solche kenntlich gemacht. Diese Arbeit hat in gleicher oder ähnlicher Form noch keiner Prüfungsbehörde vorgelegen.

Darmstadt, den 12. November 2013

(Zsolt Léczy)

Abstract

The laser-ion acceleration with ultra-intense and ultra-short laser pulses has opened a new field of accelerator physics over the last decade. Fast development in laser systems are capable of delivering short pulses of a duration of a few hundred femtoseconds at intensities between $10^{18} - 10^{20}$ W/cm². At these high intensities the laser-matter interaction induces strong charge separation, which leads to electric fields exceeding the acceleration gradients of conventional devices by 6 orders of magnitude. The particle dynamics and energy absorption of the laser pulse can be understood by means of high-performance simulation tools.

In the framework of the LIGHT (Laser Ion Generation, Handling and Transport) project our goal is to provide an analytical description of the 3D distribution of the protons accelerated via TNSA (Target Normal Sheath Acceleration). In this acceleration mechanism the short pulse impinging on a metal foil heats the electrons to relativistic energies, which triggers the strong charge separation field on the opposite target surface (Debye-sheath). The accelerated light ions (proton, carbon, oxygen) observed in the experiments originate from the contamination layer deposited on the surface. The thickness of this layer in the experiments is not known exactly. According to our study these ions can be accelerated in three different regimes depending on layer thickness: quasi-static acceleration (QSA, for thin layers), plasma expansion (for thick layers) and a not well understood intermediate (or combined) regime.

In a laser-plasma simulations time-dependent hot electron density and temperature are observed, therefore we performed plasma simulations with a well defined and constant initial hot electron distribution. Thus the simulation results are easier to compare with analytical models. In our case the theoretical investigation of the TNSA involves the understanding of the charge separation effects at the surface of a two-temperature plasma and the consequent proton acceleration in one dimension. We omit the detailed dynamics of the laser-plasma interaction by assuming a preheated electron distribution. With our 1D electrostatic simulations we investigate the influence of the proton layer thickness on the TNSA energy spectrum. Additionally we investigate the divergence of the protons using 2D simulations: In these we simulate the heating of the electrons by the laser pulse.

Numerical studies in this work were carried out using a Particle-in-Cell (PIC) plasma simulation code (VORPAL). The target is defined as a single-ionized plasma with a double-layer structure: a bulk layer of heavy ions, which represents the metal foil itself and a much thinner proton layer, which serves as the contamination layer. The layer is considered thin if it is thinner compared to the skin depth of the accelerating electric field. For a thin proton layer the quasi-static acceleration is the governing mechanism. When the proton layer is larger than skin depth the process can be described as plasma expansion.

I found that the energy and phase-space distribution of the protons strongly depends on the layer thickness. In the QSA regime the proton spectrum shows a nearly mono-energetic feature, but the maximum energy is typically low compared to the plasma expansion regime, where the protons have a broad exponential energy spectrum. For the plasma expansion we observe a cut-off energy that logarithmically depends on the acceleration time.

The simulation results in these two extreme cases for one- and two-temperature plasmas have been extensively compared to analytical predictions showing an overall good agreement. In the intermediate regime an analytical expression could be obtained for the energy conversion from electrons to protons as a function of electron parameters and layer thickness. By changing the layer thickness a smooth transition between the two extreme cases could be identified.

The proton layer thickness also has an impact on the transversal acceleration, which defines the divergence of a proton beam. In the two-dimensional TNSA simulations a laser pulse is needed to generate the hot electron population in the plasma. The simulations show that theoretically with the right laser pulse duration and layer thickness the divergence of the most energetic protons can be reduced almost to zero. In the QSA regime the transversal distribution and temperature of the hot electrons changes too quickly compared to the time-scale of the acceleration. The analytical treatment of the divergence is only possible for the thick layers, where the plasma expansion model is suitable to describe the physics. The model derived in this work can be used to reconstruct the whole velocity phase-space of the protons in 3D. Therefore it enables us to perform particle tracking and beam optics simulations with realistic TSNA proton bunch. The envelope angle of the protons measured in experiments can be also reproduced using our 2D model.

The beam quality during motion through magnetic focusing and energy selection systems downstream of the laser acceleration is sensitive to the initial distribution. After benchmarking our analytic models, simulation results and measurements with each another, we are confident we can now provide sufficiently realistic particle distributions to be expected a few mm from the target in TNSA. Using our particle distributions as input, the effect of co-moving electrons, the degradation of the transverse emittance and chromatic aberration effects can be investigated. Thereby this study hopefully contributes to the goal of the Light project: Coupling the new laser ion acceleration techniques to conventional accelerator facilities.

Kurzfassung

In den letzten Jahren wurde die Laserionenbeschleunigung mit hochintensiven ultrakurzen Laserpulsen zu einer neuen Technik in der Beschleunigerphysik. Die sich zur Zeit schnell weiterentwickelnden Lasersysteme ermöglichen Pulslängen von wenigen hundert Femtosekunden mit Intensitäten von $10^{18} - 10^{20} \text{ W/cm}^2$. Solch hohe Intensitäten erzeugen bei der Interaktion mit Materie für eine starke Ladungstrennung. Die dadurch erzeugten elektrischen Felder übersteigen die in konventionellen Beschleunigern genutzten um sechs Größenordnungen. Die Teilchendynamik während der Absorption des Laserpulses kann mithilfe von leistungsfähigen Computersimulationen untersucht werden.

Ein Ziel des LIGHT Projekts (Laser Ion Generation, Handling and Transport) ist die analytische Beschreibung des sechsdimensionalen Phasenraumes und der dreidimensionalen Dichteverteilung der von durch Target Normal Sheath Acceleration (TNSA) beschleunigten Protonen. Bei TNSA wird ein kurzer Laserpuls auf eine Metallfolie fokussiert. Dabei erreichen die Elektronen relativistische Energien. Dies wiederum erzeugt ein starkes Ladungsseparationsfeld auf der gegenüberliegenden Targetseite (Debye-sheath). Die dabei beschleunigten leichten Ionen stammen aus einer Kontaminationsschicht auf der Targetoberfläche. Die Dicke der Kontaminationsschicht ist nicht genau bekannt. Unsere Studien zeigen, dass die Ionenbeschleunigung in drei verschiedenen Regimes beschrieben werden kann: Quasistatische Beschleunigung (QSA) für dünne Schichten, Plasmaexpansion für dicke Schichten und ein Zwischenzustand.

In Laser Plasma Simulationen werden zeitabhängige Dichten und Temperaturen der heißen Elektronen beobachtet. Wir führen Plasma Simulationen mit einer anfänglich konstanten Verteilung der heißen Elektronen durch, da diese sich leichter mit analytischen Modellen vergleichen lässt. Um TNSA theoretisch behandeln zu können müssen wir die Ladungsseparationseffekte an der Oberfläche eines Zweitemperaturplasmas und die daraus folgende Protonenbeschleunigung beschreiben. Zunächst nehmen wir statt einer Simulation der vollen Laser-Plasma-Wechselwirkung ein bereits geheiztes Plasma als Ausgangspunkt der 1D-Simulation an. Wir untersuchen nun mithilfe elektrostatischer 1D-Simulationen den Einfluss der Protonenschichtdicke auf das Protonenspektrum nach der TNSA. Des Weiteren betrachten wir die Divergenz der beschleunigten Protonen mithilfe von 2D-Simulationen.

Die numerischen Studien für diese Arbeit wurden mithilfe des Particle-in-Cell (PIC) Plasmasimulationscodes VORPAL durchgeführt. Dabei wurde das Target als einfach ionisiertes Plasma in zwei Schichten ausgeführt: Die Metallfolie durch eine Schicht schwerer Ionen und die Kontaminationsschicht durch eine dünne Protonenschicht. Im Folgenden sprechen wir von einer dünnen Protonenschicht, wenn ihre Dicke die Skintiefe des beschleunigenden elektrischen Feldes deutlich unterschreitet. Für eine dünne Protonenschicht ist QSA der primäre Beschleunigungsmechanismus. Für eine Dicke Protonenschicht kann die Beschleunigung als Plasmaexpansion beschrieben werden.

Unsere Ergebnisse zeigen, dass die Energie- und Phasenraumverteilung der Protonen stark von der Schichtdicke abhängt. Für QSA ist das Spektrum fast monoenergetisch, dabei ist jedoch die Maximalenergie deutlich niedriger als für die Plasmaexpansion. Für die Plasmaexpansion erhalten wir ein exponentiell abfallendes Energiespektrum, das bei einer logarithmisch von der Beschleunigungszeit abhängenden Maximalenergie begrenzt ist. Die Simulationsergebnisse für diese beiden Extremfälle von Ein- und Zweitemperaturplasmas wurden mit analytischen Vorhersagen verglichen und zeigen gute Übereinstimmung. Für den Zwischenzustand konnte ein

Analytischer Ausdruck in Abhängigkeit der Schichtdicke und der Elektronenparameter für die Energieübertragung von Elektronen zu Protonen gefunden werden. Durch die Änderung der Schichtdicke konnte ein reibungsloser Übergang zwischen den beiden Extremfällen identifiziert werden.

Auch die transversale Komponente der Beschleunigung und damit die Divergenz des Protonenstrahls wird von der Protonenschichtdicke bestimmt. In der zweidimensionalen TNSA Simulation wird ein Laserpuls benötigt, um die heißen Elektronen im Plasma zu erzeugen. Die Simulationen zeigen, dass durch Wahl der richtigen Laserpulsdauer und Schichtdicke die Divergenz der schnellsten Protonen theoretisch auf nahezu Null reduziert werden kann. Leider kann in der Praxis die Schichtdicke nicht präzise kontrolliert werden. Verglichen mit der Zeitskala der Beschleunigung, ändert sich die Verteilung und Temperatur der heißen Elektronen zu schnell.

Die Divergenz kann für dicke Schichten auch analytisch bestimmt werden. Dafür wird der Prozess physikalisch als Plasmaexpansion modelliert. Das hierzu entwickelte Modell kann verwendet werden, um den ganzen 3D-Geschwindigkeitsphasenraum der Protonen zu beschreiben. Es erlaubt so Partikeltracking und Strahloptiksimulationen für einen realistischen TNSA Protonenpaket. Der Enveloppenwinkel von Protonen aus Messungen stimmt mit unserem 2D-Modell überein.

Der Transfer des Strahls durch magnetische Fokussierungs- und Energieselektionssysteme hängt empfindlich von der Anfangsverteilung der Teilchen ab. Nachdem wir unsere analytischen- und Simulationsmodelle miteinander und mit Messungen verglichen haben, sind wir zuversichtlich, solche Verteilungen mit hinreichender Genauigkeit liefern zu können. Die von uns gelieferten Teilchendichten können nun zur Untersuchung des Einflusses von mitbewegten Elektronen, der chromatischen Abberation oder des Emittanzwachstums bei der Weiterverarbeitung des Strahls verwendet werden. So hoffen wir, dass unsere Ergebnisse zum Ziel des LIGHT-Projekts beitragen: Neuartige Laserionenbeschleuniger an konventionelle Anlagen anzukoppeln.

Contents

| | | |
|----------|---|-----------|
| 1 | Introduction | 8 |
| 1.1 | PHELIX and the LIGHT project at GSI | 10 |
| 1.1.1 | Experimental campaign worldwide | 10 |
| 1.1.2 | The LIGHT project | 11 |
| 1.1.3 | Experimental setup at PHELIX | 12 |
| 1.1.4 | Experimental results, status and goals | 13 |
| 1.1.5 | Applications and perspectives for laser-ion acceleration | 14 |
| 1.2 | Multi-scale feature of the whole physical problem | 15 |
| 1.3 | Overview of the theoretical approaches, status of the field | 16 |
| 1.4 | Thesis structure | 18 |
| 2 | Laser-plasma interaction | 20 |
| 2.1 | Motion of electrons in a laser wave | 20 |
| 2.2 | Interaction of intense laser with matter | 21 |
| 2.3 | Hot electron generation in overdense plasma | 22 |
| 2.4 | Ion acceleration mechanisms | 23 |
| 2.4.1 | Quasi-static acceleration regime of TNSA | 23 |
| 2.4.2 | Plasma expansion regime of TNSA | 27 |
| 2.4.3 | Other acceleration mechanisms | 32 |
| 3 | Particle-in-Cell code, numerical aspects | 34 |
| 3.1 | General description of a PIC code | 34 |
| 3.2 | Numerical errors, instabilities | 35 |
| 3.3 | Features of the VORPAL code | 39 |
| 3.4 | Convergence study | 40 |
| 3.5 | Optimal 2D simulation setup | 43 |
| 4 | One-dimensional, electromagnetic simulations | 45 |
| 4.1 | TNSA from a proton plasma | 45 |
| 4.2 | Comparison with theory | 46 |
| 4.2.1 | Proton distribution | 46 |
| 4.2.2 | Electron distribution and cooling | 48 |
| 4.3 | Effect of the laser pulse-shape | 50 |
| 5 | One-dimensional, electrostatic simulations | 53 |
| 5.1 | Double layer foil | 53 |
| 5.2 | Simulation setup | 54 |
| 5.3 | Thin and thick proton layers | 55 |
| 5.4 | Detachment of a thick layer | 56 |

| | | |
|----------|---|-----------|
| 5.5 | Intermediate regime | 57 |
| 5.6 | Thickness-dependent energy conversion | 59 |
| 5.7 | Relativistic momentum distribution function of electrons | 60 |
| 5.8 | Effect of the layer thickness in laser-plasma simulations | 62 |
| 5.9 | Conclusion and discussion of the 1D results | 63 |
| 6 | 2D TNSA simulations | 65 |
| 6.1 | Thickness-dependent divergence of the protons | 65 |
| 6.2 | QSA in 2D | 67 |
| 6.3 | 2D plasma expansion, envelope model | 70 |
| 6.3.1 | The Model | 71 |
| 6.3.2 | Comparison with simulations | 73 |
| 6.3.3 | Beam properties | 75 |
| 6.3.4 | Simulation with a Gaussian laser pulse | 78 |
| 6.4 | Energy conversion in 2D | 79 |
| 6.5 | 3D velocity phase space of protons | 80 |
| 6.6 | Comparison with experiments | 82 |
| 7 | Conclusions | 84 |
| | List of symbols | 87 |
| | List of figures | 90 |
| | Bibliography | 93 |
| | Acknowledgments | 99 |

1 Introduction

The laser ion acceleration in the last decade has been a very intensively studied and exciting field of research in the domain of plasma and recently accelerator physics. Due to the new laser amplification techniques the ultra-relativistic intensities ($>10^{18}$ W/cm²) became easily reachable, which revealed interesting physics in laser-plasma interaction. Such a technique is the chirped pulse amplification, which was already invented in 1960, and it was successfully improved over the decades. The technique is based on amplification of a stretched pulse, which is compressed again. The compression is done by reflecting plates with gratings, where the long-wavelength components of the pulse travel a larger distance than the short-wavelength components (negative dispersion). Thus a few hundred femtoseconds (or less) short and intense laser pulse can be produced and its energy (several tens of Joule), by interacting with material, can be partly transferred to particles (ions and electrons).

In this work we are investigating the acceleration induced by the interaction of high density targets (metal or plastic foils) with intense laser pulse focused on a small focal spot ($\approx 10\mu\text{m}$ in diameter) on the target surface. The first experimental observation and theoretical explanation was presented by Wilks [1] in 2001. The ions are not directly accelerated by the laser, but by the hot electrons, which can escape the ionized target, induce a charge separation field on the surface, which is also called Debye-sheath. This acceleration scheme is also called the Target Normal Sheath Acceleration (TNSA), because the electric field vector is always perpendicular to the surface. A brief picture of the physical process is illustrated in Fig. 1.1. The strong coupling efficiency ($\sim 50\%$) between the laser pulse and plasma was predicted earlier by simulations [2]. The energy conversion from electrons to the high energy ions is rather small, usually 20 %, which means that the overall conversion from laser energy into the ions is typically a few percent or less.

Another serious disadvantage of the TNSA is the large longitudinal energy spread of the ions. The exponential energy spectrum (with a few tens of MeV cut-off), which is always observed in experiments, is a very undesired feature, because it means that most of the energy goes to the unwanted low-energy ions. The desired energy range can be selected by a secondary device, but the higher it goes in energy the lower is the extracted beam current. The great advantage of the laser acceleration is the very small transverse emittance. The accelerated ions have almost zero transverse temperature, which makes it very unique. Although it is a very laminar beam, it has a large global divergence with a maximum half opening angle around 20 degrees. Therefore a focusing element behind the target is needed to make use of the energetic ions. Another positive property is the low operation cost and the extremely short acceleration path (few micrometers). Because of the small scale lengths it requires careful control and very precise setup.

Despite the very poor efficiency this acceleration mechanism seems to be promising key element in various fields of research and industry. One of the most demanded application is the medical treatment by ion cancer-therapy. Unfortunately the requirement in energy is too high, 200 MeV protons or carbons, which has not been reached so far. The top cut-off energy of ions in TNSA is around 60 MeV and the currently existing models do not predict higher energies with the laser parameters available at present experiments. Therefore other acceleration regimes are

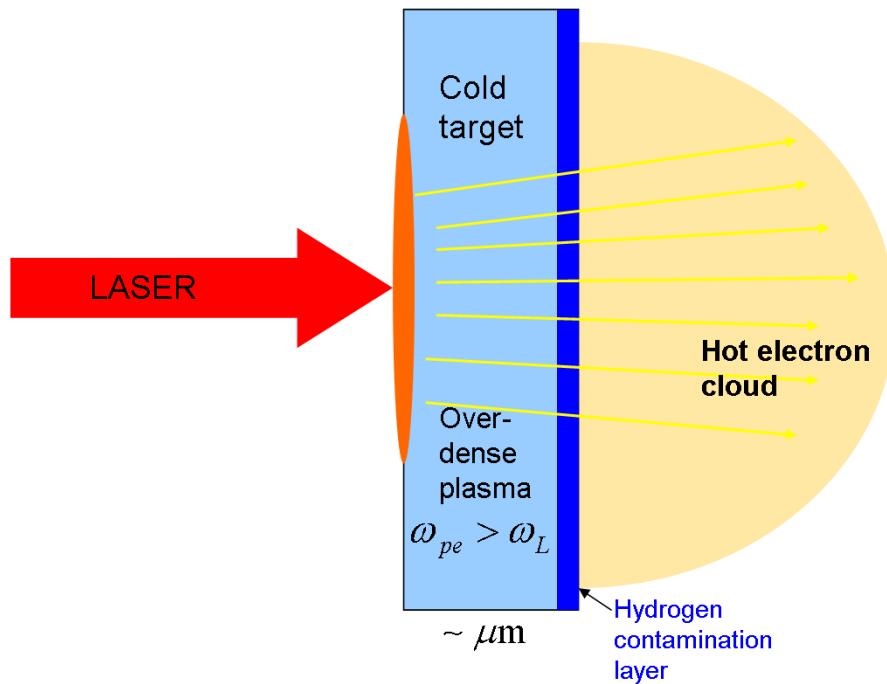


Figure 1.1: Sketch of the TNSA process.

also considered, which we discuss briefly later, but they require higher laser intensity or special target parameters and composition. Further possible applications: pre-accelerator or ion source for conventional accelerators (synchrotron), fast igniter for inertial fusion, short pulsed neutron source, etc.

Most of the applications require high repetition rate and after each shot the target has to be replaced. The latter is a mechanical problem, but the first is an issue of the laser system. Currently the record holders are the Berkeley Lab Laser Accelerator (BELLA) with 1 Hz and the DRACCO laser in Dresden with 10 Hz repetition rate. The pulse durations are limited to a few tens of fs. Several acceleration mechanisms, which theoretically provide higher ion energies and better beam qualities, require higher laser intensity, which is also difficult to produce because of nonlinear effects, causing filament propagation in the gain medium. By going higher in the intensity the laser prepulse becomes stronger. The consequence is that the target surface gets ionized and the main pulse basically interacts with an expanding plasma, which makes the physics more complicated.

Additionally to the experimental campaign there has been a large effort devoted to understand the underlying physics of the laser-plasma interaction, especially in the high intensity regime. Different scaling laws have been proposed for the hot electron temperature and for the laser energy absorption consisting of more highly nonlinear processes, which all depend on parameters like: laser intensity, incident angle, plasma density, pre-plasma scale length, etc. The next step is to describe the acceleration mechanism which can be modeled correctly only if we know the hot electron density and temperature, which are yet not exactly predictable. Therefore in many works we find theoretical models based on a two-temperature plasma expansion, where the electrons are not produced by the laser pulse, but they are assumed to have Maxwell-Boltzmann distribution with a given temperature. This is our approach as well, whereby we study the resulting charge separation on the plasma surface and the consequent ion acceleration using a Particle-In-Cell (PIC) code.

1.1 PHELIX and the LIGHT project at GSI

1.1.1 Experimental campaign worldwide

Energetic proton beams with high beam quality have been observed in many high power laser facilities worldwide. The protons can originate from the front and rear side of the target, but the number and energy of protons accelerated at the front side is smaller [3]. In designated experiments the dependence of the maximum proton energy and laser-proton energy conversion efficiency on the laser pulse duration and intensity and on the target thickness was investigated [4, 5]. One undesired effect accompanied to the CPA is the amplified spontaneous emission (ASE), which results in a pedestal pulse (prepulse) with $\approx ns$ duration. It can also influence the acceleration, because of the induced plasma expansion on the front surface, which results in a long preplasma before the main pulse reaches the target. The effect of the prepulse was also studied experimentally [6] and it was found that the shorter prepulse is more favorable, especially in the case of thin targets (1-10 μm). The reason is that, when the target is thin ($< 1\mu m$), the shock-wave induced by the prepulse (with intensity $\propto 10^{15} W/cm^2$) reaches the back surface of the target, which also expands. A theoretical work shows that a finite initial ion density gradient reduces the acceleration efficiency [7]. This effect was investigated further experimentally and the solution was found to be the enhancement of the contrast ratio (peak intensity of the main pulse over the intensity of the prepulse) of the laser [8]. For thick targets the effect of the prepulse is negligible on the rear side. The hot electrons travel through the target with a 20 degrees opening angle and spread out on the rear surface, therefore by increasing the target thickness the hot electron density reduces and the ion acceleration is weaker. Thus, we can conclude that there is an optimal target thickness for which the ion cut-off energy is maximum.

The results of the experiments were successfully interpreted using the fluid model of Mora [9] by imposing an effective acceleration time, which was defined as 1.3 times the laser pulse duration, and by calculating the hot electron density based on empirical laws [4]. However, meanwhile other analytical model has been worked out in the TNSA regime, the quasi-static acceleration, which seemed to be in better agreement with some experiments [10]. In this case the maximum energy of the protons was related to the total energy of the laser pulse [11], which was supported by experimental findings. For the estimation of hot electron temperature the scaling law introduced by Wilks [2] was widely accepted among the experimentalists. Further experiments have been carried out with the aim of clarifying the mechanism of the acceleration by changing the rear properties of the target surface (or layer) or by probing the electric field and particle densities dynamically.

By monitoring the plasma on the rear surface with transversally probing proton or laser beams the time evolution of the electric field [12] and electron density [13] and the temperature [14] could be measured. All of these results suggest that the plasma expansion model is suitable to describe underlying mechanism. The key of decreasing the longitudinal energy spread of the ion beam seemed to be hidden in the properties of the CH layer. Indeed, by changing the composition and thickness [15] or the transversal extension of the layer [16] a much better longitudinal beam quality (but lower energy) was observed in the experiments and simulations. The study of the layer properties and its effect on the acceleration is still an ongoing work in many facilities, including PHELIX (Petawatt High Energy Laser for heavy Ion eXperiments) at GSI [17].

1.1.2 The LIGHT project

In 2010 an experimental project was proposed, which makes use of protons (ions) accelerated by means of the PHELIX laser at GSI and provides transport, focusing and bunch rotation of the laser generated particle bunches by conventional ion optics and RF technology. The experiments are performed at the Z6 experimental area of GSI, which provides a suitable environment for the first systematic exploration of the interface between laser acceleration (based on TNSA) and conventional accelerator technology. In the project the capabilities of PHELIX as world-class high power (100 TW) laser with the accelerator available at GSI are combined with the target and plasma physics expertise at TU Darmstadt, the expertise in lasers of the Helmholtz Institute Jena, the high field magnet technology at the HZ (Helmholtzcenter) Dresden-Rossendorf and the accelerator expertise of the IAP Frankfurt.

This project is named as LIGHT (Laser Ion Generation, Handling and Transport) project [18] having the aim of integration the laser ion acceleration technique into the conventional accelerator environment. The goal is the collimation and transport of the TNSA-accelerated ions to the injection area of the synchrotron. It involves the understanding of the first stages of the ion acceleration and the consequent cooling of the co-moving electrons. The next stage is to explore several critical interfaces, which are the basis of any future application: de-neutralization of the neutralized particle bunch in a collimation magnetic field; collimation of a narrow energy range (10 ± 1 MeV) accompanied with a divergence angle (up to 25 degrees) from the spectrum of protons/ions by a pulsed solenoid as first collimator; transport through a drift or focusing channel; RF bunch rotation to complete the de-bunching of the originally sub-ps bunches to ns; diagnostics of the 6D phase space by means of a sub-ns streak camera and pepper-pot emittance devices.

The key element of the proton handling is a magnetic focusing device, which can be a pulsed solenoid or permanent magnetic quadrupole (PMQ). Their role is the parallelization of the divergent beam and selecting the desired energy range from the exponential energy spectrum. The magnetic field of the collimator suppresses propagation of the neutralizing electrons due to their sub-millimetre gyro-radius. This phenomenon may lead to modifications of the global production phase space distribution. First studies have been undertaken by Frank Nuernberg with the WARP-code [19]. Due to the high electron density on the solenoid axis a part of the protons are forced to bend towards this axis, thus modifying the transversal phase space of the beam. The initial beam parameters in the simulation were based on experimental measurements. With analytical curves fitted to the experiments the beam divergence and energy spectrum can be reproduced.

Due to the large energy spread, chromatic aberrations of the collimator are the most serious limitation to the realistically “usable” fraction of the full particle spectrum. These aberrations cause a degradation of the transverse emittance of the “usable” fraction of protons, and the very small production emittance becomes a relatively irrelevant quantity. The studies have been carried out using TRACE3D and the DYNAMION code, with results presented at HIAT09 [20].

Our contribution is devoted to the numerical investigation of the ion acceleration process and to provide a realistic final phase-space distribution of protons and of the co-moving electrons. The 6D beam characterization should be done at the Z6 experimental area, where using RCF stacks the transversal divergence can be measured, and with grooved targets the micro-

divergence becomes also accessible. Such measurement technique and experiments can be found in the work of Frank Nuernberg [21] and M. Schollmeier [22],[23].

1.1.3 Experimental setup at PHELIX

In the frame of the LIGHT project the new 100 TW beamline of PHELIX was build, which provides the necessary short pulse laser at the experimental area Z6 at GSI. In Fig. 1.2 we can see the sketch of the experiment, where the protons are produced. Instead of the laser produced proton beam the ion beam accelerated in the UNILAC can be also used for testing. Here we meet the full conventional accelerator infrastructure and have the perfect test bed for combining both technologies. The aim of the LIGHT project is to demonstrate injection and bunching in conventional accelerator structures of laser accelerated ions, starting with protons.

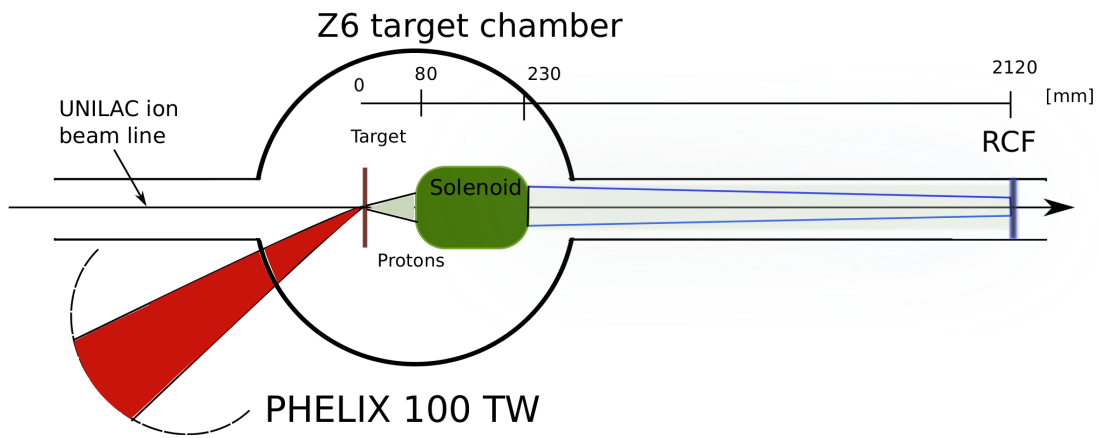


Figure 1.2: Layout of the Z6 experimental area at the GSI.

PHELIX provides for the high-power option at Z6 up to 50 J of laser energy in 500 fs on target, with maximum peak laser intensity $I_{L0} \approx 10^{20}$ W/cm². The beam enters the target chamber with a diameter of 120 mm and is focused down by a parabolic off-axis mirror to 7 μ m (FWHM) into the target chamber center. There it impacts on a thin (5-10 μ m) gold foil and a bunch of protons is accelerated via the TNSA mechanism. A few centimeters behind the target, the key element for collimation and energy selection of the proton beam is placed: a pulsed high-field solenoid, which was developed together with the necessary pulsed power supply by our collaborators at HZDR. It has an aperture of 40 mm and can reach a maximum magnetic field of 8.7 T. Due to the chromatic aberrations of this ion-optical lens, protons of different energies are focused at different distances behind the solenoid. Placing a pinhole at the right position therefore easily provides good energy selection. As proton beam diagnostic, RCF stack detectors were used at different positions: before the solenoid to detect the initial spectrum, directly behind the solenoid and at a position in the Z6 beam-line behind the target chamber. A full beam analysis is possible with these detectors via RIS (Radiochromic-film Imaging Spectroscopy) [21].

A picture of the solenoid is shown in Fig. 1.3. This solenoid was produced and tested in the high-field laboratory of the Helmholtzzentrum Dresden. Detailed CST simulation has been carried out by Peter Schmidt [24], TU Darmsadt, for mapping the magnetic field structure inside and around the solenoid and to investigate time evolution of the electric current and magnetic field. The time duration of the driving current is about 0.7 ms. Due to the strongly time dependent current and the inductance of the solenoid a phase shift can be expected between the

current and magnetic field. According to the CST simulations the time shift between peak current and peak magnetic field is about 0.04 ms, which is much longer than the proton beam (100 ps). In this scenario a very precise timing, with $\approx 10\mu\text{s}$ time resolution, is required in order to apply the maximum magnetic field on the short proton bunch.

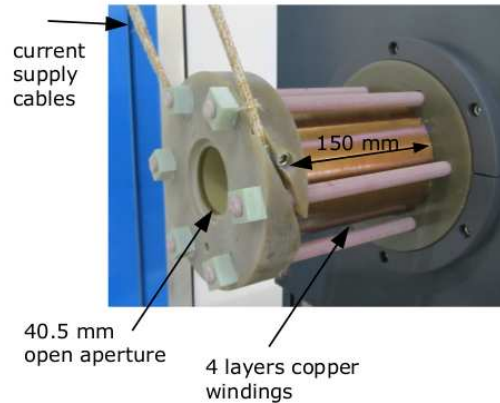


Figure 1.3: A picture of the solenoid used in the experiment. Courtesy of Simon Busold.

The Target Laboratory at the University of Darmstadt has previously provided various types of 3D target geometries for fundamental research experiments with laser and particle beams at high energy densities. As for experiments which investigate the feasibility of focussing the beam with a specially shaped target, several different designs and manufacture targets have been proposed such as hemispherical targets made from gold with different wall thicknesses, plane targets with a cone to promote focusing or a spherical target for ion acceleration combined with an adjacent cone. The experiments and simulations with these concave target structures have been performed by Oliver Deppert [25, 26] from TU Darmstadt.

The measurement of beam characteristics is done by RCF (radiochromic film) stacks which is a very useful and common technique. These dosimetry films measure the radiation dose provided by the protons (high stopping power). After interaction with ionizing radiation the film changes its color from nearly transparent to blue with a spatial resolution more than 10^4 dots per inch. After the proton beam goes through the stack of RCF's with a graphical deconvolution technique [21] the energy spectrum and transversal size of the beam can be reconstructed

For the longitudinal focusing of the proton bunch an RF buncher cavity has been proposed which is available at the GSI.

1.1.4 Experimental results, status and goals

In Fig. 1.4 we can see the typical proton energy spectrum and energy resolved envelope opening angle of the proton beam measured at the PHELIX facility. This laser is capable of delivering 120 J energy in a 500 fs long pulse with the maximum intensity 10^{20} W/cm² at a wavelength of 1 μm . The maximum energy reachable is about 40 MeV and the opening half angle of the transversally cold beam can be up to 30 degrees.

The results of the PHELIX experiments have shown a successful capturing and focusing of the accelerated protons using a pulsed solenoid [27]. The applied magnetic field strengths were 7.2 T and 8.5 T, which was able to focus 3.7-6.7 MeV protons. For the 8.5 T magnetic field protons

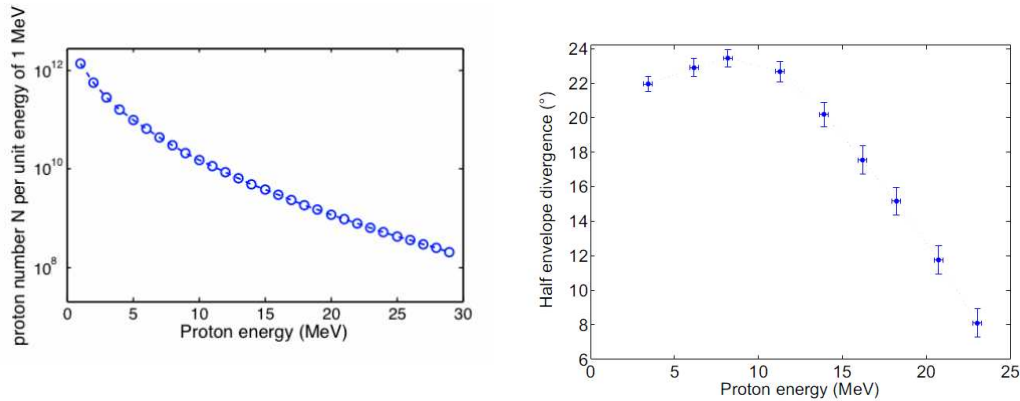


Figure 1.4: Measured energy spectrum of protons (left) and the energy-dependent half opening angle of the proton beam (right). Courtesy of Frank Nürnberg.

were collimated around 13.4 MeV energy, being in good agreement with simulations, which show about 20 % transport efficiency.

For the proton focusing two magnetic devices can be used in the framework of the LIGHT project at GSI. The resulting beam profiles, measured in the 2012 experiments, show a non-uniform transversal density distribution, which was explained by the imperfections in the magnetic field lines of the solenoid. Accurate simulations with realistic 6D initial beam distribution is required to support this finding.

The second device is a permanent magnetic quadrupole with 85 T/m field gradient and 80 mm in length. The resulting beam profile at a given distance behind the quadrupole seemed to be more uniform. The chromatic aberration was clearly visible from the different beam size for different energies. With the parameters of this experiment the best focus was obtained for 5 MeV protons.

The interesting experimental results of the last 2 years show a promising progress in the LIGHT project. Together with the target and laser beam shaping it might be possible to generate a few tens of MeV divergence-less proton beams. The proton acceleration via TNSA could be an excellent ion source and pre-accelerator for many conventional accelerators, replacing the expensive and large linear accelerators.

1.1.5 Applications and perspectives for laser-ion acceleration

Because of the challenging beam characteristics (like the ultra-low emittance [28]), discussions have been started about possible applications in: energy research (Fast Ignitor in the inertial fusion energy context), injection of high peak power ion beams for basic research facilities, medical treatment (proton and carbon therapy, transmutation of short lived radioisotopes for positron emission tomography (PET) in hospitals), the modification of material parameters (starting from applications in materials science up to warm dense matter research and laboratory astrophysics) and short pulsed neutron sources [29]. To prosper in these exciting applications, the fusion of laser-ion-acceleration and conventional ion accelerator technology is of main importance. The establishment of this connection is the main goal of the LIGHT project.

Laser driven ion acceleration, has been frequently discussed to be used in particle therapy because its compactness compared to conventional acceleration. The medical quality requirements

are very strict and will prevent a medical use of laser ion acceleration in the near future. However, the extreme short pulse lengths of a few picoseconds of the particle beams can be used to study the kinetics of the cellular response to exposure of ionizing radiation in a time scale that was not accessible up to now. Such biological test-experiments have been done in 2011 using the PHELIX laser beam [30].

The energy loss of heavy ions in plasma is one of the fields of research in the plasma physics group at GSI [31]. To probe more homogeneous, slower expanding and denser plasmas an indirect heating scheme has been developed, where the plasma is heated by soft x-ray radiation. In this scheme the x-ray radiation is generated by a laser driven hohlraum. This hohlraum radiation is used to heat a secondary hohlraum, containing a carbon foil. The carbon foil is then heated to plasma temperature and can be investigated by ions.

As we will see in chapter 6 the reason of the divergence is the non-uniform hot electron density in the Debye-sheath. Recently became possible to create laser pulses with annular intensity distribution, which makes possible the generation of a uniform hot electron density in a spot comparable with the diameter of the annular laser beam. Simulations show that with this technique a laminar proton beam can be accelerated without transversal divergence. The experiments unfortunately does not show yet any improvement, mainly because of the imperfections of this novel laser pulse shape. Developments in this directions show a promising option instead of using magnetic focusing elements.

Recently an other acceleration mechanism has been proposed in the framework of the LIGHT project. The Break-out afterburner (BOA) does not require extremely high laser intensities, which are still not available, but it predicts higher energy conversion efficiency from the laser pulse to the protons and better beam properties. This mechanism will be described in more details in section 2.4.

1.2 Multi-scale feature of the whole physical problem

The simulation works included in the LIGHT project can be divided in different stages. In order to reach the control and understand the journey of the proton beam through the different devices and acceleration phases a chain of simulation has to be performed by passing the data or analytical expressions from one to the other. The schematic view of the problem is presented in Fig. 1.5, where also the required resolution of the simulations are also indicated. The connection between the stages has to be perfect, which makes the problem challenging.

The most critical and less understood stage is the laser-plasma interaction, where the hot electrons are generated. The consequent proton acceleration has to be covered in the same simulation. Because of the small cold electron Debye-length, these simulations require extremely high resolution in space and time. The acceleration process and the resulting proton beam properties depend on various parameters: laser pulse shape, pulse duration, target thickness, preplasma scale length and, as we point out in this work, thickness of the contamination layer.

In the next stage, practically after the end of the laser pulse, the acceleration is weak and the electrons cool down adiabatically. Finally a neutral proton bunch is produced with frozen velocity phase-space, drifting and expanding in the vacuum until it meets the magnetic field of the focusing components. At this stage the beam density is so low that a much coarser grid resolution is sufficient in the simulations and an electrostatic field solver might be enough to simulate the particle motion. However, due to the small gyro-radius, the electron current can be strong if the beam was not de-neutralized before.

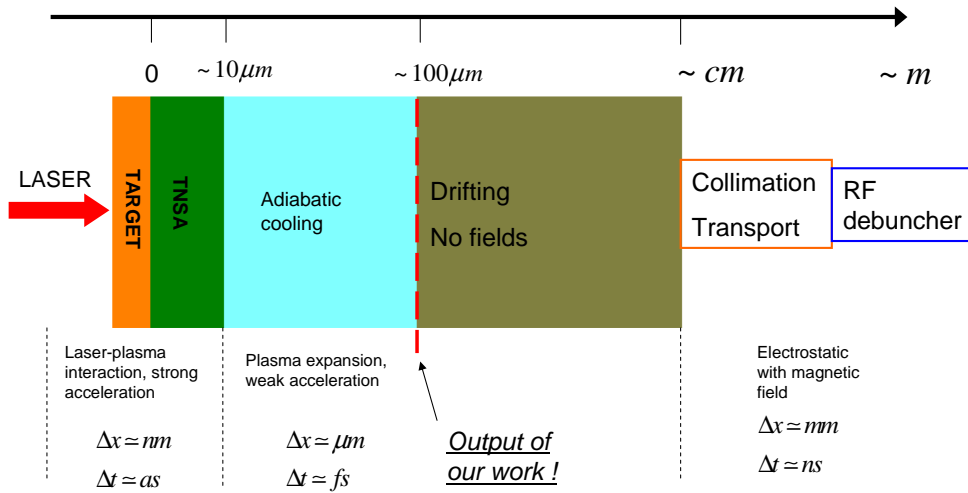


Figure 1.5: Diagram of the different stages of the LIGHT project.

1.3 Overview of the theoretical approaches, status of the field

In the TNSA many different ion species are accelerated, which originate from the hydrogen-rich contamination layer at the target surface. The common aim of most of the works is to predict or explain the maximum proton energy [10]. The protons are the lightest ions, therefore they are accelerated first, and their number in the contamination layer is usually dominant. Thus it is justified to study the behavior of a purely proton plasma filled with high temperature electrons. The physical phenomenon is called plasma expansion which can be analytically studied with the assumption of constant temperature in time, therefore the model is called isothermal plasma expansion.

The first analytical work was presented by J. E. Crow et al. [32] already in 1975. The model was improved and validated by a Lagrangian code in the work of P. Mora in 2003 [9], when the high energy protons were already observed in experiment using high intensity laser. The isothermal model predicted a proton energy spectrum similar to the one measured in experiments and by fitting the analytical expression to the measured data, the hot electron temperature could be estimated if the acceleration time was known. The weakness of the model is that the temperature is kept constant, while in the reality the hot electrons cool down during the acceleration. Therefore an effective acceleration time (t_{acc}^{exp}) had to be introduced, which defines the duration of the isothermal phase of the acceleration (when everything fits with the model) and what happens after is called adiabatic phase (when the acceleration is not so strong and the maximum proton velocity converges to a finite value). If the t_{acc}^{exp} is assumed to be equal to 1.3 times the laser pulse duration, then Mora's model is quite usable. Several other models have been proposed to describe in one set of equations the plasma expansion including the changing temperature [33, 34] and [35] which is the extension of [9], but no fully analytical model could be obtained. The most detailed numerical model [36, 37] includes electron kinetic effects, reveals very accurately the time evolution of the hot electron energy distribution and shows perfect agreement with PIC simulations.

In order to describe the realistic situation we have to include, as a first step, the cold electrons as well in the plasma, because not all of the target electrons are heated up by the laser. Thus we have to deal with a two-temperature plasma, which is even more complicated and the analytical treatment becomes almost impossible. However, our simulations show that there is no big difference between the one- and two-temperature plasma expansion, the proton velocity phase-space and density is always defined by the hot electron parameters. The effect of the cold electrons is restricted to the plasma surface, where a singularity occurs in the potential-profile for high temperature ratios [38]: $T_h/T_c \gg 10$, where the c and h subscripts correspond to cold and hot respectively. It is also called rarefaction shock which leads to a modified density and energy distribution of ions in the low energy range. The properties of the two-temperature plasma expansion have been studied in great details [39, 40, 41] and we studied as well, up to some extents, with the means of a PIC plasma simulation code, which we present later.

In [39, 42, 43] the authors, using a Vlasov code, show that if we include also heavier ions in the plasma, mixed uniformly with the protons, in the proton energy spectrum a significantly high and narrow peak appears, which is a very interesting and important feature. If the protons around this peak could be selected, a mono-energetic beam with high current could be produced. Unfortunately there are two conditions: constant electron temperature and the heavy ion density must be higher than the proton density. We believe that the target in the reality has a layered structure (which was also considered in [42, 43]), the heavy ions of the metal are separated from the hydrogen-dominated contamination layer. Recent works in this direction have been done by Albright [44] and Brantov [45] where a semi-analytical model describes the modification of the potential profile due to the accelerated proton layer and the energy distribution is evaluated numerically. The assumptions taken and the regimes covered in these works we discuss later together with our results including the charge separation effects.

Another acceleration mechanism, which has not been mentioned so far, is the quasi-static acceleration (QSA) [46, 11, 47]. In this model the layer is assumed to be very thin, such that the number of protons is much smaller the number of hot electrons in the Debye-sheath. In this case the protons are accelerated as test particles in the almost unaffected electron cloud, that is why it is called quasi-static acceleration. This model predicts much smaller energy spread, but also lower maximum energy. If we solve the Poisson equation for electrons with Boltzmann distribution, then we get an infinitely long logarithmic potential profile [48] outside of the plasma, which leads to infinitely high proton energies. This is not what we expect, therefore the end of the electron cloud has been defined based on energy conservation [47, 11, 49]. The minimum potential (maximum kinetic energy of protons) is defined by the maximum electron energy in the plasma. In the model of Schreiber [50] the derivation is done in cylindrical geometry and the maximum ion energy is related directly to the laser pulse parameters.

As we can see many ideas and theories have shown up in the last decade and these are only one-dimensional aspects. In higher dimensions almost exclusively simulation tools has to be used to model and understand the ion acceleration induced by laser pulse. Most powerful and compact tool, but time consuming at the same time, is the PIC plasma simulation code, which usually requires high computational power. In the literature we can find 2D PIC simulation studies [51, 52, 53], which report some scaling laws on the maximum proton energy depending on the laser and target parameters (laser intensity, pulse duration, target thickness, etc.). In all cases a proton plasma is considered, because for this ion the acceleration time scale is the shortest (highest plasma frequency), thus the number of time steps in the simulations is rather small. The most recent simulation work deals with the optimization of laser and target parameter

in order to maximize the proton energy and beam current considering CH (carbon-hydrogen) target [54].

The important conclusion of the TNSA simulations is that two different regimes could be identified. The first is the gradient-dominated (quasi-neutral) regime, where the density scale length ($L_n = -n(dn/dx)^{-1}$) of the expanding plasma is larger than the hot electron Debye length. It is the case for thin targets, where the hot electron density, due to the recirculation [55], is high and the Debye-length ($\lambda_D = (\epsilon_0 T_h / (q_e^2 n_{h0}))^{1/2}$, where n_{h0} is the hot electron density) is small. In the case of thick targets the laser pulse intensity (hot electron temperature) must be not too high in this regime. The electric field scales as $E = T_h / (q_e L_n)$, like in the isothermal plasma expansion. The second regime is called Debye-length-dominated (non-neutral) regime, because the L_n is very small, therefore it happens for short laser pulses and thick targets, when the plasma does not have time to expand and the hot electron density is small (λ_D is large). In this case the electric field is proportional to the square root of the hot electron pressure, $\propto \sqrt{n_h T_h}$, therefore the maximum ion energy scales differently with the pulse and target parameters, as it was also observed in experiments [53].

1.4 Thesis structure

The theoretical introduction of the laser-plasma interaction is presented in chapter 2, where we describe what is the ponderomotive force (section 2.1), what overdense plasma means (section 2.2) and the main mechanism of the electron heating (section 2.3). The ion acceleration mechanisms induced by the laser pulse are discussed in section 2.4.

Because it is a more numerical than analytical work, we introduce the PIC simulation concepts in chapter 3, where we present the code in general (section 3.1) and discuss its weakness (section 3.2). Our simulation tool is the VORPAL [56] plasma simulation code, which has some useful features implemented and it is capable of performing fast and reliable simulations. Its performance and stability is discussed in sections 3.4 and 3.5.

In the following three chapters we present our 1D and 2D simulation results. In chapter 4 simulation of the high intensity laser pulse interacting with a proton plasma is discussed and compared to the predictions of the isothermal plasma expansion model (section 4.2). We investigate in great details the proton velocity phase-space and the electron cooling during and after acceleration. The difficulties of analyzing the simulation data and comparing it to the idealized analytical model is discussed in section 4.3. A useful alternative to study TNSA is the plasma expansion simulation, where we do not use the laser pulse to generate the hot electrons, but load them into the simulation box according to a well-known density distribution with a fixed initial temperature. This trick simplifies the problem, excludes the stochastic non-equilibrium behavior of the laser-produced hot electrons and gives the same physics what we see by using the laser pulse. This kind of simulations are presented and analyzed in chapter 5, where we describe the double layer structure of the plasma (section 5.1). The consequences of changing the proton layer thickness are investigated in the following sections, where we point out that the plasma expansion and QSA are only two extreme cases of the TNSA (section 5.3). Finally we propose a simple analytical expression for the energy conversion from hot electrons to protons in section 5.6 and check its applicability in TNSA using laser pulse in section 5.8.

In chapter 6 basically we do in 2D the same study as we did in 1D, but in less details. In 2D we have to use a laser pulse in order to maintain the constant source of hot electrons, which quickly spread out in the transverse dimension. We focus on the divergence of the accelerated

beam and discuss its dependence on the layer thickness in section 6.1. We pick the two extreme cases, which are in 1D well-understood, and give analytical expressions of the energy dependent divergence in the thick layer regime in sections 6.2. In section 6.4 we present the reduced energy conversion, which would be even smaller in 3D. Using our 2D model it is possible to build an analytical description of the 3D proton velocity phase-space and density distribution, which is presented in section 6.5. Finally the model is applied to real experimental data showing a good agreement with the observed divergence of the protons. The conclusions and remarks are summarized in chapter 7.

2 Laser-plasma interaction

In this chapter we briefly discuss the main effects which occur in the relativistic laser-plasma interaction. The main source is the book of P. Gibbon [57], which gives a very good introduction into the short pulse laser interaction with matter. Further theoretical description of the physics can be found in the book of P. Mulser [58], which covers more quantum-mechanical and relativistic effects. We consider only the overdense plasma case and concentrate mainly on the electron heating via different mechanisms. The laser pulse is always linearly polarized, also in our simulations, and the incidence angle is 90 degrees.

2.1 Motion of electrons in a laser wave

First let us define the parameter which tells us how relativistic is a laser pulse. When we consider a single electron, moving freely in the fields of the laser pulse, there are two forces acting on it: a transversal force in the direction of the electric field, $F_e = q_e E_L \sin(\omega_L t)$, therefore the electron will acquire a velocity $v_\perp = -q_e E_L / (m_e \omega_L) \cos(\omega_L t)$, where E_L is the electric field amplitude, ω_L is the laser frequency, m_e is the electron mass and q_e is the elementary charge. In the longitudinal direction due to the magnetic field the electron experiences the force: $F_m = q_e v_\perp B_L \sin(\omega_L t)$, where B_L is the magnetic field component. The laser pulse is called relativistic when the longitudinal force exceeds the transversal one, therefore a normalized parameter can be introduced:

$$a_L = \frac{F_m}{F_e} = \frac{q_e E_L}{m_e c \omega_L}, \quad (2.1)$$

where we used the relation $B_L = E_L/c$, c is the speed of light. This quantity is also called the normalized electric field amplitude and it is equal to the relativistic gamma factor of the transversal motion. The laser intensity is given by $I_{L0} = \epsilon_0 c E_L^2 / 2$, therefore a_L can be expressed in terms of laser intensity:

$$a_L^2 = \frac{I_L [W/cm^2] \lambda_L^2 [\mu m^2]}{1.37 \cdot 10^{18}} \quad (2.2)$$

Let us take a closer look at the Lorentz force acting longitudinally on the electrons. For constant field amplitudes the time average of this force is zero. If the laser pulse amplitude is not uniform, but has, for instance, a Gaussian envelope shape, then the magnetic field can be expressed according to the Maxwell-Faraday law:

$$B_L = \frac{1}{\omega_L} \frac{dE_L}{dx} \cos(\omega_L t) \quad (2.3)$$

Now if we calculate again the Lorentz force pointing in the longitudinal direction, we obtain :

$$F_m = -\frac{q_e^2}{4m_e\omega_L^2} \frac{dE_L^2}{dx} (1 + \cos(2\omega_L t)) \quad (2.4)$$

Two important things can be observed in this expression. First we see that the force is proportional to the energy gradient in the pulse (square of the electric field). Secondly, this force has an oscillating component which has a frequency twice the laser frequency. It means that twice per every cycle electrons are accelerated at the plasma surface, where the laser gets reflected. This heating mechanism we discuss later in more details. The time-independent part of the force is also called ponderomotive pressure, which is the highest pressure ever produced in laboratory.

2.2 Interaction of intense laser with matter

When a laser pulse reaches a plasma it can penetrate and propagate through the plasma, if the density is low. In this regime with relativistic and short laser pulse the so-called wake-field acceleration can be induced, which is a different type of laser acceleration, where the accelerated particles are electrons. If the plasma is dense such that the electron plasma frequency (ω_{pe}) is higher than the laser frequency, then the electromagnetic wave can not penetrate the plasma and a part of it gets reflected, another part is absorbed and some part can tunnel further into the plasma in the form of higher harmonics. The condition of reflection can be easily obtained by analyzing the dispersion relation of the relativistic light wave:

$$\omega_L^2 = k_L^2 c^2 + \omega_{pe}^2, \quad (2.5)$$

where $\omega_{pe} = (n_e q_e^2 / (m_e \bar{\gamma} \epsilon_0))^{1/2}$ and $\bar{\gamma} = \sqrt{1 + a_L^2/2}$ is the cycle average gamma factor, which is an important quantity in the hot electron temperature scaling. In this equation it is clear that for $\omega_{pe} > \omega_L$ the wave number becomes imaginary, which is unphysical. Now we can write the expression for the critical density which is the border between the overdense and underdense plasmas:

$$n_{cr} = \frac{\epsilon_0 m_e \bar{\gamma} \omega_L^2}{q_e^2}. \quad (2.6)$$

Usually in a TNSA experiment both regimes are present, because of the long preplasma on the target front surface. The laser pulse propagates in the exponential density profile of the expanded plasma until it reaches the point where the electron density is equal to n_{cr} . The target can become transparent for the laser, if its intensity is high enough. The reason is that in Eq. (2.6) if the gamma factor is large and most of the electrons are already heated (long pulse is required), then the critical density can be higher than the density of the target, thus allowing the laser pulse to go through. The laser wavelength is always more or less the same, $\lambda_L \approx 0.8 \mu\text{m}$.

2.3 Hot electron generation in overdense plasma

Although we mentioned that the only considered case in our simulations is the perpendicular incidence, but for completeness we describe some mechanisms which depend on the incidence angle. In a simple picture the collisionless laser energy absorption can have four different scenarios as it is described in the book of Gibbon [57]. There is a fifth case which is the most relevant for the perpendicular incidence and high intensities, which is the $\mathbf{j} \times \mathbf{B}$ heating.

The first mechanism is the resonance absorption, which was already theoretically described in the 60's. In this case the plasma scale length (L_n) is much longer than the laser wavelength. The p-polarized light (the electric field component, the incident and reflected wave vectors are in the same plane) propagates until the critical surface ($n_e = n_{cr}$) where it drives up a plasma wave, which grows over a few periods, then gets dumped due to wave breaking. Here the electrons gain energy from the electric field not from the ponderomotive force. Another mechanism is the vacuum heating (Brunel mechanism) [59, 60], which happens for steep density profiles. In this case the electrons are dragged out from the plasma by the electric field and half of a period later they are accelerated back into the plasma, where the laser field can penetrate only to the skin depth $l_s \approx c/\omega_p$, where $\omega_p = (n_e q_e^2/m_e \epsilon_0)^{1/2}$ is the electron plasma frequency, therefore the laser field can not act on the electron any more. The optimum angle of this absorption predicted by Brunel was around 73 degrees, when all of the laser energy is absorbed. However, the simulations have shown lower efficiency, because the effect of the magnetic fields were not included in the model.

The other two mechanisms are closely related to the vacuum heating, both manifest themselves in a tiny layer near the plasma surface. When the mean thermal excursion length of the electrons is larger than the skin layer ($v_{te}/\omega_L \gg l_s$) we talk about anomalous skin effect. In this case the electron temperature is so high that the electric field can not pull it out from the plasma, but it will act on an enlarged skin depth, thus the absorption is increased. The opposite limit of this mechanism ($v_{te}/\omega_L \ll l_s$) is called sheath inverse-bremsstrahlung (SIB). The electrons receive several kicks from the laser field as they are passing the skin layer.

In experiments, due to the prepulse, the latter two mechanisms are irrelevant. For the heating the ponderomotive force is responsible, when the laser is ultra-relativistic and is shot perpendicular to the plasma. With different angle of incidence the resonance absorption can increase the electron heating efficiency, but the significant part is pushed by the ponderomotive force. In this regime the electron heating is a stochastic process [61], it is the result of the interplay between the oscillating ponderomotive pressure and the induced charge-separation field around the critical surface. The highly non-linear physics of the interaction can be studied in great details by using a PIC simulation code. Wilks used ZOHAR [2] in order to support his theoretical scaling law of the hot electron temperature and to reveal 2D effects, like bubble formation (in the presence of under-dense preplasma) and hole boring, which can be the reason, together with the induced magnetic fields, of the divergent hot electron current through the target. In his simple model the electrons gain energy from the ponderomotive potential and the temperature scales as:

$$T_h = m_e c^2 (\sqrt{1 + a_L^2} - 1) \quad (2.7)$$

This scaling found to be not accurate for higher intensities ($a_L > 10$), it overestimated the temperature. Later Beg [62] proposed a different scaling law based on experimental measure-

ments. This empirical law was confirmed by a relativistic theoretical model [63], which gave very similar results with only 10 % discrepancy. The original Beg's scaling reads: $T_h(\text{keV}) = 215(I_{18}\lambda_{\mu\text{m}}^2)^{1/3}$, while the theory predicted $T_h = [(1 + \sqrt{2}a_L)^{1/2} - 1]m_e c^2$. The much lower electron energies than the ponderomotive scaling was also observed in simulations [64]. The newest theoretical model, based on a kinetic approach, shows very good agreement with simulations and experiments over the whole intensity range [65]. However more simulations and experiments are needed to check its reliability and dependence on the incident angle.

The hot electron temperature is often defined as the average energy of the electrons with the energy higher than a certain threshold, which divides the electrons in hot and cold populations, or it is obtained by fitting the energy spectrum with an exponential function. Unfortunately this single number does not tell us anything about the energy and density distribution of the hot electrons, which are important if we want to know the energy flux or energy and angular spread. A detailed simulation work has been done by Sherlock [66], who found the hot electron energy distribution function by fitting to the simulation results:

$$f(W, \theta) = C \exp \left[- \left(\frac{W - W_{av}}{\Delta W} \right)^2 \right] \exp \left[- \left(\frac{\theta}{\theta_{1/2}} \right)^4 \right] \quad (2.8)$$

where C is a normalization coefficient, W_{av} is the average energy, $\Delta W \approx 0.57W_{av}$ is the energy spread and $\theta_{1/2} \approx 25^\circ$ is the half opening angle. The given function fits very well to the simulation results in the intensity range 10^{19} - $2 \cdot 10^{20}$ W cm⁻².

2.4 Ion acceleration mechanisms

In this section we present the main acceleration regimes of the TNSA mechanism. As we discussed earlier the acceleration is triggered by charge separation fields induced by the laser-produced hot electrons at the target rear surface, where they can escape from the neutral ionized solid target, which is considered as a thermal plasma. The analytical derivations can be found in the corresponding articles, here only the main steps and results are presented. The figures present results from 1D electrostatic PIC simulations. In these simulations only a thermal plasma is used, without heating it with a laser pulse. We are interested in the charge separation effects around the plasma surface and in the consequent ion acceleration in the electric field of the hot electron-sheath.

2.4.1 Quasi-static acceleration regime of TNSA

In the first approximation we can consider the ions to be immobile. Thus we can obtain the equilibrium density distribution of electrons by solving the Poisson equation inside and outside of the plasma. Assuming thermal equilibrium everywhere the Poisson equation in 1D geometry can be written in the following form:

$$\frac{\partial^2 \Phi}{\partial x^2} = \frac{q_e}{\epsilon_0} (n_{h0} \exp(q_e \Phi / T_h) + n_{c0} \exp(q_e \Phi / T_c) - n_0) \quad (2.9)$$

where n_{c0} , T_c are the cold electron density and temperature. Here we do not consider the proton layer yet, the neutralizing background is made of immobile singly ionized ions.

The detailed derivation of the solution can be found in [48], here we highlight the results important for us. These are the potential profiles inside ($x < 0$) and outside ($x \geq 0$) of the plasma:

$$\varphi_{out}(x) = \varphi_0 - 2 \ln\left(1 + \frac{x}{\lambda_D \sqrt{2 \exp(-\varphi_0)}}\right) \quad (2.10)$$

$$\varphi_{in}(x) \approx \varphi_0 \exp(rx/\lambda_D) \quad (2.11)$$

where $r = \sqrt{1 + (n_{c0}/n_{h0})(T_h/T_c)}$, the potential is normalized to T_h/q_e and at the plasma surface ($\varphi_0 = \varphi(x=0)$) it has the following value [48]:

$$\varphi_0 = -\frac{1 + (n_{c0}/n_{h0})(T_c/T_h)}{1 + n_{c0}/n_{h0}} \quad (2.12)$$

The corresponding electric field, which is equal to the starting peak electric field in the plasma expansion for $t = 0$, is the derivative of the potentials with negative sign:

$$E_{out}(x) = 2E_0 / \left(\sqrt{2 \exp(-\varphi_0)} + \frac{x}{\lambda_D}\right) \quad (2.13)$$

where $E_0 = \sqrt{n_{h0}T_h/\epsilon_0}$ and

$$E_{in}(x) = \sqrt{2 \exp(\varphi_0)} E_0 \exp(\alpha rx/\lambda_D) \quad (2.14)$$

where α must be calculated numerically from the neutrality condition (the total charge is zero in the system) using the density profiles. The protons placed in a layer thinner than the skin depth (penetration depth) of the electric field will be accelerated as test particles. Their charge is so small that they do not modify significantly the electron cloud, therefore this acceleration is called quasi-static acceleration. The scale length of the penetration of the electric field into the plasma is $\approx rx/\lambda_D$, which is equal to the cold electron Debye-length $\lambda_{Dc} = (\epsilon_0 T_c / (q_e^2 n_0))^{1/2}$, for $r \gg 1$.

Assuming the Boltzmann distribution for the electrons we can calculate their density profiles. These expressions will be used as initial density distributions in the plasma expansion simulations. The Eq. (2.11) is not an exact solution, therefore we have to use the α correction factor in our simulations. The value of the potential at the plasma surface depends on the hot and cold electron parameters, it is $\varphi_0 = -1$ when the cold electron density is zero (one-temperature plasma) and $\varphi_0 \approx 0$ when the cold electron population is dominant. Usually the latter is the case in the interaction of laser with overdense plasma.

It is necessary to obtain an initial thermal equilibrium for the electrons, which would be achieved only after many plasma oscillations, if we used a step-like density profile. Outside of the plasma, $x > 0$, only hot electrons are present, therefore, using the relation $n_h(x) = n_{h0} \exp(\varphi(x))$, their density profile is:

$$n_h(x) = n_{h0} \frac{2}{(\sqrt{2 \exp(-\varphi_0)} + x/\lambda_D)^2} \quad (2.15)$$

The extension of the Debye-sheath depends on the maximum electron energy (ϵ_{max}). The correct shape of the potential far from the target can not be calculated analytically [46]. In our simulations we take Eq. (2.15), which holds close to the surface, and we define the end of the electron cloud as the point where the potential is equal to ϵ_{max} :

$$L_e = \lambda_D \sqrt{2 \exp(-\varphi_0)} \left(\exp\left(\frac{\varphi_0 + \epsilon_{max}}{2}\right) - 1 \right) \quad (2.16)$$

For ϵ_{max} we choose $7.5T_h$, which is close to the prediction of scaling laws used in Ref. [11] if we use the laser parameters of PHELIX at GSI: ≈ 500 fs laser pulse duration and 10^{19} - 10^{20} W/cm² peak intensity. For this value of ϵ_{max} the hot electron energy spectrum can be resolved with the number of macroparticles used in our simulations.

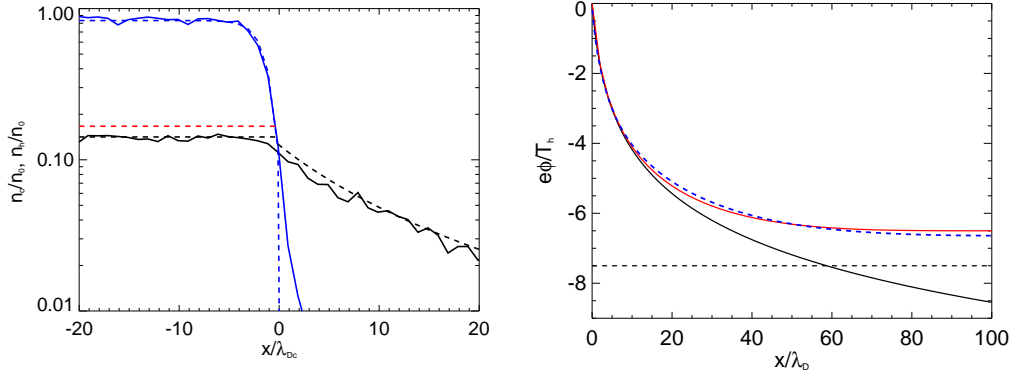


Figure 2.1: Left: The electron density profiles around the plasma surface at $\omega_{peh}t=143$. The point $x = 0$ corresponds to the initial plasma surface. The full lines show the density of hot (black) and cold (blue) electrons from simulation, while the dashed blue line represents Eq. (2.18) and the dashed black line is Eqs. (2.15, 2.19). The dashed red line indicates the initial hot electron density, n_{h0} . The initial electron parameters: $n_{c0}/n_{h0} = 5$, $T_c/T_h = 0.05$. Right: The potential from simulation (blue dashed line) compared with Eq. (2.10) (black) and with the numerical solution of Eq. (4) from [46] (red). The horizontal dashed line represents the value of ϵ_{max} .

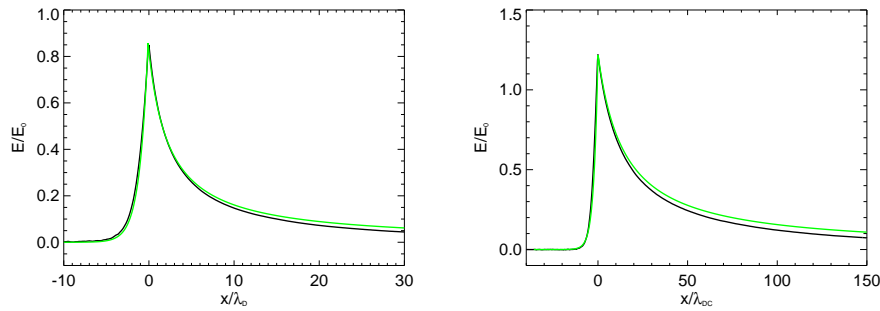


Figure 2.2: Charge separation field at the plasma surface in 1T (left) and 2T plasma (right) with $n_c/n_h=3$ and $T_c/T_h=0.05$. The black lines are simulation results and the green represent the analytical formulas.

Inside of the plasma, $x < 0$, in the one-temperature (1T) case the hot electron density is described using Eq. (2.11) with $\varphi_0 = -1$ and $r = 1$:

$$n_{h1T}(x) = n_{h0} \exp(-\exp(\alpha x/\lambda_D)) \quad (2.17)$$

In the two-temperature (2T) plasma the cold electrons dominate inside of the plasma, therefore for their density we use again Eq. (2.11), but they are also in equilibrium with the potential $n_c(x) = n_{c0} \exp(\varphi(x)T_h/T_c)$, which gives:

$$n_c(x) = n_{c0} \exp(\varphi_0 \frac{T_h}{T_c} \exp(\alpha r x/\lambda_D)) \quad (2.18)$$

In the 1T plasma $\alpha = 0.95$, but in the 2T plasma this correction factor depends on the electron pressure ratio and in our simulations it varies between 0.7-0.9. The hot electrons are in pressure-equilibrium with the cold electrons, therefore for their density distribution we use a similar exponential function, obeying the correct boundary condition at $x=0$ for the electric field:

$$n_{h2T}(x) = n_{h0} \exp(\frac{\varphi_0}{r} \exp(\frac{r}{\varphi_0} \sqrt{2 \exp(\varphi_0)x/\lambda_D})) \quad (2.19)$$

In order to confirm the validity of these expressions we performed an electrostatic simulation with 2T plasma starting with step-like density profiles. The resulting hot and cold electron density after thermalization is shown in Fig. 2.1, left plot, and compared with the analytical expressions with $\alpha = 0.86$. The time is normalized to $\omega_{peh} = (n_{h0}q_e^2/m_e\epsilon_0)^{1/2}$. A small discrepancy appears in the cold electron density close to the surface due to the strong plasma oscillations. During the relaxation the cold electrons get heated and can escape from the plasma. Another small effect is that inside of the plasma the hot electron density will be lower than its initial value, because a part of them escapes from the plasma, while the cold electrons are slightly compressed. This effect is very small for $L_p \gg \lambda_D$, therefore we neglect it in the analytical description. For large r (small φ_0) values instead of Eq. (2.19) we can simply take a constant value, n_{h0} . In Fig. 2.1, right plot, the potential profile is shown outside of the target and compared to the numerical solution of Eq. (4) from [46]. As we can see the electron cloud does not fit with Eq. (2.10) far from the target, but it is very close to the numerical result.

In this way we can simulate a correct charge separation at a plasma surface including one- or two-temperature electrons, which are in thermal equilibrium. The resulting electric field from the simulation, where the electron density distribution is initialized with the analytical expressions, is shown in Fig. 2.2 and compared to the analytical predictions.

The analytical expression for the potential outside the plasma (Eq. 2.10) for $x \rightarrow \infty$ does not converge to a finite value, but it increases logarithmically. This is of course unrealistic, because the protons do not gain infinite kinetic energy during the acceleration. The Poisson equation has to be modified such that it includes only the hot electrons with negative total energy, which means that the electrons with kinetic energy larger than the local potential leave the plasma and only the trapped electrons contribute to the electric potential. With this correction the Poisson equation for $x > 0$ has the form [46]:

$$\frac{\partial^2 \Phi}{\partial x^2} = \frac{q_e}{\epsilon_0} n_{h0} \exp(q_e \Phi/T_h) \text{Erf}(\sqrt{q_e \Phi/T_h}) \quad (2.20)$$

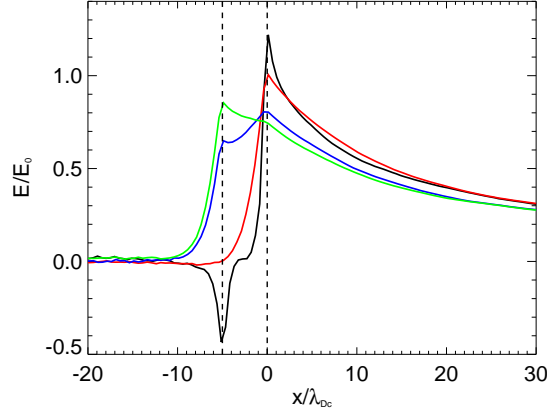


Figure 2.3: Charge separation fields at the plasma surface for : $n_p = 5n_0$ (black), $n_p = n_0$ (red), $n_p = n_0/5$ (blue) and $n_p = n_0/15$ (green). In this simulation $n_{c0}/n_{h0} = 5$ and $T_h/T_c = 20$. The vertical dashed lines indicate the borders of the layer with $d = 5\lambda_{Dc}$.

where $Erf(z) = 2/\sqrt{\pi} \int_0^z \exp(-\varphi^2) d\varphi$ is the error function. This function basically equivalent to the integral of the Maxwellian energy distribution from zero up to the local potential value. By solving numerically this equation and applying the boundary values $\varphi(0) = \varphi_0$ and $\varphi(\infty) = \epsilon_{max} - 1$ we obtain the red dashed line in Fig. 2.1. The maximum energy of the protons at the end of the Debye-sheath will be $W_{max,QSA} \approx \epsilon_{max} - 1$, if $\epsilon_{max} \gg 1$ [46], which is confirmed in section 5.3.

Now we can include a proton layer with density n_p and study its effect on the initial electric field profile. Depending on the layer density we can have four situations: $n_p > n_0$, $n_p = n_0$, $n_{h0} < n_p < n_0$ and $n_p < n_{h0}$. The fourth case is a special case and it is described in [45]. Inside of the plasma the electric field can have different shapes, but it does not influence the acceleration as far as $d \gg \delta_E$, where $\delta_E \approx 5\lambda_{Dc}$. In the target in the calculation of λ_{Dc} we always take the value of the cold electron density in the layer. If $d \approx \delta_E$ and $n_p > n_0$, then the cold electrons are swept out from the layer, where a large positive charge is left behind.

The four initial electric field configurations are shown in Fig. 2.3. In the case of the black line the peak electric field is higher, because the cold electron density inside the layer is very high and $E(0)/E_0 > \sqrt{2 \exp(\varphi_0)}$ [48] if $n_{c0}/n_{h0} > T_h/T_c$. In these simulations we started with step-like density profiles and waited for several hundred ω_{peh}^{-1} , just like in Fig. 2.1. The protons were also immobile.

2.4.2 Plasma expansion regime of TNSA

The ions are not considered immobile, we are interested in the dynamics of the acceleration process and in the time evolution of the density and energy distribution of the protons. The experimental results, like the energy spectrum in Fig. 1.4, seemed to be consistent with an analytical model, called isothermal plasma expansion model [9], as we discussed in sections 1.3 and 1.1. Theory of plasma expansion is quite simple in the isothermal approximation, when the electron temperature is constant in time and space and only hot electrons are assumed to be in the plasma. The electrons can be described as an ideal gas and the ion motion is govern by the fluid equations, which have the form:

$$\left(\frac{\partial}{\partial t} + v_p \frac{\partial}{\partial x}\right) n_p = -n_p \frac{\partial v_p}{\partial x} \quad (2.21)$$

$$\left(\frac{\partial}{\partial t} + v_p \frac{\partial}{\partial x}\right) v_p = -\frac{q_e}{m_p} \frac{\partial \Phi}{\partial x} \quad (2.22)$$

where the subscript p means protons. The electric field can be calculated from the electron pressure:

$$E = -(\partial P_e / \partial x) / (q_e n_e) \quad (2.23)$$

By taking $P_e = n_e T_h$ and $n_e = n_p$ (quasi-neutrality) we obtain the analytical solution for density and velocity profiles of protons:

$$n_p = n_0 \exp(-1 - x / (C_s t)) \quad (2.24)$$

$$v_p = C_s + x / t \quad (2.25)$$

where $C_s = \sqrt{T_h / m_p}$ is the proton acoustic speed, which is equal to the speed of the rarefaction wave [35]. This wave separates the unperturbed plasma from the downstream expanding plasma. This is illustrated in Fig. 2.4, where the density profiles are shown for two time moments in one- and two-temperature plasma. The starting position of the dashed lines is always at $-C_s t$, which is the position of the rarefaction wave in the one-temperature plasma. In the 1T case it needs $20 / \omega_{pi}$ time to reach the end of the plasma, where $\omega_{pi} = C_s / \lambda_D$, because the total length of the plasma is $L_p = 20 \lambda_D$. In the 2T plasma this wave is slower and the density profile is also different because of the cold electrons, but the density scale length evolves in the same way as in the 1T case.

We can easily obtain the self-similar electric field using Eq. (2.24) and Eq. (2.23), which gives $E_{ss} = T_h / (C_s t) = E_0 / (\omega_{pi} t)$. This electric field is correct inside of the expanding proton plasma, where the neutrality assumption is relevant. At the proton front the neutrality condition is not fulfilled, there is always a charge separation present.

In order to obtain the peak electric field at the proton front, we investigate the proton front velocity. This can be calculated, as it is suggested in [9], by knowing that at the proton front the local electron Debye-length, $\lambda_D \exp[(1 + x / C_s t) / 2]$ is equal to the proton density scale length, $C_s t$. From this equation we obtain that $v_{p,front} = 2C_s \ln(\omega_{pi} t)$, which implies that the peak electric field is twice the self-similar electric field, $E_f = 2E_0 / (\omega_{pi} t)$.

A more precise expression, validated by a hydro code, is given in [9], where $E_{out}(x = 0) = E_0 \sqrt{2 / \exp(1)}$ but only for a 1T plasma. In the 2T case the initial peak electric field is $E_{out}(x = 0) = E_0 \sqrt{2 / \exp(-\varphi_0)}$, see Eq. 2.13. The time evolution of the peak electric field is shown in Fig. 2.5, where $n_{c0} / n_{h0} = 5.25$ and $T_h / T_c = 20$ in the 2T case. The full lines show the modified expression given by Mora [9], which we write as:

$$E_f = \frac{2E_0}{(2 \exp(-\varphi_0) + \omega_{pi}^2 t^2)^{1/2}} \quad (2.26)$$

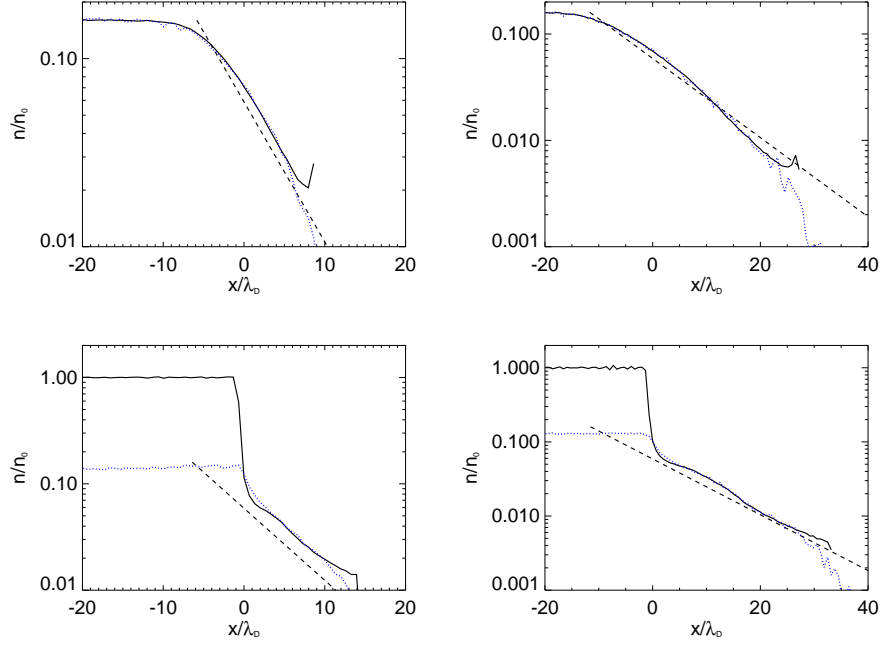


Figure 2.4: The density profiles of protons (full black line) and hot electrons (dotted blue line) at $\omega_{pi}t = 6$ (left) and $\omega_{pi}t = 12$ (right) in one- (upper row) and two-temperature plasma (lower row). The hot electron density and temperature is the same in both simulations. The dashed lines represent Eq. (2.24).

which is valid at any time. For $t = 0$ it gives the peak electric field in a charge separation only with hot electrons [32, 48]. The lower values measured in the simulations is attributed to the electron cooling, which is not included in the model. By knowing the time dependent peak electric field, the proton front velocity can be easily calculated, which has the form:

$$v_f = 2C_s \ln \left(\frac{\tau}{\sqrt{2e^{-\varphi_0}}} + \sqrt{\frac{\tau^2}{2e^{-\varphi_0}} + 1} \right) \quad (2.27)$$

where $\tau = \omega_{pi}t$. Using this formula the time dependency of many other quantities can be obtained, which we can find in [9]. The most important is the expression for the proton energy spectrum:

$$\frac{dN}{dW} = \frac{n_{h0}C_s t}{\sqrt{2WT_h}} \exp(-\sqrt{2W/T_h}) \quad (2.28)$$

where W is the kinetic energy of the protons and their density is equal to the density of hot electrons.

Assuming non-relativistic motion the cut-off energy of the distribution (maximum energy) can be easily deduced from Eq. (2.27):

$$W_{max} = 2T_h \left[\ln \left(2 \frac{\tau}{\sqrt{2e^{-\varphi_0}}} \right) \right]^2. \quad (2.29)$$

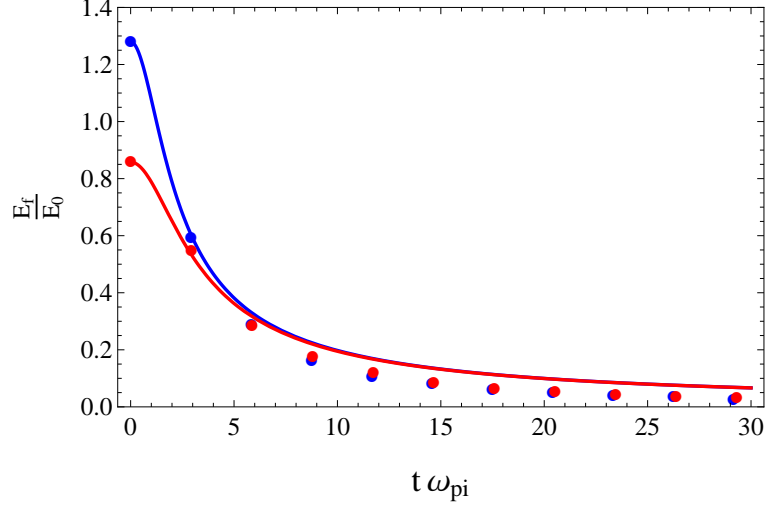


Figure 2.5: The peak electric field is shown with dots in 1T (red) and 2T (blue) plasma. The full lines are given by Eq. 2.26.

The energy spectrum measured in experiments were very similar to Eq. (2.28) and the maximum energy estimations using Eq. (2.29) were also in good agreement with the measurements if the acceleration time was chosen correctly. Unfortunately this time is not known exactly, a good choice seemed to be the 1.3 times the laser pulse duration.

In the reality the plasma expansion is more adiabatic than isothermal, because there is no infinite source of hot electrons, especially after the laser pulse. The adiabatic plasma expansion is not treatable fully analytically [34, 33], mainly because the adiabatic constant is not known for a Maxwellian momentum distribution. Recently the adiabatic constant equal to 3.0 has been found, for which an analytical solution can be derived from the hydrodynamic approach [67]. However in this case a step-like (water-bag) energy distribution of the electrons is a requirement. A scaling law was given for the hot electron cooling in the case of a finite thermal plasma in [35], where the author also gives the time duration of the isothermal phase of the expansion, when the hot electron temperature is nearly constant, therefore the isothermal model holds. This acceleration time is approximately the time needed for the rarefaction wave to reach the end of the plasma: $t_{acc} \approx L_p/C_s$.

The electron cooling in the adiabatic phase can be estimated by using energy conservation principles. The change in the thermal energy of the hot electrons is equal to the work done by the electric field on the electron fluid. This can be written in a mathematical form [35]:

$$\frac{1}{2}N_e \frac{dT_h}{dt} = - \int_{-\infty}^{\infty} T_h n_0 \frac{\partial v_e}{\partial x} dx \quad (2.30)$$

where N_e is the total number of electrons and v_e is the electron velocity. The electrons are co-moving with the protons, therefore we can use Eq. (2.25) to evaluate the right hand side, which will result in $N_e T_h/t$. Solving this simple differential equation the cooling rate is immediately given:

$$T_h(t) \propto t^{-2} \quad (2.31)$$

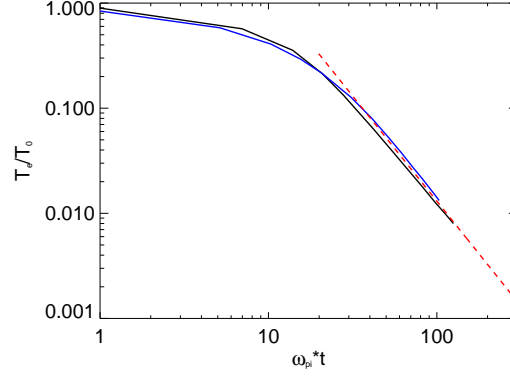


Figure 2.6: The global hot electron temperature in 1T (black) and 2T (blue) plasma from the simulations presented in Fig. 2.4. The dashed line is described in the text.

This expression is compared to the simulation results in Fig. 2.6, where the dashed line is Eq. (2.31), shifted with L_p/C_s along the horizontal axis and the initial temperature is set to $T_{h0}/3$, because some cooling happens also in the isothermal phase. The picture clearly shows that the significant cooling starts after $\omega_{pi}t = 20$, which is the traveling time of the rarefaction wave through the plasma and it is the same in 1T and 2T cases.

Starting from the Eqs. (2.21,2.22) we could derive the proton velocity and density as functions of space and time by assuming that the temperature is constant in space and time. With these conditions the self-similar electric field can be easily obtained from the electron pressure. Let us assume that the temperature is not constant in space and we do not know anything about the electric field. Using Eq. (2.23) we can express the electron density as:

$$n_e = \frac{1}{q_e} \frac{\partial P_e}{\partial \Phi} \quad (2.32)$$

After some mathematical manipulation of Eqs.(2.21,2.22) we can arrive to the equation [38]:

$$\frac{d\Phi}{d\xi} \left(\frac{q_e}{m_p} + C_s \frac{\partial C_s}{\partial \Phi} \right) + C_s = 0 \quad (2.33)$$

where $C_s = (1/m_p)(\partial P_e/\partial n_e)$, a different definition of the proton acoustic speed, and $\xi = x/t$ is the similarity parameter. In the parentheses there is basically the total energy (kinetic and potential) change over the change in the potential. Obviously it must be positive, which is the case in the one-temperature plasma. If this ratio is negative then Eq. (2.33) gives multiple valued solutions for the potential, which is unphysical. The condition for such a situation is:

$$\frac{\partial C_s^2}{\partial \Phi} + 2 \leq 0 \quad (2.34)$$

In a two-temperature plasma the electron density can be written as in Eq. (2.9), which leads to the acoustic speed:

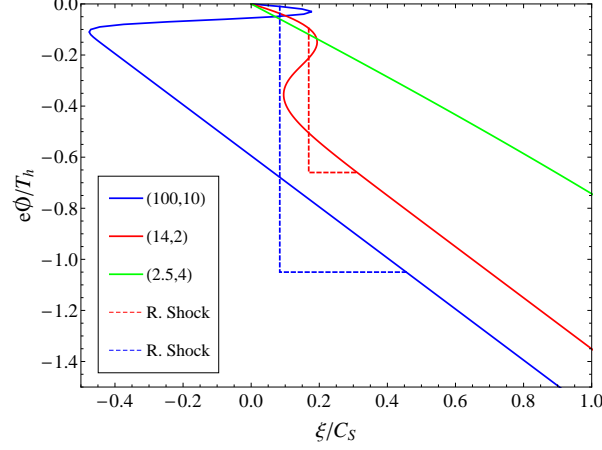


Figure 2.7: The numerical solution of Eq. (2.33) for $(T_h/T_c, n_{c0}/n_{h0})$ shown in the parentheses. With dashed lines the physical potential profiles are shown in the rarefaction shock.

$$C_{s2} = \left(\frac{1}{m_p} \frac{n_c + n_h}{n_h/T_h + n_c/T_c} \right)^{1/2} \quad (2.35)$$

After plugging this expression into Eq. (2.34) and evaluating the derivatives we find that for $T_h/T_c \geq 5 + \sqrt{24}$ the inequality becomes true. In this case the potential has a singularity, which triggers the formation of a rarefaction shock. The velocity of this shock is approximately C_{s2} , the so-called effective sound speed [68], which can be written as $C_{s2} = aC_s$, where

$$a = \frac{\sqrt{1 + n_{c0}/n_{h0}}}{r} \quad (2.36)$$

and r is defined in Eq. (2.11). In the case $n_h/n_c = 0$ and $T_h/T_c \gg 1$, $a = \sqrt{T_c/T_h} \ll 1$ [41]. The numerical solution of Eq. (2.33) is shown in Fig. 2.7 for different hot and cold electron parameters. The physically correct potential-profile can be obtained from the Hugoniot curve together with the mass-, energy- and momentum-conservation equations [38, 40]. The sharp potential-drop means a very localized and strong acceleration of the protons, which results in a significant peak in the energy distribution, but only in the low energy part [40], around $W \approx T_h$.

As we can see in the 2T plasma the rarefaction wave is slower and the initial electric field is stronger. These effects are confirmed and their consequences are presented in chapter 5.

2.4.3 Other acceleration mechanisms

Beside the TNSA, which we address in our work, there are several other mechanisms which lead to ion acceleration mostly at the front side of the target. These schemes predict small longitudinal energy spread and higher energy, but the transversal properties are questionable due to different instabilities which may occur. Let us first see what happens at the target front side for moderate laser intensities. As the linearly polarized light pushes the electrons at the front the ions are also pushed by the strong charge separation field; this process is known as hole

boring [2]. The velocity of the moving ion front can be estimated by applying the conservation of momentum and mass, which gives:

$$\frac{u}{c} = \left(\frac{n_c}{2n_{pe}} \frac{Z m_e}{M} \frac{I \lambda_L^2}{1.37 \cdot 10^{18}} \right)^{1/2} \quad (2.37)$$

where n_{pe} is the electron density at the pushing surface, M is the ion mass and Z is the charge state.

If the target is thick the hot electrons can not turn back from the rear surface in time to partially neutralize the positive charge, where the electrons are swept out by the light pressure. In this case small Coulomb-explosion can happen, which result in short, energetic ion bunches which gain additional velocity from the explosion [69]:

$$\frac{u_{sw}}{c} = \sqrt{\frac{2\Phi_p}{Mc^2}} \quad (2.38)$$

where $\Phi_p = mc^2(\sqrt{1 + a_L^2/2} - 1)$ is the ponderomotive potential. Finally the maximum velocity of the ions $v_{max} = u + 1.5u_{sw}$, which is in agreement with the simulations [69]. For higher intensities ($\approx 10^{21}$ W/cm²) the hole boring process becomes stronger and the ion energy can be higher than in the TNSA. In this regime a new mechanism shows up, the radiation pressure acceleration (RPA). In this case the Mach number ($u/C_s \geq 1.6$) is high and the ions pushed at the front propagate in the form of a shock-wave reflecting almost all of the ions in its way in the forward direction. Thus the reflected ions will have the velocity $2u$ [70]. With linearly polarized laser this mechanism is not so efficient, because the ions accelerated during the TNSA ruin the mono-energetic feature of the RPA. However there is one extreme case, when the target is very thin and the laser intensity is high (10^{21} W cm⁻²), which leads to an enhanced TNSA acceleration; it is called the laser break-out afterburner (BOA) [71]. In this case the target becomes quickly relativistically transparent and the laser pulse can further accelerate the ions behind the target via a Buneman-like instability. The 1D simulation result shows is a train of short mono-energetic bunches, but there is no experimental evidence yet.

In the RPA regime the undesired background of TNSA-accelerated ions can be avoided by using circularly polarized laser. In this case a constant push separates the electrons from the ions at the front, which are accelerated by the static electric field [72]. The problem is that circular polarization at this intensity is a challenging process and still requires improvements. In the limit of thin foils the laser accelerates all the ions in the laser path and the foil is pushed as a whole (the so-called Light-Sail regime). In this case the accelerating force scales linearly with the laser intensity and numerical simulations have predicted relativistic ions with GeV per nucleon. This kind of acceleration exists only in simulations [73].

3 Particle-in-Cell code, numerical aspects

The particle-in-cell (PIC) simulation codes have become powerful tools in the laser plasma modelling. The plasma expansion and other plasma behaviors can be also simulated using hybrid fluid codes, where the particle distributions are described by a given function (Maxwell-Boltzmann distribution). In this case the fluid equations (equation of motion and continuity) are coupled with the Poisson equation and solved numerically assuming thermal equilibrium everywhere in the plasma. Kinetic models, like Vlasov solvers and PIC codes, calculate the particle distribution self-consistently and do not assume that the distributions remain Maxwellian. In a Vlasov code the momentum distribution (usually Maxwellian) is evaluated in time and the particle densities are calculated from the integration of this function. The advantage is the noiseless output, but it needs a large memory because of the required high resolution of the velocity phase-space. Even for a problem reduced to a 1D geometry it typically needs 2 or 3 velocity components in order to incorporate the appropriate electron motion and its coupling to the Maxwell's equations. The PIC technique is more economical, easy to implement and suitable for the study of kinetic and non-Maxwellian effects.

3.1 General description of a PIC code

Simulating a plasma would mean the calculation of motion of each individual particle (ion or electron) interacting through the Lorentz force, which requires to sum up all of the electric and magnetic field vectors produced by the particle charges. In a high density plasma the number of particles in a few tens of micrometers length (1D) is more than 10^{20} , which is impossible to treat on any computer. A good idea is to represent $\approx 10^{17}$ particles (or less in higher dimensions) as one macroparticle. This simplification is still not enough to run such a simulation, because it is still too costly to calculate the fields at the particle positions created by all other particles in each time step. An easier way to calculate the fields is the integration of the Maxwell's equations, which requires charge and current density. Because these are not known analytically we have to use a numerical method, which is based on the discretization of space and time. Therefore the space is represented as a grid with well defined grid cells and grid points, where the field values are calculated.

The basic four steps taken in each simulation cycle are presented in Fig. 3.1. First, if there are initial fields defined, the particle movement is calculated using the well-known leapfrog integration method. Then the new positions and velocities of the particles are known, which are used to recalculate the charge and current densities in the plasma. At this step an interpolation method has to be chosen, because the fields are defined on the grid, but the particles are inside a cell, between the grid points. Details about the particle shapes, weighting and their effects can be found in [74]. The next step is to solve the Maxwell's equations, which provide the electric and magnetic fields strengths at the grid points. Again, we have to weight these fields back to the particles in order to apply to forces and push them further.

The accuracy depends on how fine we define the grid or how many macroparticles we load into the simulation. An issue arises, how reliable and stable is a PIC code if interpolation func-

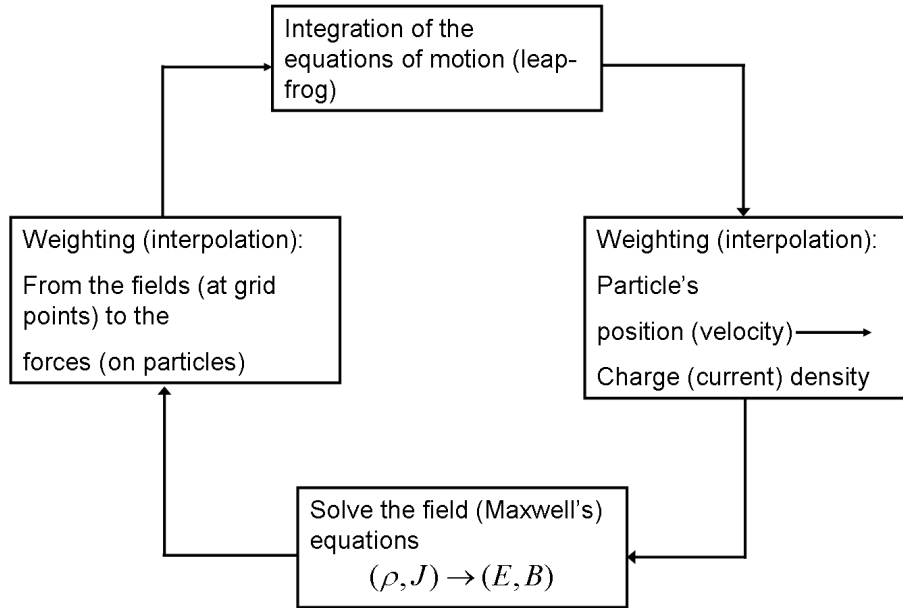


Figure 3.1: Sketch of one cycle of a PIC simulation.

tions are used, which can alter the physical distributions and lead to perhaps incorrect results [75].

3.2 Numerical errors, instabilities

A very powerful approach for periodic systems is to use Fourier transformation on all grid quantities. It provides spatial spectral information on ρ (charge density), J (current density), E (electric field), ϕ (potential), B (magnetic field) and it makes easier to solve the equations, because the Laplace operator is replaced by $-k^2$, where k is the wave number and the time derivative becomes a multiplication with the frequency, ω . In the case of discrete fast Fourier transformation (FFT) the general equation is

$$G(k_n) = \Delta x \sum_{j=0}^{N_G-1} g(X_j) e^{-ik_n X_j} \quad (3.1)$$

where G can be any field quantity, Δx is the grid size, $X_j = j\Delta x$ and N_G is the number of grid points. In order to obtain the field values in the real space we have to apply an inverse FFT, after the operations in the ω and k space, which has the form:

$$g(X_j) = \frac{1}{L} \sum_{n=-N_G/2}^{N_G/2-1} G(k_n) e^{ik_n X_j} \quad (3.2)$$

where $L = N_G \Delta x$ is the length of the simulation box and $k_n = n(2\pi/L)$. As we can see the N_G number defines also the spectral resolution, which means that we can not represent all of the wavelengths in the plasma, if L/N_G is larger than the minimal wavelength in the system. In [75] it is shown that the effect of the discrete spatial grid is to couple density perturbations and forces

at wave numbers which differ by integer multiples of the grid wave number $k_g = 2\pi/\Delta x$. With other words, the particles in a PIC simulation interact not only with each other, but also with the grid. This effect is called aliasing, because the perturbations (or oscillations) with a wavelength different from $p2\pi/k_g$, where p is an integer, will appear as a wave with wave number pk_g and its amplitude will be artificially increased. This effect is also called grid heating and it is the strongest for the wavelengths shorter than the grid size, therefore in a correct simulation the minimum physical wavelength has to be resolved by the grid.

Very often (and also in our case) the important wavelength is much smaller than the physical scale lengths of the processes, which we intend to simulate and the required grid size results in many million grid cells. In this case a coarser grid can be applied only if the number of particles per cell is increased and higher order weighting is used. By this technique the steep jumps in the current and charge density between the grid points are smoothed out, therefore the high frequency amplitudes of the Fourier spectrum are strongly reduced. There is a good analogy of this in the analysis of sampled time series. If one does not sample often enough, then differing frequencies become indistinguishable. This can be improved by low-pass filtering the signal before sampling, and the role of the particle shape functions is similar in the PIC simulations. Basically we sample charge between the grid points, which is equivalent to using a finer grid.

With higher order interpolation of the fields we can achieve the same effect: the high frequency components are eliminated from the spectrum and the numerical aliasing effect is reduced. Of course there is always a better solution to improve the accuracy by decreasing the grid size, which requires more computational power or time. If the high frequencies originate from the statistical noise of the granulated charge density, then using this smoothing technique is a good choice. First the smallest physical wavelength has to be estimated which can occur in the system, then the grid size can be set such that this wave is reproducible with the applied interpolation. If the higher order particle shapes are also used (with the same order, as we show later), then Δx can be much larger than the wavelength in the plasma, which is the Debye-length.

As an example we show how the Poisson equation is solved using the FFT (Eqs. (3.1,3.2)) on the charge density scalar field. The potential is obtained from the equation

$$\phi(k) = \frac{\rho(k)}{\epsilon_0 K^2} \quad (3.3)$$

where

$$K = k \left[\frac{\sin(k\Delta x/2)}{k\Delta x/2} \right] \quad (3.4)$$

and the electric field

$$E(k) = -i\kappa\phi(k) \quad (3.5)$$

where

$$\kappa = k \left[\frac{\sin(k\Delta x)}{k\Delta x} \right] \quad (3.6)$$

Here we obtain the analytical continuous limit when $k\Delta x \rightarrow 0$. The expressions Eqs. (3.4,3.6) also hold for the time derivation, thus now we can write the Maxwell's equations in vacuum

$$\frac{\partial B}{\partial t} = -\nabla \times E \quad (3.7)$$

$$\frac{\partial E}{\partial t} = c^2 \nabla \times B \quad (3.8)$$

in the wave number and frequency domain:

$$\Omega B = c\kappa \times E, \Omega E = -c\kappa \times B \quad (3.9)$$

where we neglect the particle current and $\Omega = \omega \sin(\omega\Delta t/2)/(\omega\Delta t/2)$. By eliminating E and B from Eqs. 3.9 we arrive to the dispersion relation of the electro-magnetic wave on a grid, which in two dimensions has the form:

$$\left(\frac{\sin(\omega\Delta t/2)}{c\Delta t}\right)^2 = \left(\frac{\sin(k_x\Delta x/2)}{\Delta x}\right)^2 + \left(\frac{\sin(k_y\Delta y/2)}{\Delta y}\right)^2 \quad (3.10)$$

Obviously ω has to be real, which happens to be if:

$$\frac{1}{(c\Delta t)^2} < \left(\frac{1}{\Delta x^2} + \frac{1}{\Delta y^2}\right) \quad (3.11)$$

or $c\Delta t < \Delta x/\sqrt{2}$ for $\Delta x = \Delta y$, which is also called the Courant criterion. This is the main criterion which has to be fulfilled in any electro-magnetic (EM) simulation. This is the result of the centered time integration scheme, which is illustrated in Fig. 3.2. It is the same leapfrog method which is used to advance particle position and velocity.

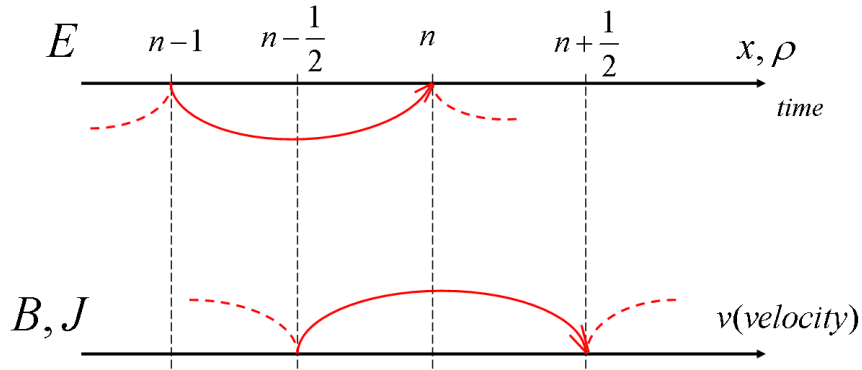


Figure 3.2: Time integration scheme of the field and particle quantities in an EM simulation.

In order to better understand the stability of a PIC code we show the dispersion diagram in Fig. 3.3, where Eq. (3.10) is plotted for the 1D case. These curves represent the phase velocity of the waves normalized to the speed of light, with different k number and for different time steps. As we can see for time steps, which do not satisfy the Courant criterion the simulation becomes unstable (the ω is imaginary) and the phase velocity approaches a minimum value when $\Delta t \rightarrow 0$. If the simulation contains relativistic particles they can travel faster than the

light on the grid which results in numerical Cherenkov radiation. This is the same effect what we can observe in the reality, when in a medium the light has velocity lower than c , because of the physical properties of the material, and relativistic electrons emit light. The difference is that in a PIC simulation the electrons do not slow down after emission, hence the energy is not conserved, but it increases.

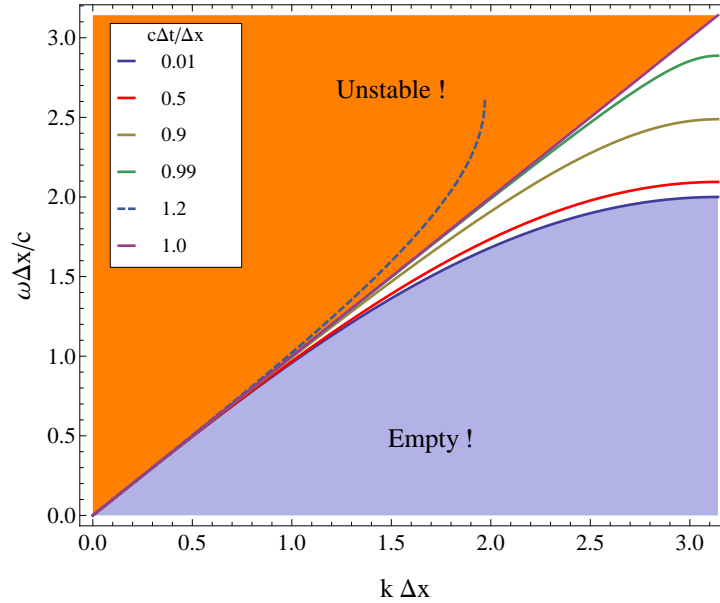


Figure 3.3: The dispersion curve of an EM wave on the grid for different time steps.

In higher dimensions this dispersion diagram is different and the phase velocity depends also on the direction of the k vector. It can be shown that the deflection from the diagonal curve (violet line in Fig. 3.3) is the strongest along the edges of the grid cell. The numerical Cherenkov emission is only relevant in 2D or 3D, because in 1D by choosing $\Delta t = 0.99\Delta x/c$ we are always at the safe side and the phase velocity is very close to the speed of light, even for short wavelengths. The heating caused by this numerical effect can be eliminated by using filtering [76], when the slow, high frequency waves are taken out from the simulation. The higher order particle shapes (or field interpolation) reduces not only the grid heating, but also the artificial Cherenkov emission.

We mentioned already that when the particle quantities (position, velocity) are advanced in time the fields are weighted such that fields at the closest grid points (nodes) contribute to the motion proportionally to their distance from the given particle. In this case the momentum of particles is conserved, but the field energy microscopically can change. However the macroscopic total energy changes by amounts small compared to other energies of interest, for example kinetic energy. There is another way to push the particles and to conserve their energy if the time integration is accurate. If the fields are not weighted, but their value is taken from the node for all particles which are at a distance less than $\Delta x/2$ from that node, then the energy is conserved. In this case the force is basically calculated from the gradient of the field energy. If we choose this option, the momentum is not conserved which can have an effect for instance on the temperature of a particle beam. The cold electrons (or ions) passing through a neutralizing background can become hot while its drift velocity (or directed energy) decreases.

3.3 Features of the VORPAL code

The code has all the usual capabilities of PIC codes and there are some special modules included, which we do not need for our problem, like ionization, collision, secondary electron emission from metal surfaces, etc. Beside that it is fully parallelised with high performance capable of performing large simulations in a relatively short time. The numerical issues presented in the previous section can be found also in this code and will be tested in the next section. Here we mention those features, which help us to deliver a physically correct and reliable result. The input file has an Xml-like structure and syntax. The output is saved in *.h5* format which can be visualized using the VorpableView (given with the software) or other plotting and data analysing software which support the *.h5* format. Our visualization tool is IDL 8.0.

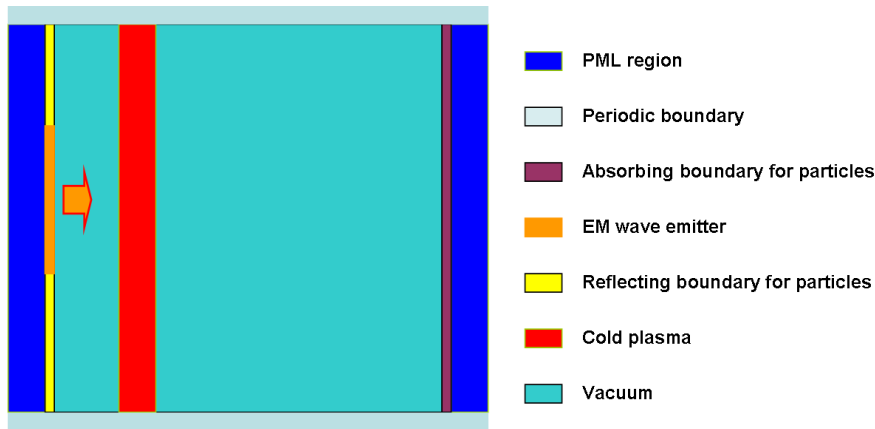


Figure 3.4: The layout of a 2D simulation box, including the boundaries.

Let us start with the boundaries used in our 2D simulations (in 1D they are the same in the longitudinal direction). The usual simulation box is presented in Fig. 3.4. The usual length and width is about $50 \mu\text{m}$ which is enough to study the longitudinal and transversal acceleration of ions. The PML (perfectly matched layer) has an important role, because it is responsible for the absorption of the outgoing (right end) and reflected light waves from the over-dense plasma (left end). If there were periodic or reflecting boundaries, then the whole simulation domain would be filled up with the laser wave. In the transverse direction first we put periodic boundaries, because it is more useful for the converge study. For a more realistic TNSA simulation we can place PML regions also on the transversal boundaries, thus the fields can go away in each direction, like in the reality. We can simulate a real infinite space if we include special reflecting boundaries for the electrons in transverse direction. These are the so-called diffuse boundaries, which reflect particles with a Maxwellian velocity distribution, where the temperature is given by the user in the input file. In this way the hot electrons, which would spread out on the whole target surface, now are re-emitted into the plasma with cold temperature, which is the initial electron temperature ($\approx 1 \text{ keV}$), therefore the total charge is conserved (quasi-neutral plasma).

The initial physical parameters (electron density, temperature, laser intensity, etc.) will be given later in the corresponding chapters. Now we present the main idea behind the PML region. It is an artificial absorbing layer for wave equations, commonly used in numerical methods to simulate problems with open boundaries. The idea is that the gradient operator ($\partial/\partial x$) is replaced by $(1 + i\sigma(x)/\omega)^{-1}\partial/\partial x$, wherever it appears in the wave equations. The function $\sigma(x)$ is a positive function of x and in VORPAL it is defined as:

$$\sigma(x) = \sigma_0 \left| \frac{x - L_{pml}}{\Delta x} \right|^s \quad (3.12)$$

where L_{pml} is the width of this layer and σ_0, s can be freely defined, depending on how fast or effectively should be the wave absorbed. We understand how it works if we apply the new operator on the wave form $\exp[i(kx - \omega t)]$, which is transformed to: $\exp[i(kx - \omega t) - \frac{k}{\omega} \int_x \sigma(x') dx']$, where the wave propagates in the $+x$ direction ($k > 0$). The amplitude of the wave will decrease after each grid cell it passes. The L_{pml} has to be set carefully, because if the wave goes through and enters the other PML layer or gets reflected with a significant amplitude, the effect will be reversed ($k < 0$) and it can end up with a much larger amplitude than the initial one.

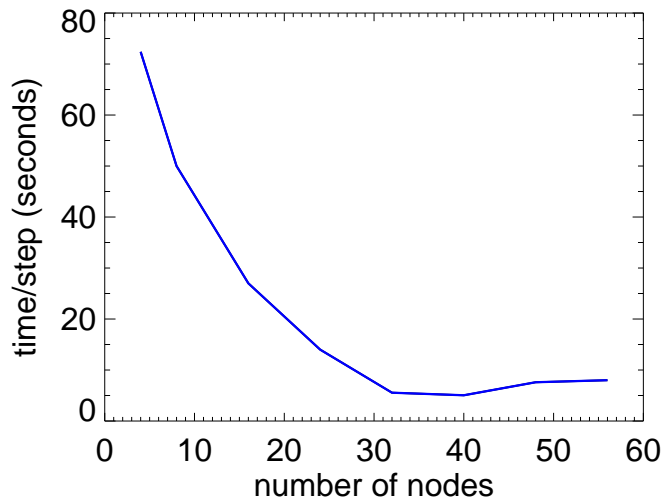


Figure 3.5: The performance of the parallel 2D simulation as a function of the number of nodes.

The code has a parallelized executable, which is compatible with MPI platform. A significant speed-up can be achieved up to 32 nodes for our typical 2D setup. The scalability test is shown in Fig. 3.5, where we can see that the optimum speed is reached around 30 nodes. If more nodes are used, then the communication between the nodes requires more time which results in a slower simulation. In Vorpil we can choose between the momentum and energy conserving algorithms of the field solvers, but we always use the first one, because we are mostly interested in the velocity phase-space of particles and the parameters we choose such that the energy change is insignificant on the time scale of the simulation.

3.4 Convergence study

Before we check the convergence of the laser-plasma simulations let us see the effect of the higher order filtering (particle shape and field interpolation). The third order interpolation is the most commonly used, which we also use in our simulations and compare with the linear one. In these 2D EM simulations the whole domain is filled with uniform plasma and periodic boundaries are used everywhere. The size of the simulation box is $100\Delta x$ in each direction. In this scenario the only wave length which has to be resolved is the electron Debye-length. Usually

this we can not resolve in a 2D simulation, because the ratio of the characteristic acceleration length and the cold electron Debye-length is on the order of 10^3 or more. It results in 10^6 grid cells, which is very time consuming on 32 nodes. Therefore we are interested in the behavior of a thermal plasma when the grid size is larger than the electron Debye-length.

In Fig. 3.6, left, we can see how powerful the cubic filtering can be. Even if the grid size is 40 times larger than the Debye-length and the number of particles per cell (PPC) is only 2, the grid heating is by orders of magnitudes lower than in the linear case. The time is normalized to the electron plasma frequency $\omega_{pe} = (n_0 q_e^2 / m_e \epsilon_0)^{1/2}$, where n_0 is the plasma density. In the right side plot in Fig. 3.6 we observe finer changes of the temperature. The grid heating can be suppressed with linear filtering only with very high resolution, $\Delta x = 4\lambda_D$, but there is still some significant increase of energy (red line). Using the cubic filtering in the same simulation (brown line) the heating is not observable. With higher PPC and resolution the simulation with linear interpolation is more correct and the grid heating is negligible, but it would require a huge amount of memory and long run time for a 2D TNSA simulation. The CPU time for the brown line was 4 hours, while in the case of the blue line it was 27 hours, which means a factor of 7 increase in speed.

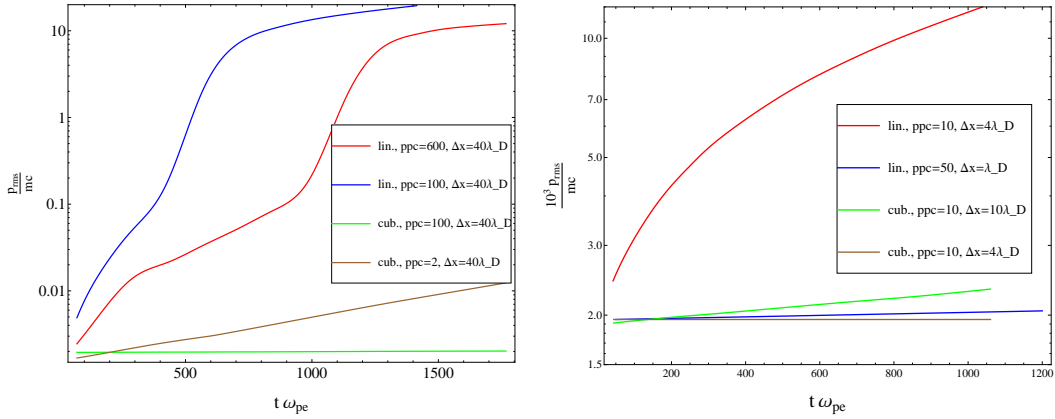


Figure 3.6: Left: The RMS momentum of electrons from a thermal plasma simulation with 1 keV initial electron temperature. Right: The same simulation, but with different simulation parameters.

As the laser pulse interacts with the plasma relativistic electrons are produced, which can contribute to the numerical heating via the Cherenkov field emission. As we mentioned earlier the cubic filtering eliminates this problem as well, as it is confirmed in Fig. 3.7. With a non-relativistic temperature the grid heating results in relatively small (only factor of two in 4 ps) with linear interpolation because of the high resolution (black line). If we increase the temperature to a relativistic value, the heating appears again, which can be explained by the Cherenkov radiation. The same simulation with cubic filtering shows no heating effect (blue line). The simulation domain was a square with $50\lambda_D$ long edge.

As we have seen the distance between the grid points can be 20-40 times larger than the Debye length and the simulation can still be stable with the filtering technique. Unfortunately in TNSA we have different scale lengths which must be resolved on the uniform grid (the adaptive grid is not implemented in VORPAL for plasma simulations). One important characteristic length is the laser skin depth which is larger than the cold electron Debye length ($l_s > \lambda_{Dc}$, because $c > v_{th}$). The hot electron production depends on how the skin depth is resolved by the grid. On

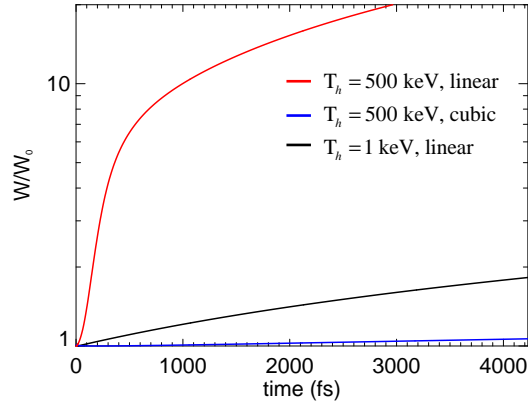


Figure 3.7: Time evolution of the total energy over the initial total energy in time for different initial electron temperatures. The simulation parameters: $\Delta x = 4\lambda_D$, $PPC = 50$. Here $1/\omega_{pe} = 2.1$ fs.

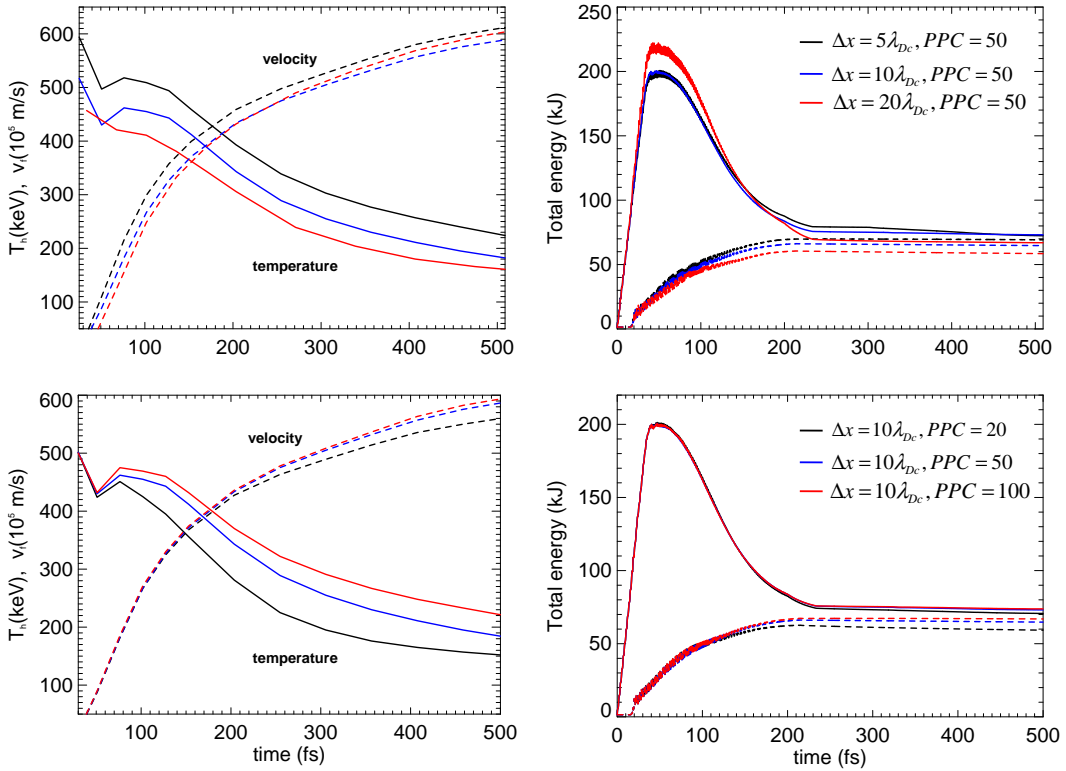


Figure 3.8: Left: The longitudinal hot electron temperature and proton front velocity versus time. The color legend is the same as in the right picture. Right: The total energy of the system (full line) and the total energy of particles (dashed line).

the other hand we want to resolve the proton acceleration at the rear side of the target, where the density gradients are quite steep due to plasma expansion. Therefore we have to perform a convergence test, where we can check how the physical processes depend on the small changes of the simulation parameters.

First let us see the effect of the grid size by keeping the PPC constant in 2D simulations. The result is presented in Fig. 3.8, upper row. As we expected for different grid sizes the temperature of heated electrons (T_h) is not the same and convergence is also not visible yet. The convergence

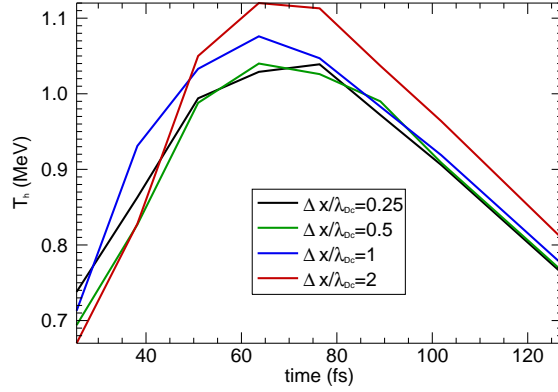


Figure 3.9: The hot electron temperature over time for different spatial resolutions in 1D simulation.

becomes apparent, when we change only the PPC, as is it shown in Fig. 3.8, lower row. In this case the initial T_h is the same always, but the cooling and ion acceleration is different because as the plasma expands the ion front is less resolved if the PPC is lower. In these simulations the laser pulse duration is 200 fs as we can see in the evolution of the total energy. After the laser pulse is off the total energy of the system is constant, as it should be, or it can slightly decrease because of the absorbing boundaries (see Fig. 3.4), which indicates that the energy is conserved and no numerical heating is present. The electron cooling in the case of the lowest PPC is slightly slower than with more particles. It can be attributed so the grid heating, which is very small in this case. The cubic filtering was used in all of the simulations and the target is a neutral plasma with immobile ions in the first half of the target (front side) and with protons in the second half.

In all of our 2D simulations we use the shifted-Gaussian pulse shape, which provides an almost constant hot electron pressure at the beginning of the expansion. There is not much difference between the simulation with this pulse and with the normal Gaussian, as we will show in section 6.3.4. However, by getting closer to the conditions assumed in the analytical model we can have a greater confidence in the study of the transverse divergence of the protons.

We could see the convergence over the grid size only in 1D simulations. The laser pulse duration was 100 fs with peak intensity $4 \cdot 10^{19} \text{ W/cm}^2$ and the target setup was the same. The resulting temperature of hot electrons is shown in Fig. 3.9. The difference between the temperature values is not so large as in 2D and it increases faster, because the transversal degree of freedom is missing. Between the simulations with grid size $\lambda_{Dc}/4$ and $\lambda_{Dc}/2$ there is no significant difference which indicates the convergence. Such a high resolution we can not use in the 2D simulations, but the undergoing acceleration on the rear side of the target is correct with a coarser grid as well.

3.5 Optimal 2D simulation setup

As a conclusion of the previous section we can use the grid size $\Delta x = 10\lambda_{Dc}$ and $PPC \approx 20$ as a good initial parameter-set for a 2D simulation. The results are correct (if the simulation is

not too long) and the run time is less than one day. The main parameter which defines the grid size is the cold electron Debye-length. In principle we can increase its value by increasing the initial electron temperature or decreasing the target density, but there are three criteria which has to be fulfilled. The hot electron temperature has to be much higher than the initial one (T_c), the target density must be higher than the critical density (n_{cr}) and the laser wave length must be at least 20 times longer than the grid size, otherwise it would not be well resolved by the grid. These quantities are defined by the laser parameters: intensity (defines T_h) and wave length (defines n_{cr}). A simple drawing in Fig. 3.10 helps to better understand the trade-off between these requirements.

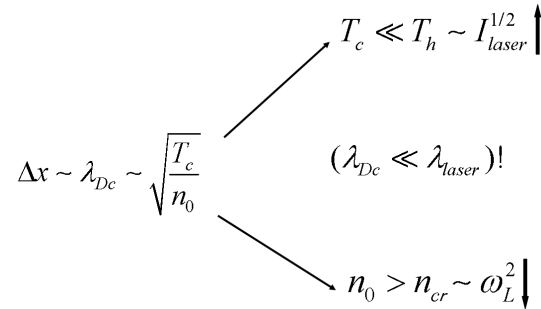


Figure 3.10: A sketch to illustrate the possibilities of increasing the cold electron Debye-length.

The initial cold Debye length can be made larger by increasing T_c , but the situation is not improved, because the hot electron Debye length will be longer, because the $T_h/T_c \approx 100$ ratio has to be fulfilled, thus we need more grid cells to ensure enough place for the acceleration behind the target. By increasing too much the laser intensity we can enter the radiation pressure acceleration regime, which is not in our region of interest.

Moreover λ_{Dc} can not be set too large, because the laser wave length must be always much longer than the grid size, which is proportional to the cold Debye-length. In principle we can increase the laser wave length, but it has an effect on the plasma density (see Eq. (2.6)). For a longer λ_L the cold Debye-length becomes automatically larger, if the n_0/n_{cr} is kept the same. Let us take an example, where n_0/n_{cr} is fixed. If the plasma density we set a factor of N lower, then λ_L , λ_{Dc} , l_s and Δx will be \sqrt{N} times larger. The hot electron temperature will be $\approx N$ times larger, if the intensity remains unchanged, because $a_L \propto I_L \lambda_L^2$ (see Eq. (2.2)). By decreasing n_0 the density of laser-produced hot electrons will be also lower, at least by a factor of \sqrt{N} (N times lower density, but \sqrt{N} times larger laser skin depth). Thus the resulting hot electron Debye-length is $N^{3/4}$ times larger, which means a longer simulation domain. In order to have the same acceleration length the laser intensity has to be reduced by a factor of $N^{3/2}$, but then the condition $T_h/T_c \geq 100$ might not be fulfilled.

As we can see, by increasing the cold electron Debye-length of the target plasma we have to change the parameters of the laser pulse in order to obtain the same physical results. The hot electron Debye-length will be inevitably effected such that the simulation domain has to be increased. Finally we can not achieve any significant speed-up of our simulation.

In 1D simulations we do not have such issues with stability and numerical errors. The grid size can be even 10 times smaller than the cold electron Debye-length and the simulation finishes in a reasonable time.

4 One-dimensional, electromagnetic simulations

4.1 TNSA from a proton plasma

In the experiments the target is usually a metal foil (for example Aluminum or Gold) with a thickness of the order of $10\ \mu\text{m}$. The accelerated ions which are observed actually originate from the few nm thin contamination layer on the target surface. It can contain many different atoms (mostly Carbon and Hydrogen) which react differently to the electric field of the Debye-sheath. In theory we always have to simplify the real world in order to model and understand the undergoing physics. As a first step we study the proton acceleration in the case of an over-dense purely proton plasma interacting with a high intensity laser pulse.

In the following we present results from two simulation setups where only the laser pulses are different. The setup and the measured physical quantities, at the time when the peak intensity reaches the target, are shown in Table 4.1. The laser pulse reaches the plasma 20 fs after the beginning of the simulation. For the initial plasma density we have to choose a value higher than critical density (n_{cr}), which is fixed. Our freedom in choosing this parameter is limited, because for very high density, the initial Debye-length is very small, which requires a very high grid resolution. We have a much broader range of choice for the initial electron temperature, but it has to be much lower than the laser-produced hot electron temperature. Its realistic value is not well known, therefore in the laser community $T_c \propto 1\ \text{keV}$ is a compromise [51, 53]. This value is typically much smaller than T_h and it is large enough to allow the usage of a coarser grid, which results in a faster simulation.

| Physical quantity | Pulse 1 | Pulse 2 |
|--|--------------------------------------|------------------------------------|
| Time duration (t_L) | 115 fs | 196 fs |
| Laser intensity (I_{L0}) | $10^{23}\ \text{W/m}^2$ | $6.08 \cdot 10^{22}\ \text{W/m}^2$ |
| Normalized laser amplitude (a) | 2.7 | 2.09 |
| Debye length (λ_D) | $7.79 \cdot 10^{-8}\ \text{m}$ | $5.25 \cdot 10^{-8}\ \text{m}$ |
| Target density (n_0) | $2.43 \cdot 10^{28}\ \text{m}^{-3}$ | $2.0 \cdot 10^{28}\ \text{m}^{-3}$ |
| Plasma frequency (ω_{pi}) | $7.945 \cdot 10^{13}\ \text{s}^{-1}$ | $9.3 \cdot 10^{13}\ \text{s}^{-1}$ |
| Hot electron temperature (T_h) | 400 keV | 250 keV |
| Hot electron percentage (n_{h0}/n_0) | 16% | 25% |
| Acoustic speed of protons (C_s) | $6.19 \cdot 10^6\ \text{ms}^{-1}$ | $4.89 \cdot 10^6\ \text{ms}^{-1}$ |
| Initial potential-drop (φ_0) | 0.164 | 0.256 |

Table 4.1: Parameters of 1D simulations and calculations

In Fig. 4.1, left, the electron velocity phase-space is shown at an early time of the interaction. The short electron jets, with a time separation half of the laser period, propagate through the

plasma and turn back at the rear side. They can escape from the neutral plasma until their kinetic energy is fully transformed into the potential energy. This is how they build up a potential-well, which gives rise to the strong electric field. In the left picture we can see the effect of the electric field induced by the charge separation at both sides of the plasma, which triggers the plasma expansion. The RPA is clearly visible in the first half of the plasma, where a short, mono-energetic bunch evolves and gets accelerated as it is described in section 2.4. At this low intensity the number and energy of protons accelerated via RPA is quite low compared to other energetic protons coming from the back side of the target.

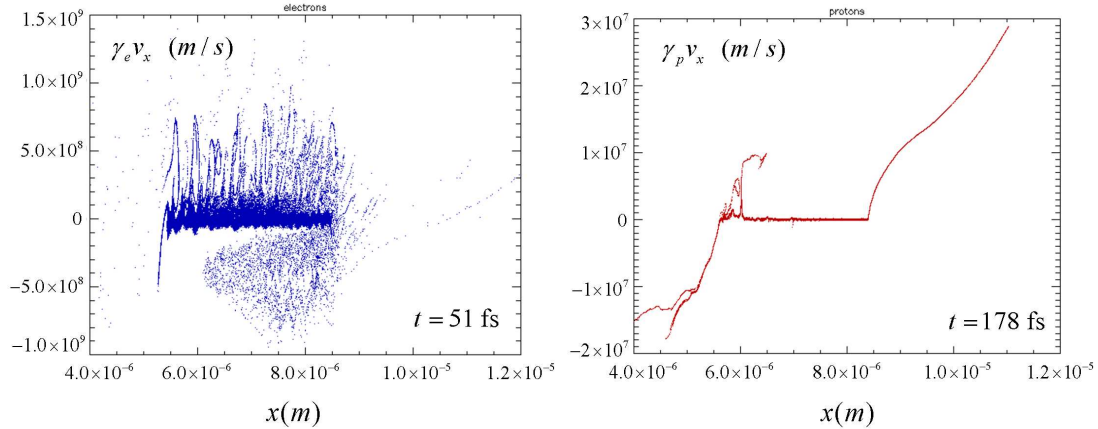


Figure 4.1: Velocity phase-space of electrons (left) at 51 fs and of the protons (right) at 178 fs from the simulation with the Pulse 1.

In these simulations the grid size is half of the initial Debye-length and the total length of the simulation box is $25 \mu\text{m}$, which corresponds to 15000 grid cells. The number of particles per cell is 200, but it is increased when we simulate a long time scale. The initial electron temperature is 2 keV and the plasma density is 10 times the critical density, which corresponds to $2.43 \cdot 10^{28} \text{m}^{-3}$.

At the front side of the target we place a preplasma with a scale length $0.1 \mu\text{m}$ and with a total length $0.5 \mu\text{m}$. With this artificial preplasma, with an exponential density profile, the laser absorption is somewhat increased [77] and we avoid the step-like plasma density profile, which is never the case in the reality.

4.2 Comparison with theory

In this section we use the analytical plasma expansion model [9] to interpret and understand the simulation results, where the laser pulses from Table 4.1 are used. The laser parameters are chosen such that the total energy of the two pulses is the same. In all of the plots presented here the physical quantities are normalized by the values shown in Table 4.1. The target thickness is $3 \mu\text{m}$ and consists of electrons and protons. The simulation results are compared to the analytical formulas presented in the section 2.4.2.

4.2.1 Proton distribution

First let us see the time evolution of the proton front velocity, which is the most important observable in laser the acceleration. The results are shown in Fig. 4.2. As we can see the ac-

celeration can be divided in three parts: laser phase, until the laser-plasma interaction lasts; quasi-isothermal plasma expansion and adiabatic phase, when the acceleration is much weaker and practically stops. In the laser phase the hot electron pressure increases, therefore the front velocity does not agree with the theory. After the laser is off the target still contains hot electrons, which sustain the isothermal condition until the time $L_t/(2C_s)$ (L_t is the target thickness), as we discussed in section 2.4.2. After this the electron temperature quickly drops and the acceleration depletes the hot electron energy, which means the end of the acceleration. Finally we can write the total acceleration time in the form:

$$t_{acc}^{1D} = t_L + \frac{L_t}{2C_s} \quad (4.1)$$

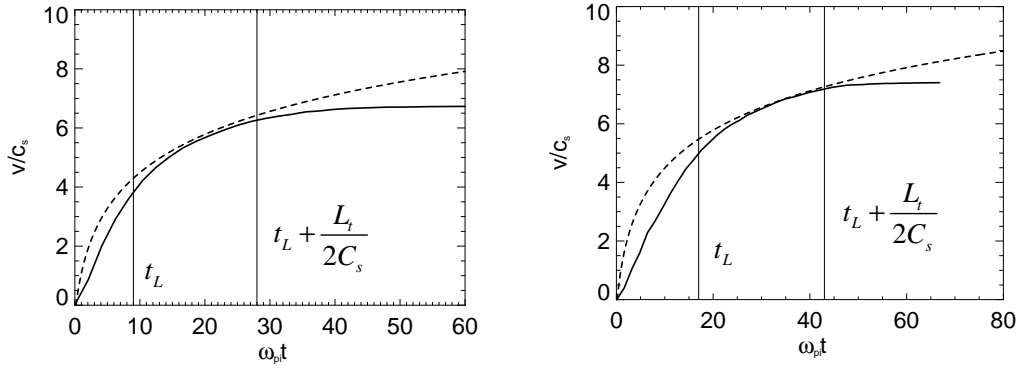


Figure 4.2: The maximum proton velocity during acceleration for Pulse 1 (left) and Pulse 2 (right). The dashed lines represent Eq. (2.27).

The energy spectra of the protons outside of the target is shown in Fig. 4.3. As we can see the agreement is very good if we use the above defined acceleration time. One can notice that for the shorter pulse the final cut-off energy is larger. This is because the total energy of the two pulses is the same, but their duration is different. The longer pulse has a lower intensity at the beginning of the expansion, when the TNSA field is strong (see Eq. (2.26)). In this case the plasma interacts with a lower electric field of the laser (due to the Gaussian intensity profile of the laser pulse) for a longer time. It results in a lower electron temperature and in a weaker acceleration. In the case of the shorter pulse the hot electron temperature is higher in the active part of the expansion (first 10 proton plasma periods, see Fig. 2.5). The number of accelerated protons is slightly higher in the case of the longer pulse, because the hot electron density is higher.

As we can see in the 1D simulations the acceleration time is much longer than the $1.3t_L$, which is used in the experiments. This is because in 1D the electrons are forced to move along a line, the transversal degree of freedom is not present. In higher dimensions the hot electrons spread out on the rear surface when they escape the target and most of them do not contribute to the acceleration, or only for a short time.

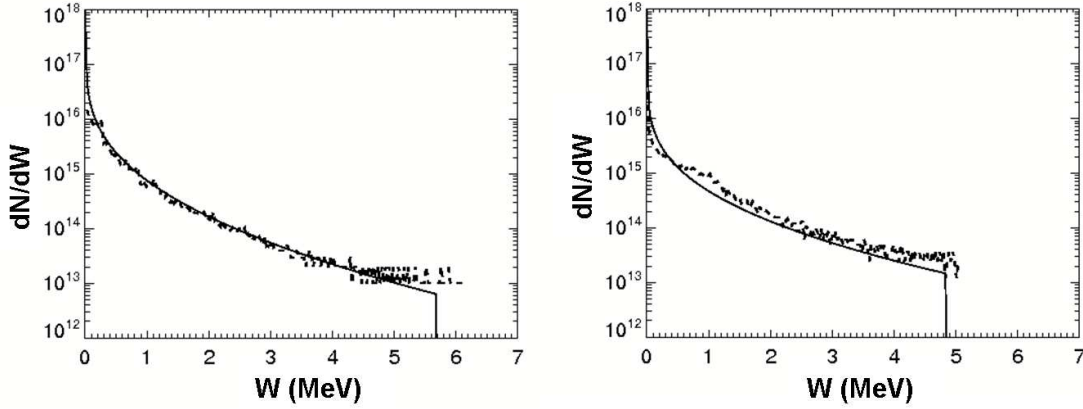


Figure 4.3: The energy spectrum of protons for Pulse 1 (left) and Pulse 2 (right). The full lines represent Eq. (2.28) and (2.29).

4.2.2 Electron distribution and cooling

In Fig. 4.4, left, the electron spectrum is shown from the simulation with Pulse 1. At an early time (black line) the number and energy of hot electrons is very small. The cold electron population is barely visible, because their temperature is 2 keV with maximum energy ≈ 15 keV. When the laser pulse reaches the plasma a part of the electrons gain much larger energy than the maximum energy of the cold electrons. At the peak of the pulse the temperature reaches its maximum value (red line) and a cold and a hot electron populations are distinguishable. The border between them is not clear, there is no sharp separation between them, but we define 100 keV as an energy border between the hot end cold electrons. This value is used throughout the thesis. The cold electrons are also heated up (the slope is not so steep) and in later times the hot electrons cool down (blue line).

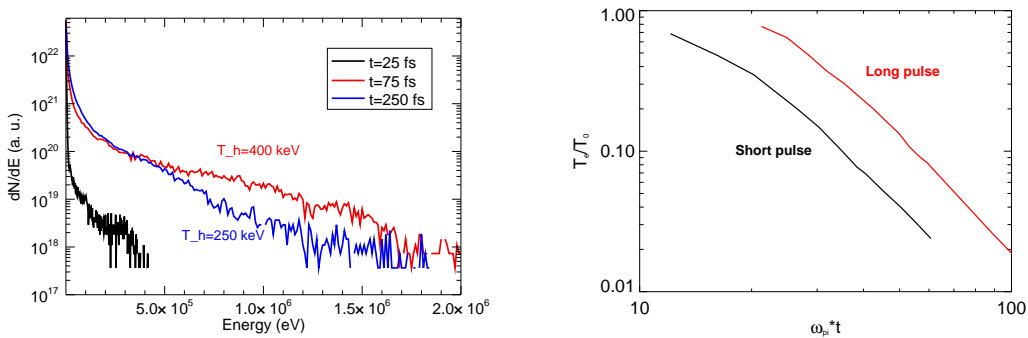


Figure 4.4: Left: The electron energy spectrum at different time instances from the simulation with Pulse 1. Right: The mean kinetic energy of electrons with energy higher than 100 keV for Pulse 1 (black) and Pulse 2 (red).

The cooling process can be followed in time if we calculate the mean kinetic energy of the hot electrons at each time. The result is presented in Fig. 4.4, right, for the shorter and longer

pulses. Here the cooling rate is the same in both cases and the best fit shows $t^{-2.1}$, which is close to the theoretical prediction, Eq. (2.31).

An important issue, which can be investigated with PIC simulations, is the velocity distribution of the electrons. We are interested if the hot electrons are co-moving with the protons or not. In our definition co-moving term that the mean velocity of electrons is higher than their RMS (or thermal) velocity,

$$v_{rms}(x) = \sqrt{\langle (v(x) - \langle v(x) \rangle)^2 \rangle} \quad (4.2)$$

The results are shown in Fig. 4.5, where the electron and proton mean velocity is compared to the thermal velocity of electrons. Initially the electron temperature is high, especially outside of the plasma, where only hot electrons are present (see left picture). Later the hot electrons cool down and the temperature becomes non-uniform. This effect has been shown and explained in [36]. In the right picture of Fig. 4.5 the co-moving feature of the electrons is confirmed, their mean energy is equal to the proton velocity everywhere and their thermal velocity is 10 times smaller than at the beginning.

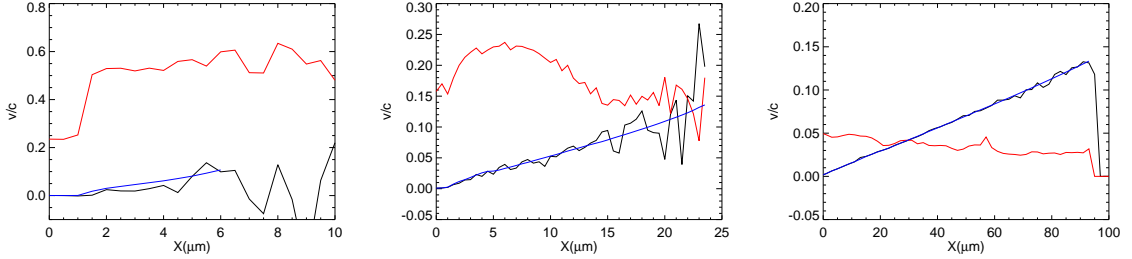


Figure 4.5: The electron rms velocity (of all electrons) in red at $\omega_{pi}t=18$ (left), $\omega_{pi}t=50$ (middle) and $\omega_{pi}t=200$ calculated by Eq. (4.2). In black the mean velocity is plotted. The blue line represents the proton velocity in space. The $x = 0$ point is the middle of the target. These are results of laser-plasma simulation with Pulse 1.

We can now calculate the electron temperature when the proton front reaches a certain position, x_f . For this we should estimate the distance from the target until the proton front has to fly in order to have a cold co-moving electron population in the plasma. Let us call the temperature T_{xf} , when the proton front is at x_f . The path of the proton front is a sum of two parts:

$$x_f = x_{iso} + x_{adi} \quad (4.3)$$

where x_{iso} is the distance traveled during the isothermal phase and x_{adi} is the distance traveled until the temperature reaches T_{xf} . By calculating the integral of Eq. 2.27 in the limit $\omega_{pi}t \gg 1$, we obtain:

$$\chi_{iso} = \sqrt{2}\tau_{acc}(\ln(\sqrt{2}\tau_{acc}) - 1) \quad (4.4)$$

where $\chi_{iso} = x_{iso}/\lambda_D$ and $\tau_{acc} = \omega_{pi}t_{acc}$. The second part of the path is simply the final front velocity times the cooling time: $x_{adi} = v_f(t_{acc})t_{cool}$, where t_{cool} is calculated from the scaling law $T_{xf}/T_0 = (t_{acc}/(t_{cool} + t_{acc}))^2$. In the units of normalized quantities it can be written as:

$$\chi_{adi} = 2 \ln(\sqrt{2}\tau_{acc})(\sqrt{\vartheta} - 1)\tau_{acc} \quad (4.5)$$

where $\vartheta = T_0/T_{x_f}$ and T_0 is the temperature of hot electrons at the end of the isothermal phase, which is approximately 1/3 of the initial value (see Fig. 2.6). Finally we can write the distance x_f , where the electron temperature ϑ times smaller than at the beginning, normalized to the initial Debye-length and using that $\tau_{acc} \gg 1$ and $\vartheta \gg 1$:

$$\chi_f \approx 2\tau_{acc} \sqrt{\vartheta} \ln(\sqrt{2}\tau_{acc}) \quad (4.6)$$

In order to calculate exactly this value in the reality, three values are needed: the hot electron density, the hot electron temperature and the acceleration time. As an example we take for the hot electron density $n_h = 10^{27} \text{ m}^{-3}$ and for the temperature 3 MeV ($T_0 = 1 \text{ MeV}$). With these realistic values the hot electron Debye-length is $\lambda_D = 0.235 \mu\text{m}$ and the proton plasma frequency $\omega_{pi} = 4.16 \cdot 10^{13} \text{ Hz}$. We can assume that the laser pulse duration is $t_L = 500 \text{ fs}$, thus the acceleration time is $\tau_{acc} = 1.3t_L\omega_{pi} = 27$. If we are interested in the position of the proton front where the electron temperature is 1 keV, we can use Eq. (4.6), which gives $6226\lambda_D$ or 1.46 mm. If we want the temperature to be 0.1 keV ($\vartheta = 10^4$) then the proton front has to travel 4.63 mm. These distances are surprisingly small, for lower temperature they would be even smaller. In the reality the cooling rate is probably much slower. The scaling law derived in the plasma expansion model holds only for collision-less plasma, but at low temperatures the collision can become an important effect in the evolution of the electron phase-space. This phase of the expansion is beyond our scope and we can not treat it correctly in the simulation. Due to the large macro-charge of the virtual PIC particles the density at these distances can not be resolved.

4.3 Effect of the laser pulse-shape

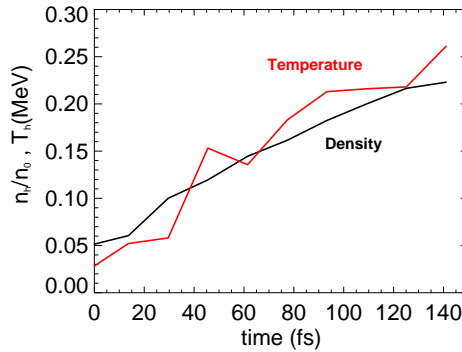


Figure 4.6: Time evolution of the hot electron temperature and density during the laser-plasma interaction with Pulse 2.

In simulations with a laser pulse the hot electron temperature and density change in time, therefore the accelerating field is also not constant. The maximum proton velocity deviates from the analytical prediction (see Fig. 4.2), it increases rather linearly than logarithmically in the laser phase. However the calculated maximum velocity agrees with the simulation taking the acceleration time defined in Eq. (4.1) and the electron parameters at the peak intensity. The increasing hot electron pressure is illustrated in Fig. 4.6 for Pulse 2. If we include the

time dependency of hot electron pressure in the plasma expansion theory the equations become analytically unsolvable.

Even if the laser intensity is constant over the whole pulse duration the hot electron parameters increase in 1D simulations. We try to look for a pulse shape for which at least initially the hot electron parameters are constant. In order to investigate the time development of the electron heating and the proton acceleration we performed simulations with three different pulses. The time profiles are shown in Fig. 4.7, where the electric field of the laser waves are described by the following expressions:

$$E_L = E_{L0} \exp\left(-\frac{(2t - t_L)^2}{t_L^2}\right) \cos(2\pi ct/\lambda_L) \quad (4.7)$$

$$E_L = E_{L0} \exp\left(-\frac{(2(t - t_L/3) - t_L)^2}{t_L^2}\right) \cos(2\pi ct/\lambda_L) \quad (4.8)$$

$$E_L = E_{L0} \cos(2\pi ct/\lambda_L) \quad (4.9)$$

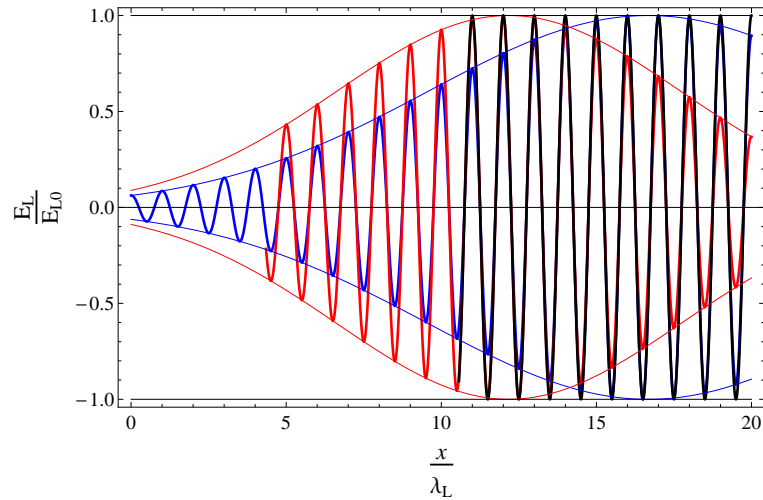


Figure 4.7: Intensity profile of the laser pulses: constant Eq. (4.9) -black, Gaussian Eq. (4.7) -red, shifted Gaussian Eq. (4.8) -blue.

In these simulations the target is $1.5 \mu\text{m}$ thick and it consists of immobile ions at the front ($1 \mu\text{m}$) and a thick proton layer at the back ($0.5 \mu\text{m}$). The initial plasma density is $2.57 \cdot 10^{28} \text{m}^{-3}$, which is 8 times larger than the critical density. The total energy ($9.33 \cdot 10^9 \text{J}$) and the peak intensity ($I_{L0} = 2 \cdot 10^{19} \text{W/cm}^2$) of the pulses is the same in all three simulations. Their time duration is different: 200 fs for the shifted Gaussian, 94.3 fs for the constant and 156.5 fs for the Gaussian pulse.

The evolution of hot electron density and temperature in time is shown in Fig. 4.8, left. The temperature and density is almost the same in the first half of the black and blue pulse, therefore the acceleration of the proton front is also very similar. The hot electron pressure in the late stage of the expansion has no significant effect, because of the $\propto t^{-1}$ time dependency of the electric field (see Fig. 2.5). The maximum energy of the protons is mostly determined by the initial temperature and density of the hot electrons. The proton front velocity is very close to the

analytical prediction Eq. 2.27, shown with the green dashed line and calculated for $T_h = 900$ keV, $n_{h0} = 5 \cdot 10^{27} \text{ m}^{-3}$ and $\varphi_0 = 0.2$.

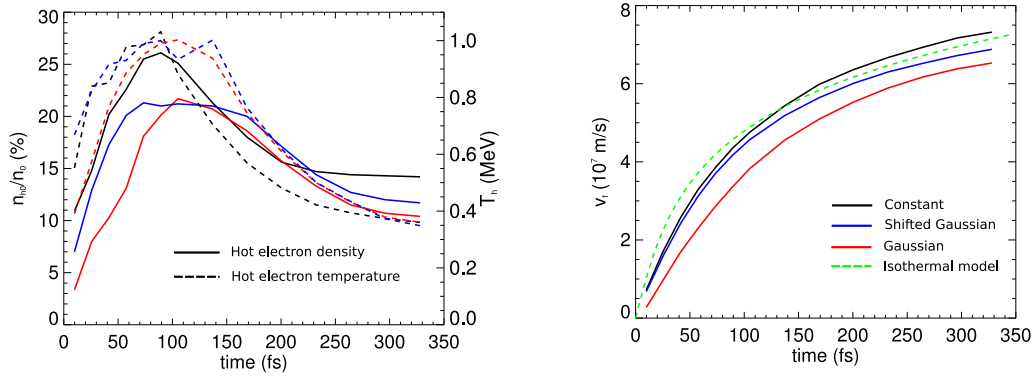


Figure 4.8: Left: The time evolution of the hot electron density and temperature. Right: Proton front velocity compared to Eq. 2.27. The color legend is the same as in Fig. 4.7.

The stochastic feature of the hot electron production does not allow us to compare precisely physical quantities measured in simulations with idealized analytical models. The very fine structure of the charge separation field at the rear surface is also difficult to study in these conditions. A very useful and easy approach is to perform plasma expansion simulations, where the hot electron parameters are well-known from the beginning and they are not changed by external forces (like a laser pulse).

5 One-dimensional, electrostatic simulations

In this chapter we are going deeper into the details of the two-temperature plasma expansion and we are getting closer to the reality by taking a double layer configuration of the plasma. As we know the target consists of bulk heavy ions and a much thinner hydrogen-rich contamination layer, where the protons come from. The laser pulse is neglected in this study, instead of the pulse length the plasma length will define the acceleration time. The Boltzmann distribution is imposed on electrons only in the initial condition, in the expansion and acceleration the electron kinetic effects are automatically included. It gives a more realistic results than the fluid or hybrid codes.

5.1 Double layer foil

The accelerating field on the target surface is created by the hot electrons, produced by the intense laser pulse. Initially the hot electrons recirculate in the target, their density is increasing and they are not in a thermal equilibrium, therefore the electric field is not constant. In our simulations we skip this chaotic phase of the acceleration and start with a sedate state of the plasma. The target is considered as a plasma with two electron populations, hot electrons and cold electrons with much lower temperature, but higher density. We set up a plasma where the charge separation is well described and the hot-to-cold electron pressure ratio is well known. In this case the problem is simplified and the constant electron parameters allow us to compare simulation results to analytical predictions. The challenge is to find the equilibrium density distribution of the electrons around the plasma surface. One attempt can be found in [34], but by fitting the potential inside the plasma with a parabolic function the system can not be neutral, the positive charge inside will be 15 % higher than the negative charge outside of the plasma. For the same purpose we use an exponential function, as suggested in [48]. In experiments and simulations [78] the usual density and temperature ratios are: $n_c/n_h \approx 100$ and $T_h/T_c \approx 100$, where the subscript c and h corresponds to cold and hot respectively. In the following we will consider two cases: only hot electrons are present in the plasma (1T) and two-temperature case (2T).

The basic build up of this work is presented in Fig. 5.1. The target consists of protons, heavy ions, which are considered immobile on the time scale of proton acceleration, and electrons. As we can see the 2T plasma is a multi-scale problem, because inside the plasma the cold Debye-length has to be resolved, while outside only hot electrons are present with $\lambda_D \gg \lambda_{Dc}$. Because of numerical limitations we do not use such high parameter ratios mentioned before, but in all of our 2T simulations the cold electrons dominate. The penetration depth of the electric field has a scale length very close to the hot (1T, Fig. 5.1, left) or cold (2T, Fig. 5.1, right) electron Debye length.

In our work we always assume that the proton density is equal to the total electron density (or density of the singly ionized heavy ions), because the number density of protons in organic

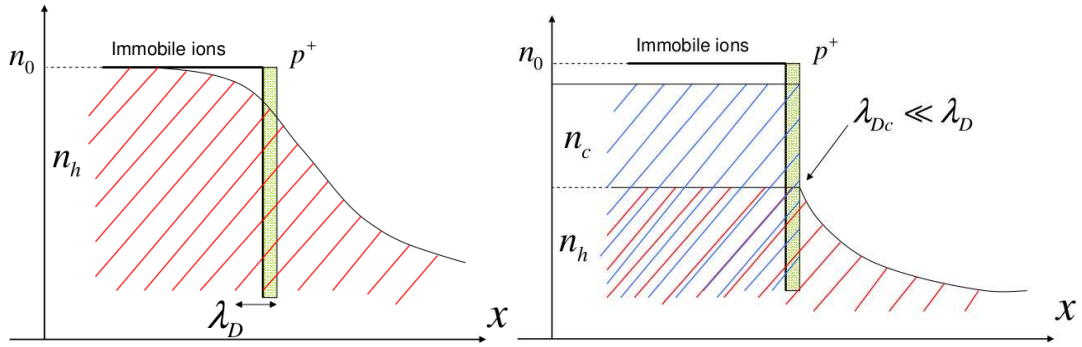


Figure 5.1: Sketch of the density profiles in a charge separation at the plasma surface for 1T (left) and 2T (right) plasma. The red color shows the hot electrons with temperature T_h and the blue shows the cold electrons with temperature T_c .

materials is close to the solid density ($\approx 10^{28} \text{ m}^{-3}$). It is confirmed with measurements [79], where the layer was analyzed by x-ray photoemission spectroscopy, which showed $\approx 1 \text{ nm}$ thick layer with hydrogen density $\approx 10^{29} \text{ m}^{-3}$. Another experiment [14] reports that the hot electron density, measured by an optical reflectometry technique, is only $\approx 10^{26} \text{ m}^{-3}$ at the axis of symmetry of the laser pulse. It means that in the TNSA the realistic proton density can be more than 100 times higher than the hot electron density.

5.2 Simulation setup

The protons are initially placed in the interval $x = [-d, 0]$, where d is the layer thickness. The ions are placed in the interval $[-L_p, -d]$, where L_p is the total plasma length. At $x = -L_d$ there is a reflecting boundary for particles and at the other end of the simulation box we place an absorbing boundary. In the 1D simulations high grid resolution and many macroparticles can be used, which means that the Debye-length can be well resolved and the statistical noise-level is very low. Numerical parameters: grid size $\Delta x = \lambda_{Dc}/4$, $n_0 = n_{c0} + n_{h0}$. In the 1T case $\Delta x = \lambda_D/10$. In some simulations we consider layer thicknesses 100 times smaller than the electron Debye-length. In these cases the grid resolution would be too high for our computer, therefore we keep the layer thickness equal to Δx , defined before, and we reduce the layer density such that the mass of the layer is the same as it would be if we had chosen $d = \lambda_{D(c)}/100$. The used time step: $dt = 0.04/\omega_p$ and the number of macro-particles per cell is 2000. The typical numbers for time step is 10^{-18} s and for grid size 10^{-10} m in the 2T plasma, while in the 1T case these number are about 50 times larger. The length of the simulation box is about 4 times the length of the electron cloud (L_e), which corresponds to $\approx 10^4$ grid cells. The electric potential and electric field are calculated by a Poisson solver implemented in VORPAL. The electric field at both ends of the simulation domain is set to zero.

The large number of grid cells is very demanded in this kind of simulation, especially in the 2T case, where the cold electron Debye-length is much smaller than the hot one. We have to resolve the smallest scale lengths, which means that in the regions where the hot electrons dominate the grid resolution is much higher than the required, because the grid is uniform. We have requirements on the number of macroparticles as well in order to ensure the physically correct output. In the next section we will see that in the Debye-sheath the electron density goes down as x^{-2} , which means that the number of macroparticles per cell is very small far from the

target and therefore the noise-level is higher. In some cases when n_{c0}/n_{h0} is high we choose a higher number than 2000 in order to have a smooth hot electron density profile outside of the plasma. Another important physical effect which gives a time limitation for simulation is the decreasing density of the proton front during plasma expansion. In [9] we find that n_p at the front is proportional to t^{-2} , which means that after some time the proton front is represented by one macroparticle in one cell and the density at this point can not decrease any further. The typical simulated time is a few hundreds of femtoseconds, which corresponds to $\propto 10^4$ (in 1T) and $\propto 10^5$ (in 2T) time steps.

5.3 Thin and thick proton layers

As we have seen the electric field inside the plasma has an exponential form (see Eq. 2.14) with a scale length equal to λ_D/r (for simplicity we neglect α). Therefore we introduce a dimensionless parameter:

$$D = r \frac{d}{\lambda_D} = \sqrt{1 + \frac{n_{c0} T_h}{n_{h0} T_c} \frac{d}{\lambda_D}} \quad (5.1)$$

where n_{c0} in our simulations will be equal to the cold electron density inside the target and $n_p = n_0$. From now on we use D to characterize the layer, which represents the ratio of the thickness d to the scale length of the penetrating electric field into the dense plasma.

Let us consider a layer which is much thinner than the penetration depth of the electric field into the target, $D \ll 1$. In this case the protons are accelerated as test particles, all of them feel the same field strength and finally they form a quasi-mono-energetic bunch. Its velocity can be estimated by integrating the electric field (Eq. (2.13)) from the plasma surface ($x = 0$) until the end of the electron cloud ($x = L_e$), which gives:

$$v_{max} = 2C_s \sqrt{\ln(1 + L_e/(\lambda_D \sqrt{2e^{-\varphi_0}}))} \quad (5.2)$$

where $C_s = \sqrt{T_h/m_p}$, m_p is the proton mass. This velocity corresponds to the kinetic energy $W_{max,QSA} \approx 6.5T_h$, which is in agreement with the analytical prediction[46, 11]: $W_{max,qsa} = (\epsilon_{max} - 1)T_h$, for $\epsilon_{max} \gg 1$. In our case ϵ_{max} is a fixed parameter, but in reality it depends on the fast electron generation during the laser-plasma interaction. For $\epsilon_{max} = 7.5$ the length of the electron cloud is $L_e \approx 60\lambda_D$ and $v_{max}/C_s \approx 3.8$, which is in good agreement with the simulation shown in Fig. 5.2.

In the opposite extreme case, $D \gg 1$, the protons are accelerated via plasma expansion [9], which can be described analytically up to the point when the adiabatic phase starts and the electron cooling becomes important [35]. This time is approximately the laser pulse duration, but in the case of an expanding plasma slab the acceleration time is $t_{acc} \approx L_p/C_s$, where C_s is the proton acoustic speed, which is equal to the speed of the rarefaction wave [35], as we have described it in section 2.4.2.

When the rarefaction wave reaches the middle ($\omega_{pi} t \approx 20$) of the plasma the hot electron temperature is already one third of the original value. After this the hot electron cool down quickly and the proton acceleration becomes weaker. The final front velocity can be estimated using the following formula [9]:

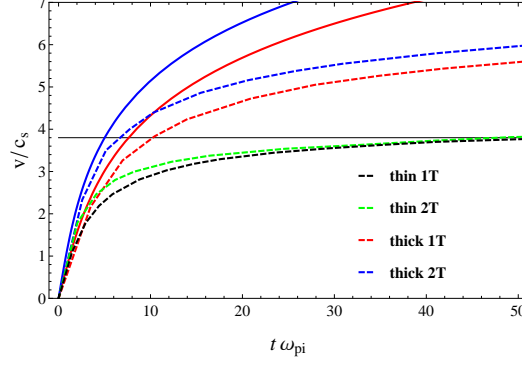


Figure 5.2: Maximum velocity of protons from simulations (dashed lines) compared with the analytical predictions (full lines). The red (1T) and blue (2T) color corresponds to the thick layer case, while the black (1T) and green (2T) represents the thin layer case (quasi-static acceleration, $D = 0.01$). The black full line is given by Eq. (5.2) and the red and blue full lines correspond to Eq. (5.3).

$$v_f = 2C_s \ln \left(\tau_{acc} + \sqrt{1 + \tau_{acc}^2} \right) \quad (5.3)$$

where $\tau_{acc} = \omega_{pi} t_{acc} / \sqrt{2e^{-\varphi_0}}$.

In Fig. 5.2 we can see that for $D = 20$ the electron cooling has a significant effect on the late stage of proton acceleration. The analytical model does not predict a final velocity for $t \rightarrow \infty$, while the simulation shows a converging proton front velocity.

5.4 Detachment of a thick layer

A proton layer at the rear side of a heavy target can detach only if the rarefaction wave reaches the point where the layer is in contact with the heavy ions. This wave in the 2T plasma for $T_h/T_c \gg 9$ behaves as a shock-wave [38] and it has an influence on the detachment. The properties of this shock have been studied by using a Boltzmann-Vlasov code [39]. The cold electrons slow down the rarefaction wave and modify the density profile of the protons.

In Fig. 5.3, left, the simulation results are shown in the case of 1T and 2T plasma, where $n_{c0}/n_{h0} = 9$ and $T_h/T_c = 200$. In the 2T case the proton density at $x = 0$ is equal to n_{h0}/e^a and behind it a steep drop shows up. The analytical expression from [9] can be generalized in the following form:

$$n(x) = n_{h0} \exp\left(-a - \frac{x}{C_s t}\right) \quad (5.4)$$

which is valid for the electrons as well, since they are co-moving with the protons if we neglect the small charge separation at the proton front.

One very important consequence of this shock-wave is that the proton velocity in the tail of the bunch at the time of detachment is not zero, but $\approx 0.59C_s$ [39, 40]. This effect can be seen in Fig. 5.3, right, where the dashed lines correspond to the velocity profile before the detachment and the full lines after the detachment.

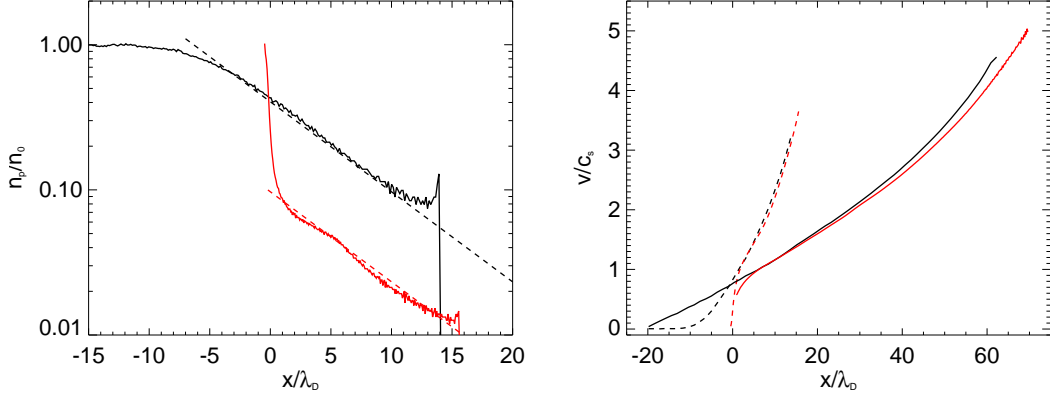


Figure 5.3: Left: The proton density profile (full line) is compared to the analytical prediction Eq. (5.4) (dashed line) in the 1T (black) and 2T (red) case, for $\omega_{pi}t = 7$. Right: The color legend is the same. The longitudinal velocity profile of protons is shown at $\omega_{pi}t = 7$ (dashed line) and $\omega_{pi}t = 18$ (full line). The dimensionless layer thickness is $D=20$.

The detachment time can be defined as $t_{det} \approx d/(aC_s)$. In the 1T case ($a = 1$) this time is always shorter than t_{acc} , because $d \ll L_p$. In the 2T case the detachment time can be longer than the acceleration time, $d/(aC_s) > L_p/C_s$, which requires the condition $d/L_p > a$. After detachment the energy conversion from electrons to protons is less efficient, therefore t_{det} should be always longer than t_{acc} , which is close to the laser pulse duration.

5.5 Intermediate regime

The acceleration in this regime has not been described up to now fully analytically. Our simulation results in a dependence on the dimensionless layer thickness are represented in Fig. 5.4. There is a smooth transition between the two regimes. In the case of a very thin layer the accelerated protons form a quasi-monoenergetic beam (pink line in Fig. 5.4) and in the case of a thick layer (black line) the spectrum is similar to an exponential energy distribution [9].

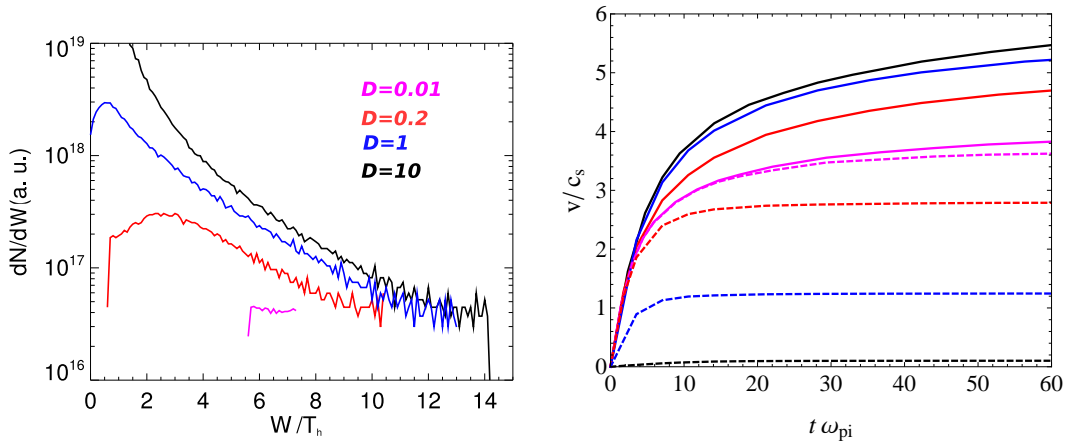


Figure 5.4: Left: Final energy spectra of protons for $D = 0.01$ (pink), 0.2 (red), 1 (blue) and 10 (black) in a 1T plasma. Right: The color legend is the same, but the full lines show the front velocities and the dashed lines show the corresponding mean velocities.

For intermediate thicknesses the proton bunch detaches from the target and gets accelerated in the static field until it reaches the position x_t , where the electron trapping takes place. This trapping process with the modified electric field is illustrated in Fig. 5.5. It is clearly visible that the electrons follow the proton bunch and partly neutralize it.

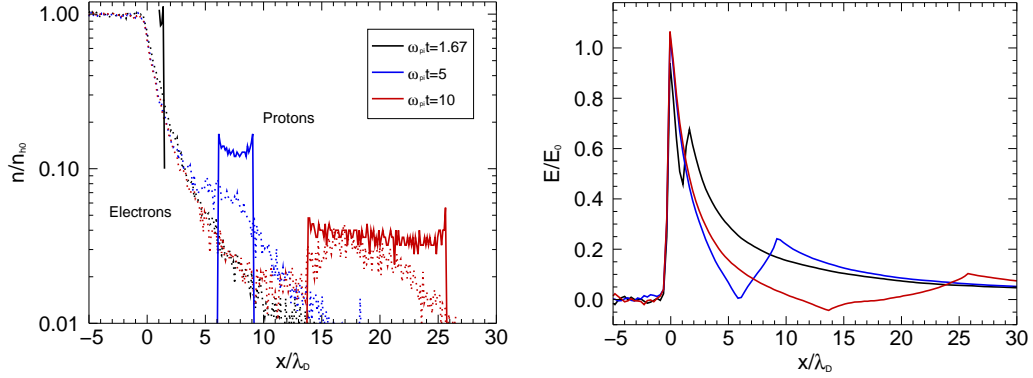


Figure 5.5: Left: Density profiles of electrons (dotted line) and protons (full line). Right: The corresponding electric field. Simulation parameters are: $D = 1$, $n_p/n_{h0} = 4$, $T_h/T_c = 20$.

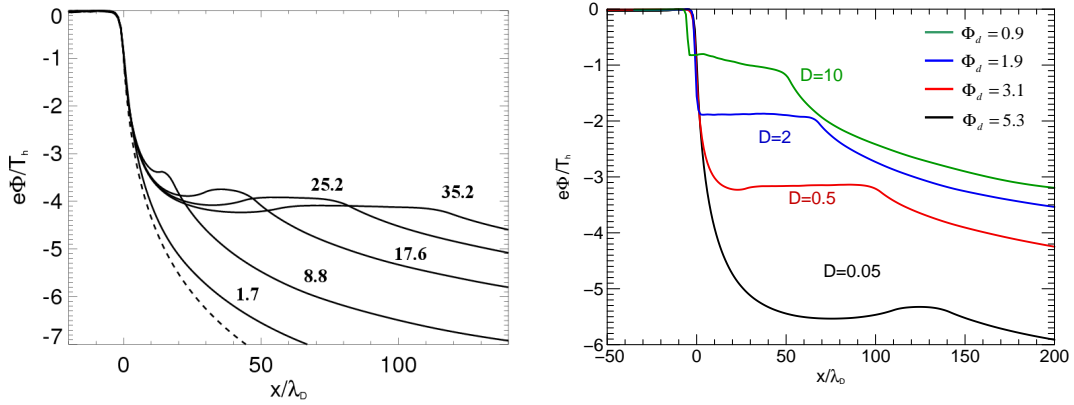


Figure 5.6: Left: Potential profile during the acceleration at given $\omega_{pi}t$ in 1T plasma for $D = 0.2$. The dashed line shows the initial profile (Eq. (2.10)). Right: The space structure of the potential for different layer thicknesses, illustrating the potential-drop, Φ_d .

In Fig. 5.6, left, we can see that a bump appears in the potential, which slowly smooths out. Later the proton bunch expands and due to the trapped neutralizing electrons the potential takes a constant value along the bunch (the flat region in the last curve). Thus between the plasma surface and the bunch tail evolves a potential-drop (Φ_d), which converges in time to a constant value. In Fig. 5.6, right we can see that this drop depends on the layer thickness. In order to estimate Φ_d we have to take a closer look at the potential profile between the heavy ions and the proton bunch. For this the Poisson equation has to be solved, which gives us the potential profile modified by the proton bunch. This problem has been solved in [44] by assuming that $n_{c0}T_c/(n_{h0}T_h) \ll 1$.

We are interested in the potential at the position where the electric field is zero, because this is when the electron trapping starts. In [44] this potential is given as:

$$\Phi_d = 2 \frac{T_h}{q_e} \ln \left(\frac{\sqrt{2} r n_{h0}}{D n_p} \right) \quad (5.5)$$

We can obtain the same expression using Eq. (6) from [45]. This expression predicts an infinite potential-drop for zero thickness, therefore we have to introduce a minimum layer thickness for which $\varphi_d = q_e \Phi_d / T_h = \epsilon_{max} - 1 = -\varphi_{max}$. On the other hand for thicker layers the potential-drop should be $\varphi_d = -\varphi_0$. With these corrections we find $d_{min} = \lambda_D n_p^{-1} \sqrt{2} / (\exp(-\varphi_{max}/2) - \exp(-\varphi_0/2))$ and we arrive to an expression:

$$\varphi_{dcorr} = 2 \ln \left(\exp(-\varphi_0/2) + \frac{\sqrt{2} n_{h0}}{n_p (D/r + d_{min}/\lambda_D)} \right) \quad (5.6)$$

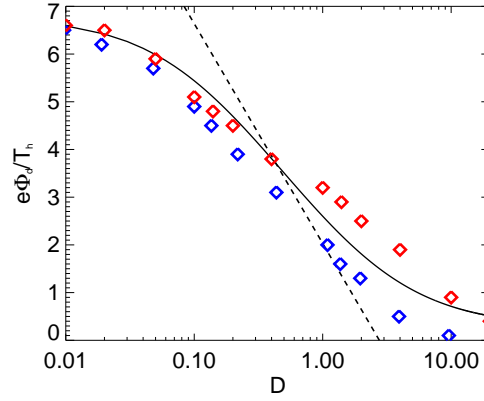


Figure 5.7: Potential drop measured from 2T simulations with $L_p = 4\lambda_D$ (blue) and $L_p = 20\lambda_D$ (red). The black full line represents Eq. (5.6) and the dashed line Eq. 5.5.

The simulation results are compared to Eq. (5.6) in Fig. 5.7. Here $n_c/n_h = 3$, $T_h/T_c = 20$ and we performed simulations for two plasma lengths. The dashed line shows the φ_d if the electron cloud would be infinitely long. The full line shows good agreement with the simulations in the small D region. In the case of thick layers the potential-drop is higher than it was at the moment when the electron trapping started (or the electric field has negative value), see Fig. 5.6, this is why we measured higher Φ_d than the theoretical prediction. In the case of the short plasma the electrons cool down faster, because their total energy is smaller. In Fig. 2.6 it was confirmed that the fast cooling of hot electrons happens after t_{acc} , which depends on L_p . If L_p is large then T_h remains unchanged for a longer time, while in a short plasma the temperature drops, which results in a smaller potential-drop.

5.6 Thickness-dependent energy conversion

The average energy of the protons in the case of thin layers will be equal to the potential drop, Φ_d . We are interested in the energy conversion from the hot electrons to the protons, which is the ratio of the final total proton energy and the initial total hot electron energy. Therefore the energy conversion for thin layers can be written as:

$$C_{thin} = 2\varphi_{dcorr} \frac{n_p}{n_{h0}} \frac{d}{L_p} \quad (5.7)$$

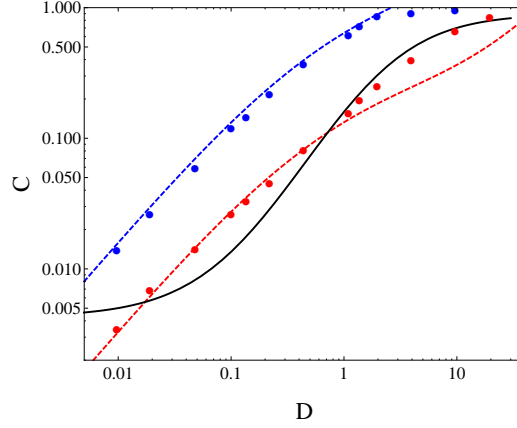


Figure 5.8: Energy conversion from hot electrons to protons. The color legend is the same as in Fig. 5.7 and the dashed lines show Eq. 5.7, while the full line Eq. 5.8.

For thicker layers the protons drag the electrons with them and at the proton front there will always be an electron cloud, which creates the accelerating field. Mostly the electrons with a kinetic energy higher than Φ_d contribute to the acceleration. By integrating the Maxwellian energy distribution of electrons from Φ_d until $\epsilon_{max} T_h$ and dividing by the total initial electron energy we obtain the energy conversion from the electrons to the protons as a function of D :

$$C_{thick} = \frac{2}{T_h} \int_{e\Phi_d}^{\epsilon_{max}} W_e f_e(W_e) dW_e \quad (5.8)$$

where $f_e(W_e) = (\sqrt{2\pi T_h W_e})^{-1} \exp(-W_e/T_h)$. This estimation is compared with the simulation results in Fig. 5.8. As we can see below $D = 1$ the dashed lines are in a pretty good agreement with the simulations. For $D \gg 1$ the full line is very close to the results from the simulation with long plasma. The reason of the full energy conversion for the short plasma is that the condition $d/L_p > a$ is fulfilled and for this layer detachment can not happen.

5.7 Relativistic momentum distribution function of electrons

In our 1D plasma expansion simulations we assumed non-relativistic electrons, because they have the Maxwell momentum distribution, which is implemented as default in VORPAL. For relativistic particles the Maxwell-Juettner distribution [49] is usually assumed, which corresponds to the equilibrium distribution of a relativistic gas. This distribution is achieved through collisions between molecules with relativistic speed [80]. In the laser plasma interaction the collisions are not important and the electrons are not in thermal equilibrium. Their energy spectrum can be fitted with a simple exponential function (see Fig. 4.4), which is different from the Maxwell-Juettner distribution.

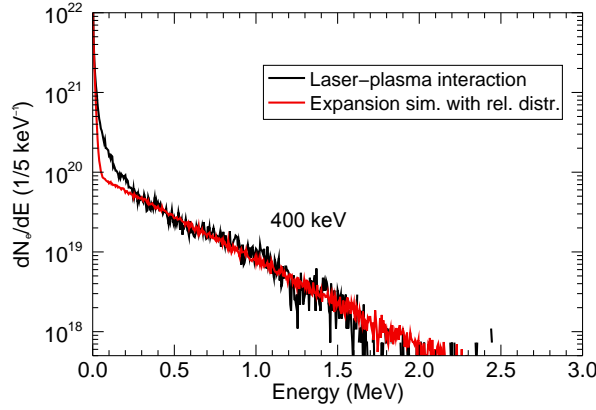


Figure 5.9: Energy spectrum of electrons from the laser-plasma simulation and plasma expansion simulation, where the analytical momentum distribution was used, Eq (5.10).

Based on the simulation results we can start from the energy distribution $f_h(W_e) = (N_h/T_h) \times \exp(-W_e/T_h)$, where N_h is the number of hot electrons, and using the relation

$$f_h(p) = \frac{1}{2} f(W_e) \frac{dW_e}{dp} \quad (5.9)$$

we can derive the momentum distribution function:

$$f_h(p) = \frac{AN_h}{2} \frac{|p|}{(m_e c)^2 \gamma(p) K_T} \exp\left(-\frac{\gamma(p) - 1}{K_T}\right) \quad (5.10)$$

where $\gamma(p) = (1 + (p/(m_e c))^2)^{1/2}$, $K_T = T_h/(m_e c^2)$ is the normalized temperature, $p = m_e \gamma v_e$ is the relativistic momentum and A is a normalization constant ($\lim_{K_T \rightarrow \infty} A = 0.5$). For the kinetic energy we took the relativistic expression: $W_e = m_e(\gamma - 1)c^2$. For the cold electrons we use the usual non-relativistic Maxwell-distribution:

$$f_c(v) = \frac{N_c}{\sqrt{2\pi} v_{th}} \exp\left(-\frac{v_e^2}{2v_{th}^2}\right) \quad (5.11)$$

where $v_{th}^2 = T_c/m_e$ is the thermal speed and N_c is the number of cold electrons. In VORPAL it is possible to implement any random number generator according to arbitrary chosen probability density function. Loading the electrons into the simulation with these momentum distributions we can reproduce the energy spectrum observed in the laser-plasma interaction. The comparison is shown in Fig. 5.9. The heating of the cold electrons is not included in the expansion simulation, that is the reason of discrepancy at low energy.

The simulations with relativistic electrons require more computational power, because λ_D/λ_{Dc} is large. In our 1D study the usual temperature-ratio is $T_h/T_c \approx 20$. With $n_{c0}/n_{h0} = 5$ the ratio of the scale lengths is $\lambda_D/\lambda_{Dc} = 10$, while in these simulations for $T_h/T_c = 320$ it would be 40. The equilibrium density profiles of the cold and hot electrons are the same as in the non-relativistic

case, therefore we can conclude that relativistic TNSA can be simulated with non-relativistic electrons, the result is the same in normalized units. The electric field and potential profile is studied in great details for arbitrary momentum distributions in [49], where the influence of the directed kinetic energy is found to be significant. In our simulations the electrons possess only thermal energy and in the laser-plasma simulations the directed energy is significant only during the first few recirculation period of the hot electrons.

5.8 Effect of the layer thickness in laser-plasma simulations

An advantage of plasma expansion simulations is that the hot electron density and temperature are well-known from the beginning and stay almost constant during the isothermal phase. This is not true in the laser-plasma interaction as we can see in Fig. 4.6. In this section we return to the TNSA with laser pulse, but instead of a proton plasma we use a heavy ion plasma with a proton layer, like in the previous sections. There is a significant increase in the hot electron temperature if the heavy ions are used, as we can see in Fig. 5.10. In this simulation the laser pulse was 100 fs long at 10^{19} W/cm² intensity. The higher electron energy is due to the lack of ion acceleration on the front side of the plasma. The RPA and plasma expansion processes observable in the interaction with proton plasma consume energy of the electrons, which results in lower temperature. The temperature achieved by using a heavy target is similar to the Wilk's prediction (Eq. (2.7)), which gives 961 keV.

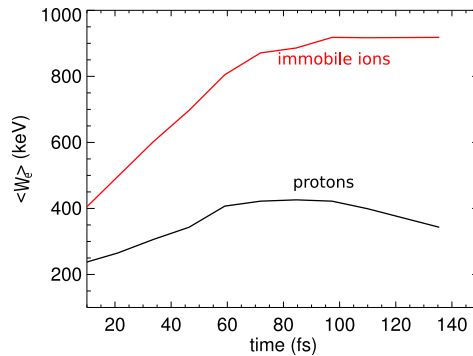


Figure 5.10: Time evolution of the mean kinetic energy of the hot electrons when a laser interacts with a proton plasma (black) and with an immobile ion plasma (red).

In these simulations the hot electron temperature is much higher than the initial one ($r \gg 1$), therefore the normalized layer thickness we can write as d/λ_{De} . In Fig. 5.11 we compare the results of simulations with two laser pulses. The energy conversion from electrons to protons and the final proton velocities are measured for different proton layer thicknesses. The peak laser intensity was the same in both cases ($I_L = 10^{19}$ W/cm²) with different pulse durations. In the case of the longer pulse the energy conversion is lower, as it is expected (L_p larger), but the final velocity is higher, especially in the plasma expansion regime. In the QSA regime the

maximum velocity depends on the length of the electron cloud, while in the thick layer regime obviously the time dependency of the front velocity plays a role.

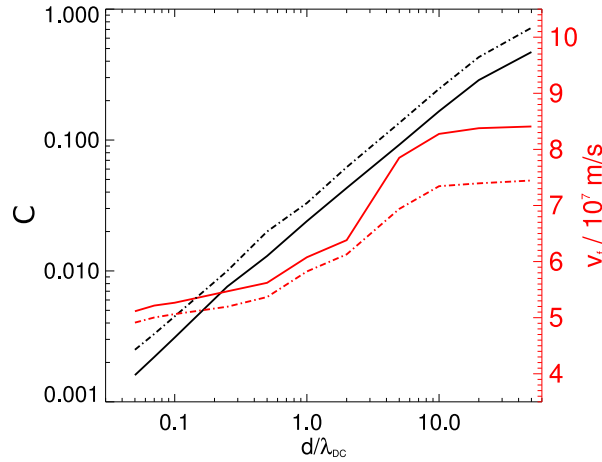


Figure 5.11: The black lines shows the energy conversion for 200 fs (dashed-dotted) and 400 fs (full) laser pulses. The red lines show the corresponding maximum proton velocity.

5.9 Conclusion and discussion of the 1D results

In the last 2 chapters we have presented electromagnetic (with laser pulse) and electrostatic 1D simulations. We started from the simplest case of the TNSA, when the target consists only of protons and electrons. The uncertainty of the hot electron parameters in the laser-plasma interaction requires the investigation of a simplified setup, where a two-temperature plasma is initialized with well-known hot and cold electron parameters. The non-trivial, but small effects of the cold electrons on the charge separation and plasma expansion can be studied and understood only in these circumstances. The next step was to implement the double layer structure of the target, which revealed the different acceleration regimes of the TNSA. These regimes can be identified by the value of a normalized layer thickness (Eq. 5.1), which depends on the hot-to-cold electron pressure ratio.

In the realistic TNSA only the initial cold electron Debye length and the layer thickness has to be known in order to identify the acceleration mechanism. In the interval $1 < d/\lambda_{De} < 10$ there is a jump in the maximum energy, but the energy conversion increases almost linearly, which indicates that the energy spectrum becomes broader with more ions in the low energy tail. The laser intensity determines the maximum energy, but in the thick layer regime the pulse duration is also important. It should be equal to the detachment time when the layer is thick, because after detachment the heavy ions are accelerated and the energy conversion from hot electrons to the protons will be low, see Fig. 5.8. In the thin layer regime it has to be at least as long as the time needed for the proton bunch to fly through the Debye-sheath, which is around $30/\omega_{pi}$, see Fig 5.2. These conditions are optimal for proton acceleration, with longer pulses the heavier ions from the target are also accelerated.

By including the transversal dimension the acceleration quantitatively changes. We expect lower energy conversion and weaker acceleration, because the hot electrons can disappear from the hot-spot. The new degree of freedom does not allow us to set up an initially equilibrium

plasma with a transversally non-uniform hot electron density distribution. In the next chapter in all of the simulations a laser pulse inevitably has to be used.

6 2D TNSA simulations

In the previous chapter we explored the different regimes of TNSA by changing the proton layer thickness. Here we do the same in 2D geometry, but a laser pulse is used to create the hot electron population. We need a source of hot electrons because of the transversal degree of freedom. If we set up a hot electron cloud somewhere in the plasma with well defined temperature and density, then it would spread out in each directions on a much shorter time-scale than the acceleration of ion.

The grid resolution can not be as high as in 1D, therefore the QSA regime can not be properly simulated, because of the extremely small scale length of the penetrating electric field. However, the main effects in the transversal acceleration can be observed. We performed a series of simulations to investigate the effect of the proton layer thickness on the transverse divergence.

6.1 Thickness-dependent divergence of the protons

In these simulations a 200 fs long laser pulse interacts with a $2 \mu\text{m}$ thick plasma slab with variable proton layer thickness on the rear surface. The laser intensity is $4 \cdot 10^{19} \text{ W/cm}^2$ with a Gaussian transversal intensity profile, $\sigma = 8 \mu\text{m}$. The initial electron temperature is 5 keV. The grid size is 3 times larger than the initial electron Debye-length and the particles are represented by 50 macroparticles per cell. In each simulation the setup is the same, only the layer thickness is changed. The layer can not be thinner than Δx , therefore in the QSA regime ($d < \lambda_{Dc}$) the layer density is reduced.

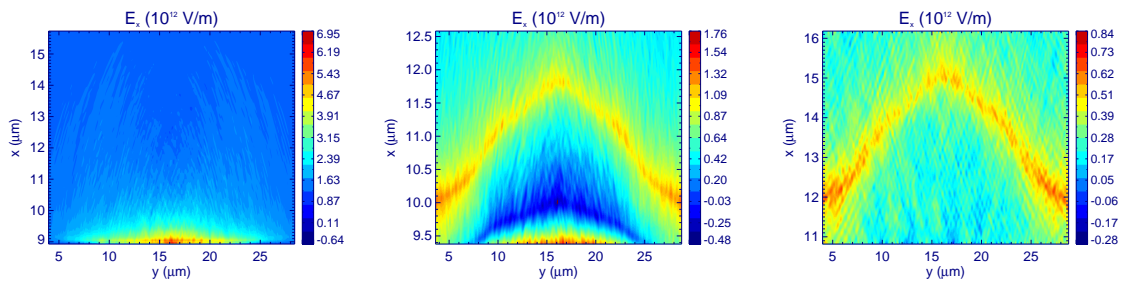


Figure 6.1: The longitudinal electric field behind the target for $D = 0.5$ (left), $D = 6$ (middle) and $D = 50$ (right). The rear surface is at $x = 9 \mu\text{m}$.

As we have seen in the last chapter, with high temperature ratios the skin layer of the TNSA field becomes equal to the cold electron Debye-length, $\lambda_D/r \approx \lambda_{Dc}$. In this chapter we always use the simplified definition of normalized layer thickness: $D = d/\lambda_{Dc}$, which is a good approximation.

First we show the contour plots of the longitudinal electric field in Fig. 6.1. There is nothing special in the 2D case, the time evolution in a dependence of layer thickness is the same as in 1D. It is worth to note the Gaussian transversal strength profile of the electric field, which is due to

the Gaussian hot electron density profile, as we will see later. Because of the non-uniform transversal density profile of the hot electrons, the Debye-sheath initially acts as an electrostatic lens, accelerating the protons towards the laser axis. The later stage of the transverse acceleration depends on the layer thickness.

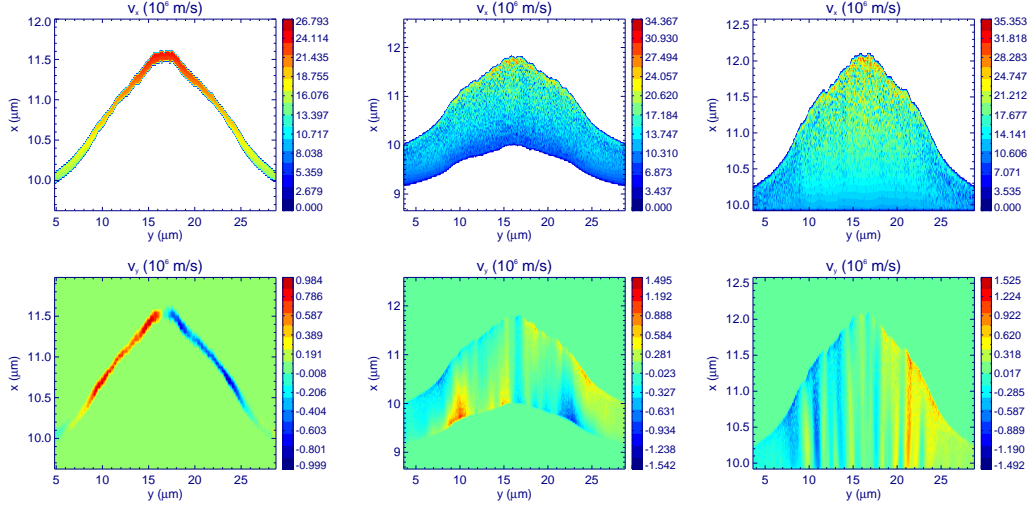


Figure 6.2: The longitudinal (upper row) and transversal (lower row) components of the proton velocity for $D = 0.5$ (left column), $D = 6$ (middle column) and $D = 50$ (right column). The rear surface is at $x = 9\mu\text{m}$.

For very thin layer the electric field is not influenced by the protons, which are accelerated as test particles. In the intermediate regime we can see the negative electric field at the tail of the proton bunch, like in Fig. 5.5, and for thick layers a peak electric field only at the proton front is visible, which is a characteristic feature of the plasma expansion. The resulting velocity distribution created by these electric fields is shown in Fig. 6.2. The transverse acceleration in the two extreme cases has opposite direction. We call it positive focusing in the QSA regime, because the protons are accelerated inwards, while in the expansion regime it is called negative focusing. In the intermediate regime the velocity contour shows a very complicated structure. The fields are always perpendicular to the surface and because in this regime there are two surfaces (bunch head and tail), and they are curved, the negative focusing in the front and positive focusing in the back act at the same time.

In order to characterize the divergence we measure the RMS velocity and the average velocity of the protons on the front surface at the end of the laser pulse. One may expect that there is a layer thickness for which the divergence is zero if it has different sign in the two extreme cases. The average velocity is calculated only in the half space, from the laser axis to the right. Our expectation is confirmed in Fig. 6.3, left plot, where the average velocity is zero for a given D value and the RMS velocity has a minimum (close to zero). Unfortunately this optimum thickness changes in time. The reason can be understood by looking at the right picture. Initially in the intermediate regime the acceleration is similar to the QSA, as we discussed already in the 1D case. In this phase the positive focusing is present. As the proton bunch flies further the acceleration transforms into the expansion regime, when the negative focusing overtakes the transverse acceleration. If the acceleration in the second phase is not too long, then the transverse velocity gained during the first phase is canceled by the charge separation field at the bunch surface. If the plasma expansion phase lasts longer, then the divergence increases again.

The positive focusing can be induced (or it can last longer) by changing the target surface shape, for instance by using a concave initial curvature of the target rear surface. In this case the thick proton layer can have small divergence even if the laser pulse is long.

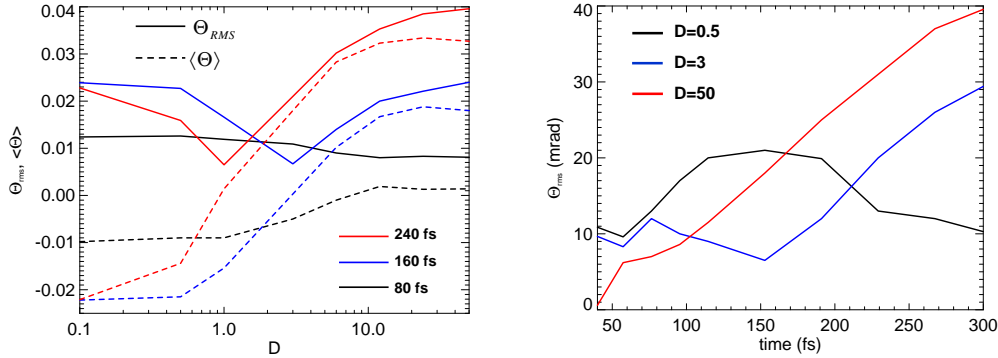


Figure 6.3: Left: The average and RMS angle (in radian) at the proton front at different times. Right: The time evolution of the RMS angle for different layer thicknesses.

In these simulations the plasma density was only 2 times higher than the critical density, because in this case the initial Debye-length is longer and the simulations could be performed in a shorter time. The drawback of this speed up is that the second and higher harmonics of the laser pulse can go through the target and disturb the transversal electric field. Because these harmonic waves have small amplitude, the effect on the longitudinal acceleration is negligible. The much weaker transverse fields are slightly modified, but by averaging the fields of the higher harmonics in time the overall effect is zero. In order to clearly see the transversal electric fields produced by the space-charge or charge separation, we have to increase the plasma density, which results in slower simulations.

6.2 QSA in 2D

In this section we illustrate the electric field configuration on the rear side of the target made of electrons and immobile ions. The proton layer is neglected because its small charge and the layer thickness can not be resolved anyway in our 2D simulation. The transversal dynamics is difficult to describe, because of the rapidly changing density gradient of the hot electrons. In a first approximation we can model the Debye-sheath as an electron cloud with Gaussian transversal density profile. The longitudinal profile is the same as in 1D. The hot electrons, due to space charge, expand with a very high speed, therefore the width of the Gaussian is increasing in time. In order to obtain the transverse proton velocity phase space we need to solve the Poisson equation in 2D, which can be done only numerically, and the time dependency of the density profile has to be included, which is not known.

Snapshot of the electric field is shown in Fig. 6.4. The transversal field, accelerating the protons towards the middle, is also responsible for the fast spread of the electrons over the target surface. In this simulation the plasma density is 8 times the critical density. The full length at half maximum of the laser intensity profile is $3 \mu\text{m}$. The target is placed at $7 \mu\text{m}$ from the laser source and its thickness is $3 \mu\text{m}$. The width of the simulation box is $48 \mu\text{m}$.

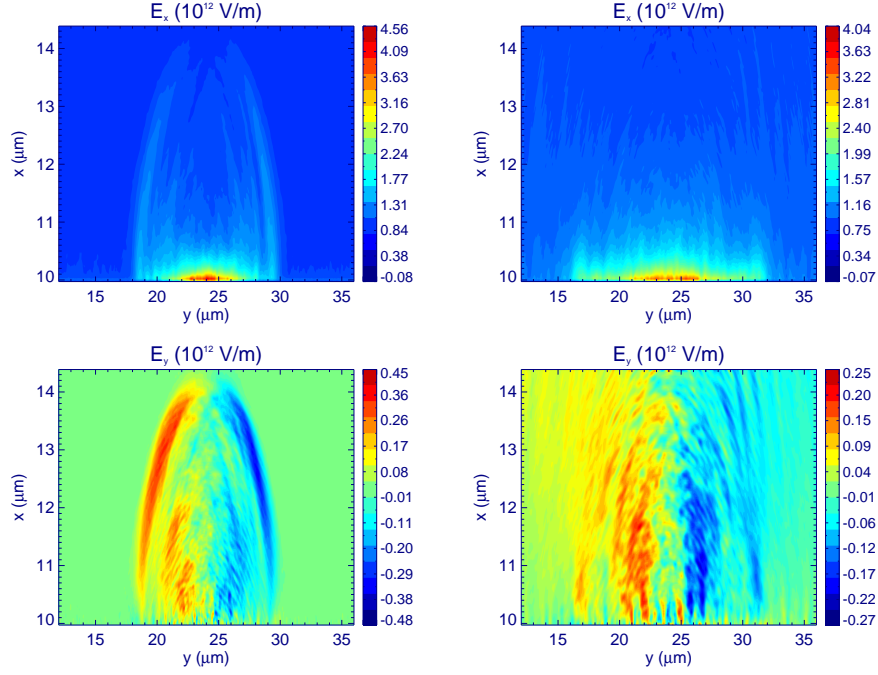


Figure 6.4: Simulation with immobile ions showing the electric fields: the longitudinal (upper row) and transversal (lower row) components at 45 fs (left) and at 76 fs (right). The rear surface is at $x = 10 \mu\text{m}$.

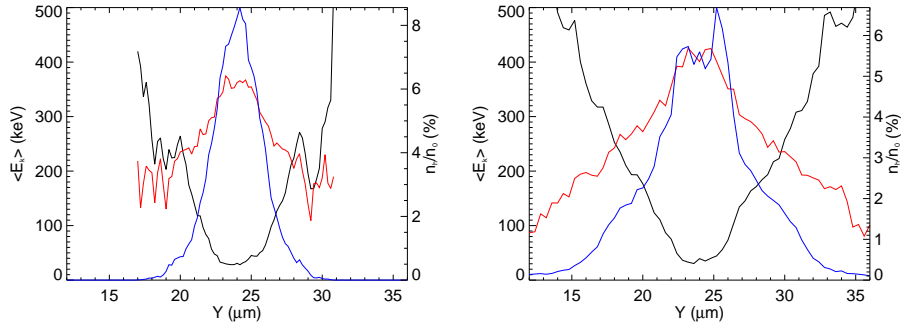


Figure 6.5: The longitudinal (red line), transversal (black line) temperature and density (blue line) of hot electrons. The plots are made for the same time instances as in Fig. 6.4.

We can take a look also at the electron temperature and density in a $1 \mu\text{m}$ thick layer at the rear side of the target plasma. Fig. 6.5 shows the mean kinetic energy and density of the electrons with energy higher than 100 keV. The edge of the electron cloud propagates with a velocity $\approx 2 \cdot 10^8 \text{ m/s}$. With this high speed the electron cloud can not be considered static and the analytical estimation of the transverse divergence is impossible. However, as the electrons spread out the transversal fields weaken and the transverse acceleration in comparison with the longitudinal one becomes negligible. That is why the transverse velocity in the QSA regime is much smaller than in the case of thick layers (see Fig. 6.2).

For the investigation of the acceleration of a thin layer in these fields, we have to resolve not only the layer thickness (should be smaller than the cold electron Debye-length), but also the exponential profile of the electric field close to the plasma surface ($x \leq 0$). These strong

requirements are beyond the capabilities of our computational resources. One alternative way to simulate the QSA regime in 2D is the implementation of an analytical charge distribution in VORPAL. Assuming a longitudinal density profile defined in Eqs. (2.15 and 2.17) and a Gaussian transversal profile we can write the charge distribution as:

$$\rho = \rho_{e0} \exp\left(-\frac{y^2}{2\sigma^2}\right) \left[\frac{2}{(\sqrt{2e_N} + x/\lambda_D(y))^2} \Big|_{x \geq 0} - 1 + \exp\left(-\exp\left(\frac{\alpha x}{\lambda_D(y)}\right)\right) \Big|_{x < 0} \right] \quad (6.1)$$

where $\alpha = 0.96$ (obeying charge neutrality), σ is the standard deviation of the transverse laser intensity profile, $\rho_{e0} = q_e n_{h0}$ is the hot electron charge density at the plasma surface ($x = 0$) and $\lambda_D(y) = \lambda_D \exp(y^2/(4\sigma^2))$ is the hot electron Debye-length, which depends on the transverse position. We assume a 1T plasma because the skin depth of the electric field is larger. Although in the TNSA a 2T plasma is present the final maximum energy is the same for a 1T plasma as well, it depends only on the maximum electron energy (or length of the Debye-sheath). Using a Poisson solver the electric field is obtained from the static charge distribution and only the hot electron Debye-length has to be resolved. In the laser-plasma interaction for a correct QSA simulation the cold electron Debye-length has to be resolved, which is not feasible. In this simulation the grid size is 8 times smaller than $\lambda_D = 0.16 \mu\text{m}$ and the proton positions were generated separately in an IDL script. Thus we could set up a much thinner layer than the grid size, $d = 5 \text{ nm}$ ($D = 0.03$).

The resulting potential and velocity phase-space of protons is shown in Fig. 6.6. The proton acceleration can be imagined as they slide down on this potential-well, initially sitting at $e\Phi/T_h = -1$, at the position $x = 0$. In this simulation $\sigma = 2 \mu\text{m}$, which is much smaller than in the reality and the transversal velocity is 6 times smaller than the longitudinal which corresponds to 9.5 degree maximum divergence. The divergence of a thin proton is typically smaller than in the expansion regime because of the short traveling time of the protons in the Debye-sheath. Beside this, due to the broadening electron cloud, the transversal fields become weaker as the protons reach the end of the electron sheath.

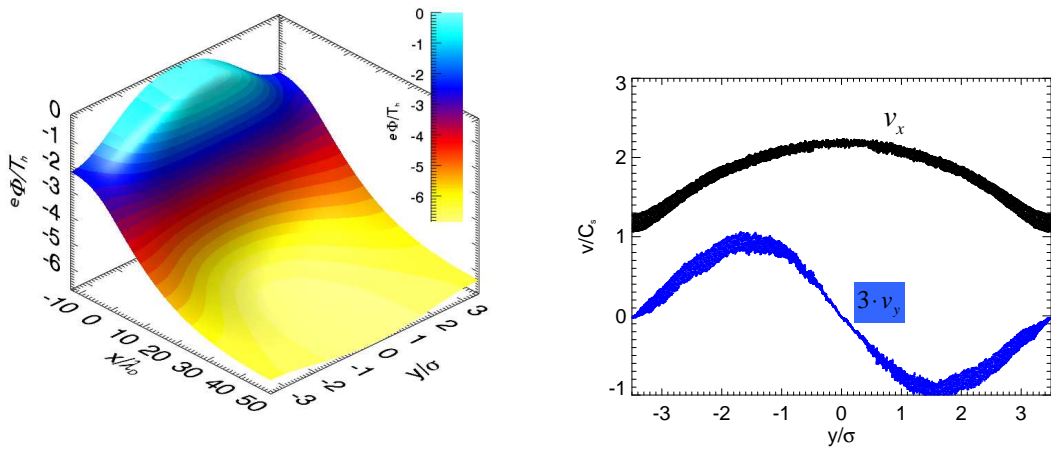


Figure 6.6: Left: The potential in a 3D contour plot produced by the charge distribution given in Eq. (6.1). Right: The longitudinal (black) and transversal (blue) velocity components of the protons at $\omega_{pi}t = 18$.

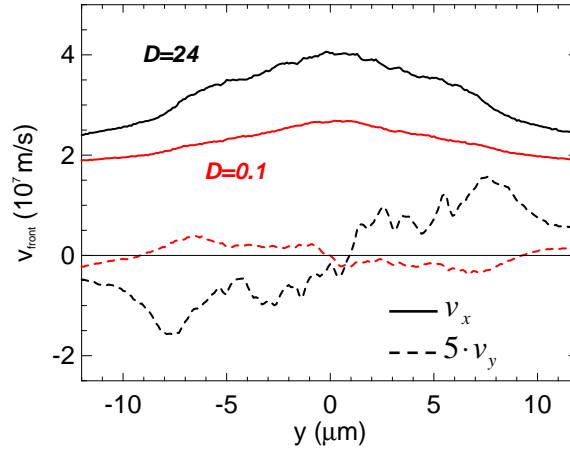


Figure 6.7: Comparison of the longitudinal and transversal velocity components of the protons at the outer surface of the expanding plasma at the end of the laser pulse duration.

In Fig. 6.7 the comparison of the two extreme cases is shown. It confirms that in the QSA regime the transverse acceleration is much weaker than in the plasma expansion regime. Here the black line represents the average velocity of the protons in a $0.2 \mu\text{m}$ thin layer at the proton front. The red line is calculated for all of the protons because the local energy spread at each y position is very small. Many experimental results and theoretical works [4, 12, 13, 14] imply that the layer should be thicker than penetration depth of the electric field.

6.3 2D plasma expansion, envelope model

If we want to handle and further transport the proton beam we have to know its space properties, especially the divergence angle. In the experiments the typical observation is ≈ 20 degrees maximum envelope angle [21, 23]. Our scope is to give an analytical model, which explains this feature and to support it with 2D PIC simulations. With the model presented here we try to describe the mechanism of the transversal acceleration and the divergence observed in experiments. The analytical results are validated by 2D TNSA simulations. With our 32 nodes available for VORPAL we are restricted to a quite small spacial domain: max. $\approx 100 \times 100 \mu\text{m}^2$, but it is large enough compared to the hot electron Debye-length ($\approx 0.2, \mu\text{m}$) or to the laser spot ($\approx 10 \mu\text{m}$).

Just like in our 1D studies, the target consists of a thick ($2 \mu\text{m}$) heavy ion slab and a much thinner proton layer ($0.5 \mu\text{m}$) with cold neutralizing electrons. The laser pulse has a Gaussian transversal intensity profile. We are focusing on the expansion of a proton layer which is thicker than the penetration depth of the electric field into the target (few nm). Because of the exponential density profile of an expanding plasma we are restricted to a short time window (several hundred fs), in which the proton front can be resolved by the macroparticles. This time is enough, because the fields are strong only at the beginning of the expansion, later on the front velocity does not change significantly, even if the laser pulse is long.

In the following we present the basic idea behind the 2D expansion model, then we compare the analytical predictions with our simulation results and discuss the discrepancies.

6.3.1 The Model

Our 2D simulations show that the self-similar electric field ($E_0 = \sqrt{n_{h0}T_h/\epsilon_0}$), which defines the acceleration, can be fitted with the function

$$f(y) = \exp(-y^2/(4\sigma^2)) \quad (6.2)$$

which indicates that the product of the hot electron density and temperature (pressure) results in a Gaussian transversal profile. This is confirmed in Fig. 6.8, where E_0 is plotted at three time instances and compared with the analytical fit. The simulation parameters are presented in Table 6.1, Sim3 column. As we can see the width of the hot spot increases, but in the relevant time interval it agrees well with the simulation (blue line). For the analytical calculations we have to use the hot electron pressure in the early stage of the plasma expansion, because this is when the acceleration is the most active and the proton surface is defined. In the model for the transverse hot electron density distribution we use a Gaussian, which has an RMS transverse size (σ) comparable to the half width of the laser pulse and the temperature is considered to be uniform in space and constant in time. Although the intensity profile of the laser is also Gaussian the hot electron temperature becomes isotropic faster than the density. This hot electron configuration also provides the same electric field shown in Fig. 6.8. The peak value of the density (n_{h0}) is measured at the laser axis. For this we rely on the simulation and do not use other semi-empirical estimations.

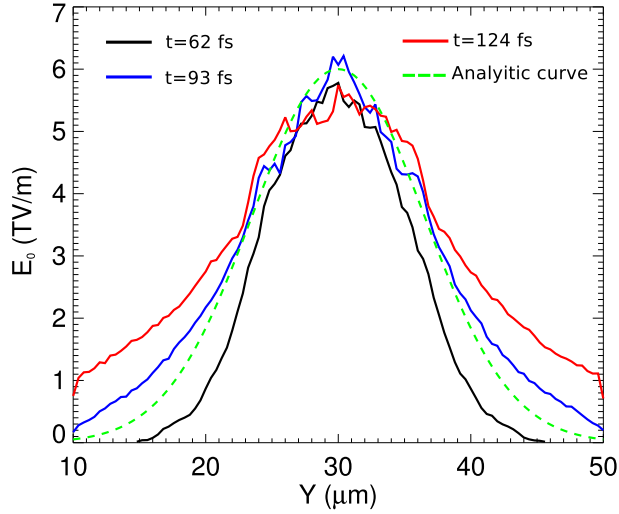


Figure 6.8: The self-similar electric field (E_0) calculated from the measured hot electron parameters during the acceleration. The green dashed line shows the analytical fit Eq. (6.2), with $\sigma = 4.6\mu\text{m}$.

After laying down the initial conditions and assumptions we can derive a transversal acceleration by using the 1D isothermal model. The model is based on the fact that electric field vector is always perpendicular to the proton surface, which is determined by the proton front. The transverse component (E_y) is proportional to the tangent of the surface angle. An example for the electric field configuration around the expanding plasma is shown in Fig. 6.9. As a simplification we calculate E_y by multiplying E_x with the surface angle, because it is small ($\Theta < 0.2$ rad) in our time frame of interest ($\omega_{pi}t < 20$) if σ/λ_D is large. All we need to know is the

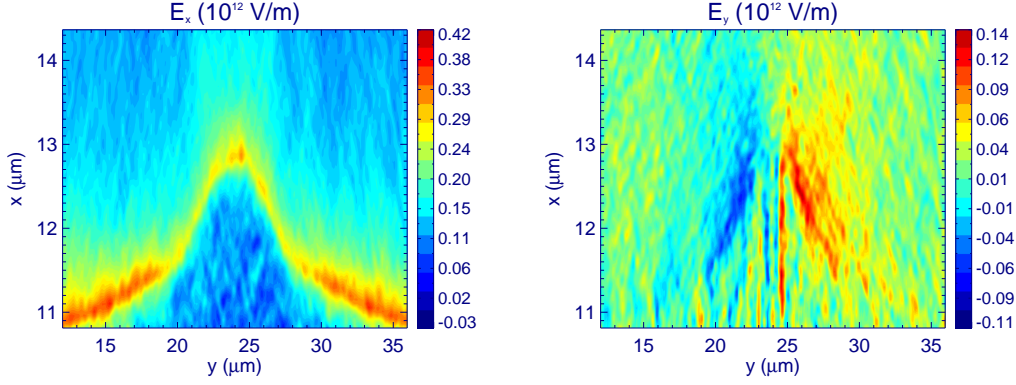


Figure 6.9: The longitudinal (left) and transversal (right) electric field in a 2D TNSA simulation with a thick layer, $D = 50$.

time-dependent derivative of the proton front as a function of y . The starting equation gives the position of the ion front [9]:

$$\chi_f(v, \tau) = 2\tau(\ln(\eta(v)\tau + \sqrt{(\eta(v)\tau)^2 + 2}) - \ln(\sqrt{2})) - 2(\sqrt{(\eta(v)\tau)^2 + 2} - \sqrt{2})/\eta(v) \quad (6.3)$$

where $\eta = \sqrt{n_h(v)/n_{h0}}$ and $n_h(v) = n_{h0} \exp(-v^2/2)$. Here the transverse coordinate is normalized to σ , $v = y/\sigma$, the time t is normalized to $1/\omega_{pi}$ and the longitudinal coordinate x is measured in the units of λ_D . This curve can be fitted with a parabolic function, $f(y) = x_f(0, t) - C_t y^2$, where C_t is a time-dependent fitting parameter, with high accuracy in the interval $[-2\sigma, 2\sigma]$. This function for the proton surface was also suggested in [81]. We have to mention that the Euler number (e_N) is missing from the expression, because the 1D model [9] is derived for one-temperature electrons, but in the two-temperature case φ_0 appears in the exponent. It depends on the hot-to-cold electron pressure ratio and on y , which would make the equations more complicated. Assuming that the cold electron density is much higher than that of the hot electrons, we can use the approximation $\varphi_0 \approx 0$. If we calculate the derivative of Eq. (6.3), we get the following expression:

$$\frac{\partial \chi_f}{\partial v} = \frac{v\tau}{\Sigma} \left(\sqrt{1 + \frac{1}{k(v, \tau)}} - \sqrt{\frac{1}{k(v, \tau)}} \right) \quad (6.4)$$

$$k(v, \tau) = \exp(-v^2/2)\tau^2/2 \quad (6.5)$$

where $\Sigma = \sigma/\lambda_D$. Now we use $E_y(v, \tau) = (\partial \chi_f / \partial v) E_x(v, \tau)$, where

$$E_x(v, \tau) = \frac{2\eta(v)}{\sqrt{2 + \eta(v)^2\tau^2}} \quad (6.6)$$

The transverse velocity (v_y) of the protons at the front can be calculated if we integrate Eq. (6.6) over time, which results in

$$v_y(v, \tau)/C_s = \frac{v\tau}{\Sigma} \left(2 - \sqrt{\frac{1}{k(v, \tau)} \frac{v_x}{C_s}} \right) \quad (6.7)$$

where $v_x = 2C_s \ln(\eta(v)\tau/\sqrt{2} + \sqrt{1 + (\eta(v)\tau)^2/2})$ is the longitudinal velocity. The opening angle of the protons at the surface we obtain by dividing Eq. (6.7) with v_x which gives:

$$\Theta(v, \tau) = \frac{v\tau}{\Sigma} \left(\frac{2C_s}{v_x} - \sqrt{\frac{1}{k(v, \tau)}} \right) \quad (6.8)$$

This angle is approximately 3.4 times smaller than the surface angle given in Eq. (6.4). This expression gives us the divergence of the protons at the surface and we will see that it can be used to describe the velocity phase-space of the whole expanding proton plasma.

6.3.2 Comparison with simulations

In this section we are going to validate the model presented above by 2D PIC simulations using laser pulse. Three different simulations were carried out where the hot electron parameters were measured at the middle of the laser pulse and used for the normalizations. In Table 6.1 the simulation parameters and the measured hot electron parameters are listed for the three cases. The initial cold electron density was always the same, $n_0 = 8.8 \cdot 10^{27} \text{ m}^{-3}$, which corresponds to $4n_{cr}$.

In the following we present the results and compare with the analytical model for different time steps. The expansion at the rear side of the target starts at 30 fs. In Fig. 6.10, 6.11, 6.12 the analytical curves are shown by the red lines, while the simulation results are presented by the black lines. At early time the longitudinal velocity is smaller than the predicted one, because we use the hot electron density and temperature measured at a later time. As we can see the discrepancy is large for small Σ , because the proton surface strongly deviates from the Gaussian because of an unrealistic 2D effect.

| Physical quantity | Sim1 | Sim2 | Sim3 |
|------------------------------------|-------------------------------------|-------------------------------------|-------------------------------------|
| Pulse duration | 300 fs | 500 fs | 300fs |
| Laser intensity | $4 \cdot 10^{23} \text{ W/m}^2$ | $0.8 \cdot 10^{23} \text{ W/m}^2$ | $4 \cdot 10^{23} \text{ W/m}^2$ |
| σ_L | $1.7 \mu\text{m}$ | $8.51 \mu\text{m}$ | $3.4 \mu\text{m}$ |
| σ | $2.5 \mu\text{m}$ | $8 \mu\text{m}$ | $4.6 \mu\text{m}$ |
| Debye length (λ_D) | $7.28 \cdot 10^{-8} \text{ m}$ | $6.51 \cdot 10^{-8} \text{ m}$ | $7.6 \cdot 10^{-8} \text{ m}$ |
| Plasma frequency (ω_{pi}) | $8.28 \cdot 10^{13} \text{ s}^{-1}$ | $8.09 \cdot 10^{13} \text{ s}^{-1}$ | $8.73 \cdot 10^{13} \text{ s}^{-1}$ |
| Hot electron temperature | 380 keV | 290 keV | 460 keV |
| n_{h0}/n_0 | 0.45 | 0.43 | 0.50 |

Table 6.1: Parameters of 2D simulations and calculations

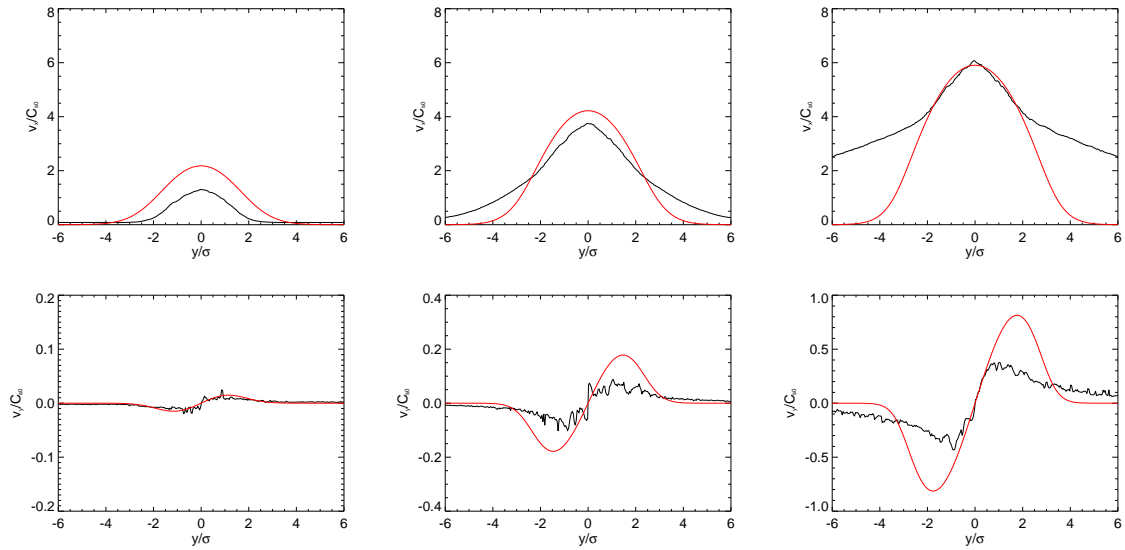


Figure 6.10: Longitudinal and transversal velocities for Sim1 at the time moments: 50, 100, 200 fs.

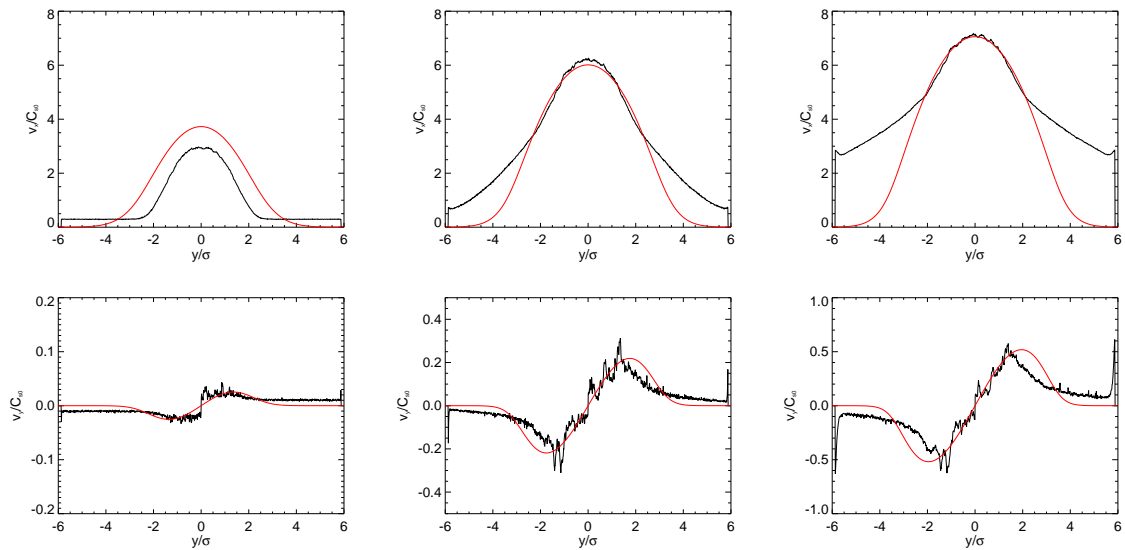


Figure 6.11: Longitudinal and transversal velocities for Sim2 at the time moments: 80, 200, 320 fs.

A very important feature is that the hot electron density is not realistic in transverse direction. The physical problem has a cylindrical symmetry which means that the electrons propagate in each direction, not only along the y coordinate. It means that n_h should decrease as $1/r$, where r is the distance (radius) from the middle (axis of symmetry of the laser pulse). This effect can not be seen in our simulations that's why the protons are accelerated not only in the hot spot, but farther away from this region. A real validation of the model needs a 3D simulation. However, the good agreement close to the center indicates that we can assume the Gaussian density profile to be a good approximation and the model is applicable in the real life.

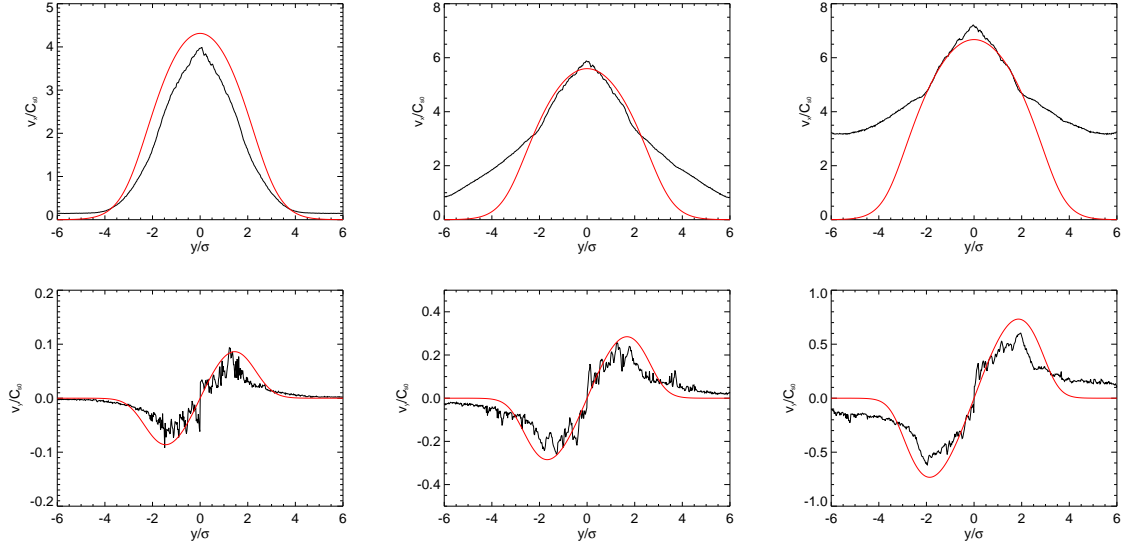


Figure 6.12: Longitudinal and transversal velocities for Sim3 at the time moments: 90, 150, 240 fs.

The next step is to map the entire velocity phase space of the proton bunch using the model. For this we have to know what happens to the protons which are behind the front surface. In Fig. 6.13, left the proton density is shown, and in the right the velocity angle along a line at the position $x = 16 \mu\text{m}$ at different time moments. As we can see the protons follow the front surface, each proton at a given position has the same angle (Θ) as the proton front had at the time when it was at the position of the selected proton. This is illustrated by the green point, which at $t = 250$ fs was at the proton front, but when it is inside the expanding plasma the divergence is the same as it was of at the proton front earlier.

This is a very useful feature of the expanding plasma, because from the time evolution of the proton front we can reconstruct the whole velocity phase-space. This is confirmed by a comparison shown in Fig. 6.14 where v_x versus v_y normalized to the acoustic speed is plotted. The analytical plots were produced by drawing the velocities at the surface at each time moment. If we want to know the velocity angle in one point inside of the gray area we have to track back Eq. (6.8) until the outer boundary is crossing that point.

6.3.3 Beam properties

Our ultimate scope is to have an expression for the envelope angle as a function of proton energy and time. For this we have to relate the longitudinal velocity of the protons to the transverse position. This we can do if we use an approximation for $\tau \gg 1$:

$$v_x/C_s = \ln(2\eta(v)^2\tau^2) \quad (6.9)$$

The normalized velocity can be written as $v_x/C_s = \sqrt{2W/T_h}$. From this equation we can express the v coordinate as a function of energy and time:

$$v(W, \tau) = \sqrt{2} \left(\ln(2\tau^2) - \sqrt{2W/T_h} \right)^{1/2} \quad (6.10)$$

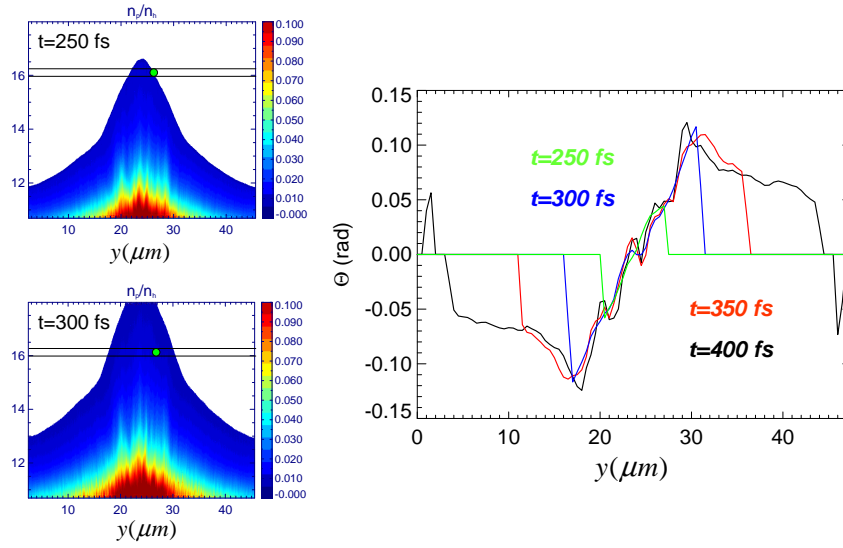


Figure 6.13: Left: Contour plot of the expanding proton plasma at two time instances. Right: The angle of the proton velocity vector with respect to the x direction along the line $x = 16\mu\text{m}$, indicated in the left by the horizontal lines.

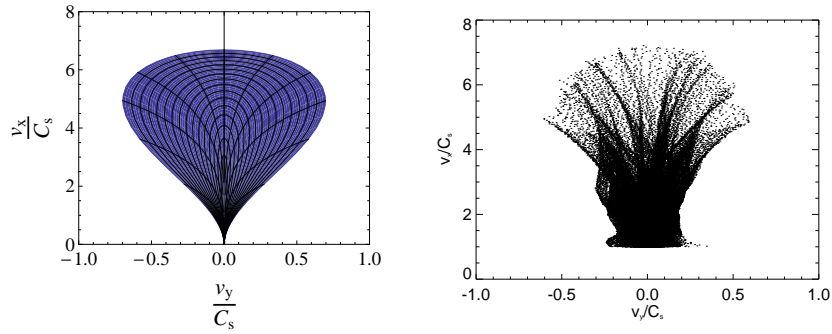


Figure 6.14: Velocity phase-space of protons from Sim3 at $\omega_{pi}t = 19.2$. In the left plot the analytical prediction Eqs. (6.7,6.9) is shown and in the right one is the simulation result.

If we plug this expression into Eq. 6.8 we have the envelope angle in time as a function of energy. For the cut-off energy we use the prediction from [9]: $W_{max} = 2T_h(\ln(\sqrt{2}\tau))^2$. In Fig. 6.15 a comparison is presented between the model and simulations. As we can see for larger Σ the agreement is better. Due to the filamentations occurred in the laser-plasma interaction in the simulation we don't have such a smooth curve as in the model and due to the above discussed 2D effect we can expect good agreement only close to the top of the surface where the high energy protons are.

As we know, the isothermal model gives a simple expression for the velocity as a function of time and space: $v = C_s + x/t$. This does not depend on the hot electron density and the interesting consequence of it is that along a line parallel to the target surface, the longitudinal velocity is the same. It makes very easy to calculate the velocity components of a proton once we know its position.

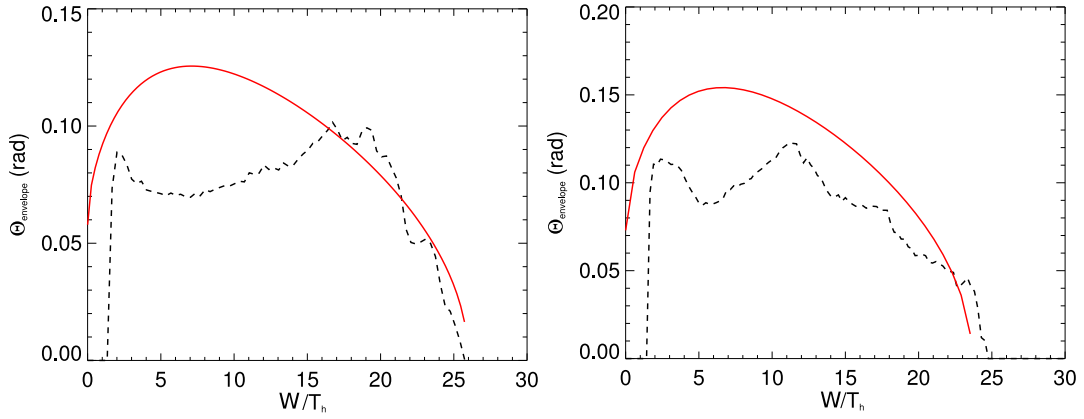


Figure 6.15: Left: The envelope angle of protons as a function of energy at $\omega_{pi}t = 20$ for Sim2. Right: The envelope angle of protons as a function of energy at $\omega_{pi}t = 24$ for Sim3. The dashed black line is simulation result and the full red line is the model.

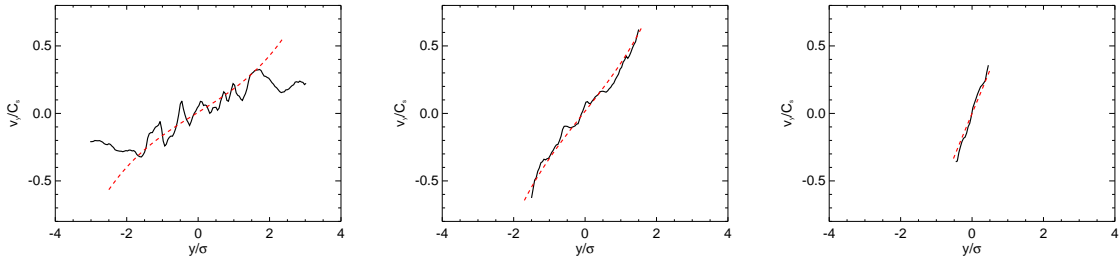


Figure 6.16: The transverse velocity along the lines : $x/\lambda_D = 50, 80, 107$ from Sim3. The time moment is $\omega_{pi}t = 22$. The red dashed line is obtained from the model and the black dots from the simulation.

We can use the model to predict and analyze the transverse phase-space of the beam, which also depends on the longitudinal energy. The $[y, y']$ phase space along one line can be obtained numerically if we calculate the time from Eq. 6.3 when the proton front reaches a given x position for each y coordinate. Then we insert this time in Eq. 6.8, which we multiply with $1 + x/t$ to obtain the normalized two-dimensional array: $[y, y']$. This numerical solution is plotted and compared to Sim2 in Fig. 6.16. As we can see the agreement is quite good. One can observe that the transverse phase-space of the protons is rotating to the vertical position as the energy increases. The opening angle as a function of energy and transverse position can be represented with contour plots, as it is shown in Fig. 6.17.

This feature of the proton beam has been observed in other simulations [82] and experiments [21] as well. This is very important and has to be taken into account in the further simulations, where the beam is collimated or transported to other devices. The most energetic protons reach first the magnetic focusing element, which are close to the center and experience the less focusing because of their small divergence. As the beam penetrates the magnetic field the slower protons close to the axis will have an even smaller opening angle, but towards the outer surface their divergence increases up to the maximum value.

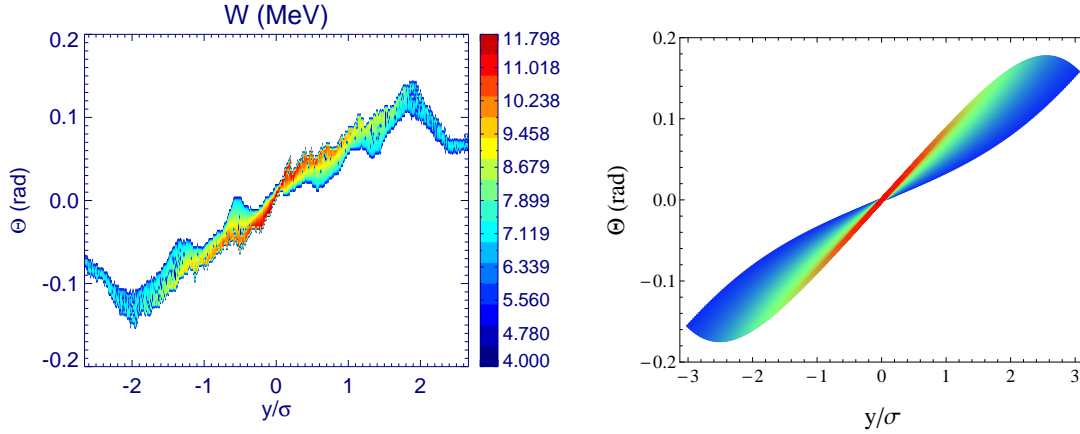


Figure 6.17: The energy dependent opening angle is shown versus the transverse position obtained from Sim3 (left) from the model (right) at the time instance $\tau = 22$. The color code is the same for both plots.

6.3.4 Simulation with a Gaussian laser pulse

We repeated the simulation Sim3 with a Gaussian pulse and we found a negligible difference in the results. The pulses are defined like in Fig. 4.7 and their spatial intensity contour is shown in Fig. 6.18. The duration of the Gaussian pulse is reduced to 247 fs in order to keep the total energy the same. The plasma interacts with a lower intensity initially, but later the temperature and density of hot electrons will be higher, as it is shown in Fig. 6.19. The time development of the hot electron population is very similar to the 1D case, but in 2D their longitudinal temperature does not increase as much, in the simulation with the shifted pulse it stays constant at the beginning. Probably for shorter pulses one can observe more significant effects of the pulse shapes, because of the quickly changing intensity amplitudes.

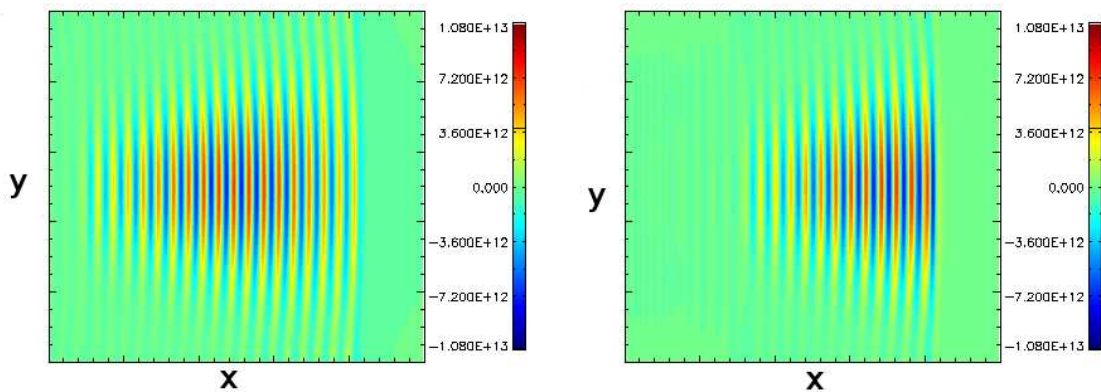


Figure 6.18: Comparison of the normal (left) and shifted Gaussian (right) pulses in 2D.

The hot electron energy now is shared between the longitudinal and transversal plane, but the longitudinal temperature is higher. The hot electrons spread with high velocity in the transverse direction, and their density remains almost constant, while the total number increases.

The divergence of the protons for the two pulses is also very similar, as it is shown in Fig. 6.20. At the beginning the acceleration is weaker with the Gaussian pulse, but later it overtakes the

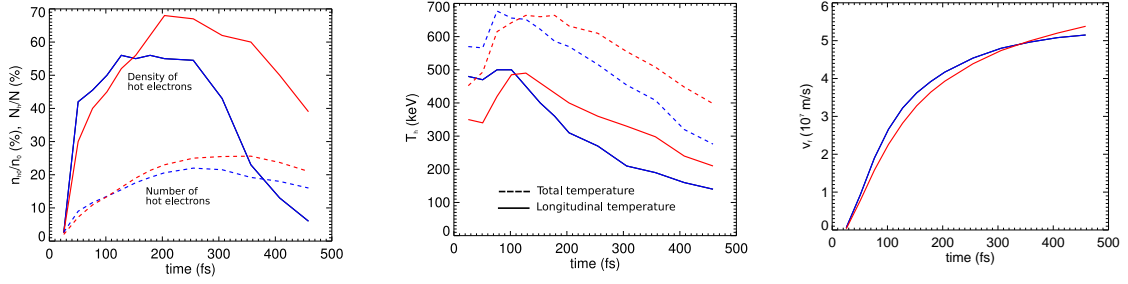


Figure 6.19: The time development of the hot electrons for the Gaussian (red) and shifted Gaussian pulses (blue): density and total number (left), Longitudinal and total temperature (middle), and proton front velocity (right).

acceleration induced by the shifted pulse. The higher velocity in the later stage of the expansion indicates a faster development of the surface angle, which results in a slightly larger divergence which we observe in the third picture.

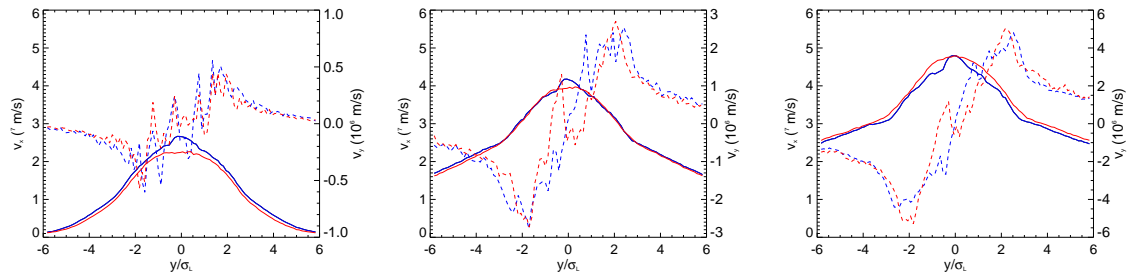


Figure 6.20: Longitudinal (full line) and transversal (dashed line) velocities of the protons at the front for : 100 fs (left), 200 fs (middle), and 300 fs (right). The color legend is the same as in Fig. 6.19

6.4 Energy conversion in 2D

Using the simulations presented in section 6.1 we can calculate the energy conversion from the hot electrons to the protons. The absorbed energy from the laser was about 35 %. The result in a dependence of layer thickness is shown in Fig. 6.21, left.

The obvious consequence of the new transversal dimension is the lower energy conversion compared to the 1D case. The dependence on the layer thickness is about the same as in 1D and it is clear that in the expansion regime most of the energy goes to the low energy protons, when we compare the red and blue lines in Fig. 6.21. In the QSA regime almost all of the protons have higher energy than half of the maximum energy, which is shown in Fig. 6.21, right. If we compare this plot with the 1D case in Fig. 5.11 we observe that the energy conversion in 2D is 3-4 times smaller. The hot electrons lose about 50 % of their energy at the lateral boundaries.

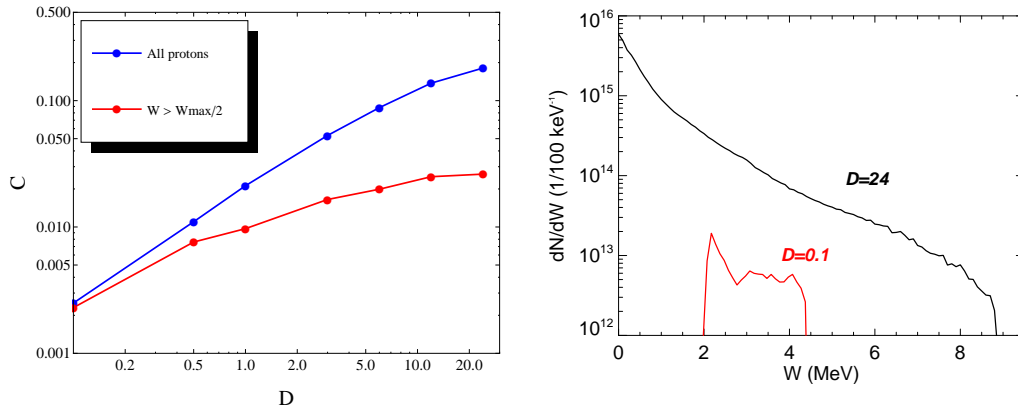


Figure 6.21: Left: The energy conversion from electrons to protons. In the case of the blue line we take into account all of the protons, but the red line shows the conversion for the protons with energy higher than half of the cut-off energy. Right: Comparison of the energy spectrum of the protons in the extreme cases.

6.5 3D velocity phase space of protons

As we discussed earlier the 2D simulation with Cartesian grid does not give the correct electron density in the transverse distribution. In reality the density profile would be much more similar to a Gaussian function, everywhere, not only close to the center. If we assume that the whole expansion is rotation symmetric we can easily extend the model to 3 dimensions in cylindrical coordinates. The evolution of the proton front will be the same at each angle and y has to be replaced with r (radius). It means that in every equation of the previous section instead of y^2 we can write $y^2 + z^2$. The velocity components in 3D will have the following form:

$$v_x = C_s(1 + x/t); v_y = \frac{|y|}{y} v_x \Theta \cos(\arctan(\frac{z}{y})); v_z = \frac{|z|}{z} v_x \Theta |\sin(\arctan(\frac{z}{y}))| \quad (6.11)$$

The proton surface is defined by Eq. 6.3. The visualization of the proton bunch is done in Fig. 6.22, where the main parameters are: $C_s = 0.5 \cdot 10^7$ m/s, $\lambda_D = 1.2 \cdot 10^{-7}$ m, $\omega_{pi}t = 15$ and $\sigma = 6 \mu\text{m}$. These four parameters are necessary to set up the initial proton bunch analytically. The diameter of the bunch is 4σ ($24 \mu\text{m}$) and the protons with v_x higher than $2C_s$ are included. Basically we virtually cut out the top of the expanding proton plasma from a TNSA, where the hot electron parameters would be: $n_{h0} = 1.027 \text{ m}^{-3}$ and $T_h = 260$ keV. Now we can load it into a simulation box with the neutralizing and co-moving hot electrons. We performed a simulation with $T_{h0} = 90$ keV and let it run until 2 ps. Such a plasmoid can be easily resolved even in 3D, because only hot electrons are present and their Debye-length is large. The grid size in each direction is $0.5 \mu\text{m}$ and the length of the simulation box is $40 \mu\text{m}$.

The results are shown in Fig. 6.23. As we can see the transversal velocity has increased significantly, which results in a 18 degrees maximum opening angle. It is in good agreement with the experimental findings at the PHELIX, where the source size is larger, but the pulse duration is also longer than $15/\omega_{pi}$ (360 fs in our case). The divergence angle is proportional to the acceleration time, but it is inversely proportional to the Σ , therefore in experiments it is better to use a large laser spot and long pulse duration for higher cut-off energy and smaller divergence.

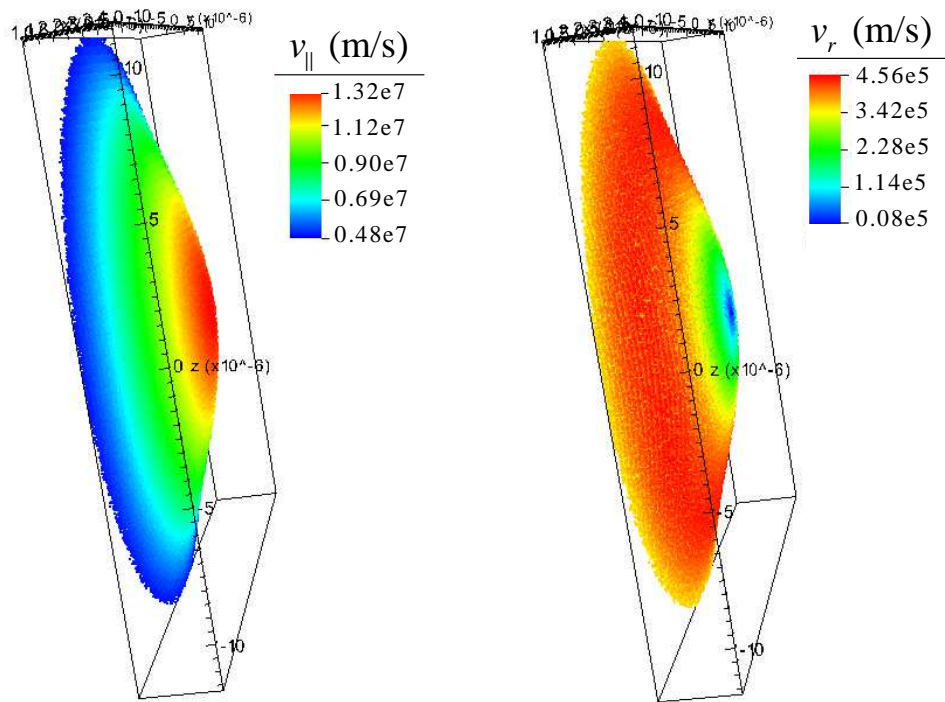


Figure 6.22: The initial longitudinal (left) and radial (right) velocity distribution of protons on the surface.

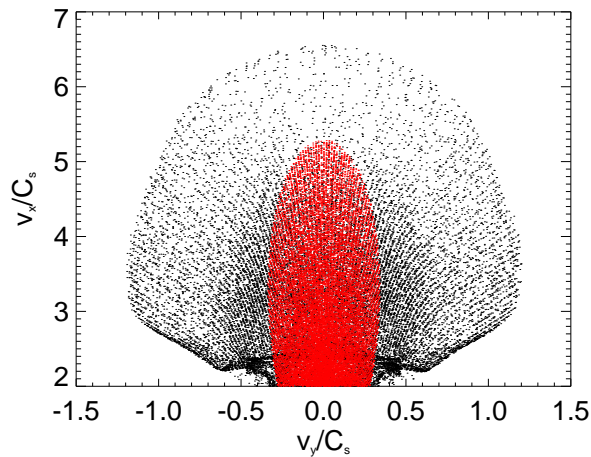


Figure 6.23: Velocity phase space of protons at the beginning (red) and 2 ps later (black).

This simulation technique allows us to study the behavior of a proton bunch in any magnetic field (solenoid, quadrupole), which are used in the experiments. With the proposed analytical model we can simulate the focusing and transport of the beam with realistic density and phase-space distributions. Thus we have the connection between the first and second stages of the LIGHT project.

6.6 Comparison with experiments

The proton surface for low energies is not known exactly, but we can study in the divergence angle in the high energy portion of the proton beam. From Eq. 6.10 we can conclude that the energy is proportional to the fourth power of the transverse position. In this case we can simplify our expression for Θ by taking $k(\tau) \approx \tau^2/2$, which means that the high energy protons are very close to the center ($\nu \ll 1$). Thus in this limit and for $\tau \gg 1$ the expression has the form:

$$\Theta_0(W, \tau) = \frac{v(W, \tau)}{\Sigma} \left(\frac{\tau}{\ln(\sqrt{2}\tau)} - \sqrt{2} \right), \quad (6.12)$$

where $v(W, t)$ is given by Eq. 6.10. The unknown parameters are the hot electron temperature (T_h) and density (n_{n0}), the acceleration time and the σ . For T_h we can use the newest scaling law [65]:

$$T_h = \frac{\pi m_e c^2}{2K_{ell}(-a_L^2)} \quad (6.13)$$

where K_{ell} is the complete elliptic integral of the first kind. The acceleration time we choose to be 1.3 times the pulse duration. The other two parameters are independent, because the hot electron density determines the maximum energy and the σ is responsible for the divergence. In this scenario we remain with two fitting parameters, which can be also estimated by other means and compared to the result of the fitting of Eq. 6.12 to the experimental measurements.

The σ of electrons we can relate to the full width at half maximum (FWHM) of the laser spot-size, which is known, if we introduce an other parameter, the spread-angle of hot electrons (Θ_{el}), which is the half opening angle of the hot electrons inside the target. This opening angle is unknown, but in the experiments it is assumed to be around 10 degrees. The σ as a function of this angle can be easily expressed as:

$$\sigma = \frac{S_{FWHM}}{2\sqrt{2\ln(2)}} + L_t \tan(\Theta_{el}) \quad (6.14)$$

The experimental data is taken from the PhD thesis of Frank Nuernberg [19] and Marius Schollmeier [83] together with the used laser and target parameters presented in table 6.2. The experiments were done at three different facilities and the energy spectrum together with the divergence angle were measured by the same RIS technique.

The measured data and the fitted curves using Eq. 6.12 are presented in Fig. 6.24. As we expected, in the low energy part there is no agreement at all, but a perfect fit can be seen in the high energy part. The parameters given in table 6.2 are also close to the realistic estimations [14],[84]. As we can see in Fig. 6.23 a significant part of the transverse acceleration can happen after the isothermal phase of the expansion (after the laser pulse). This fact is not included in our comparison, which means that Θ_{el} is probably larger in the reality (up to 30 degrees [85]).

| Physical quantity | Z-Petawatt | LULI | PHELIX |
|--|------------------------------------|-----------------------------------|------------------------------------|
| Pulse duration | 480 fs | 350 fs | 500 fs |
| Laser intensity | $9.2 \cdot 10^{23} \text{ W/m}^2$ | $3 \cdot 10^{23} \text{ W/m}^2$ | $5.6 \cdot 10^{23} \text{ W/m}^2$ |
| Normalized laser amplitude (a_L) | 8.2 | 4.6 | 6.4 |
| Spot-size (FWHM) | $5 \mu\text{m}$ | $8 \mu\text{m}$ | $15 \mu\text{m}$ |
| Target thickness | $25 \mu\text{m}$ | $15 \mu\text{m}$ | $25 \mu\text{m}$ |
| Hot electron temperature (T_h) | 1.38 MeV | 766 keV | 1.08 MeV |
| Electron spread-angle (Θ_{el} , degrees) | 16 | 16.5 | 6.8 |
| Hot electron density (n_{h0}) | $2.2 \cdot 10^{26} \text{ m}^{-3}$ | $12 \cdot 10^{26} \text{ m}^{-3}$ | $5.9 \cdot 10^{26} \text{ m}^{-3}$ |

Table 6.2: Parameters of experiments and the fitting values

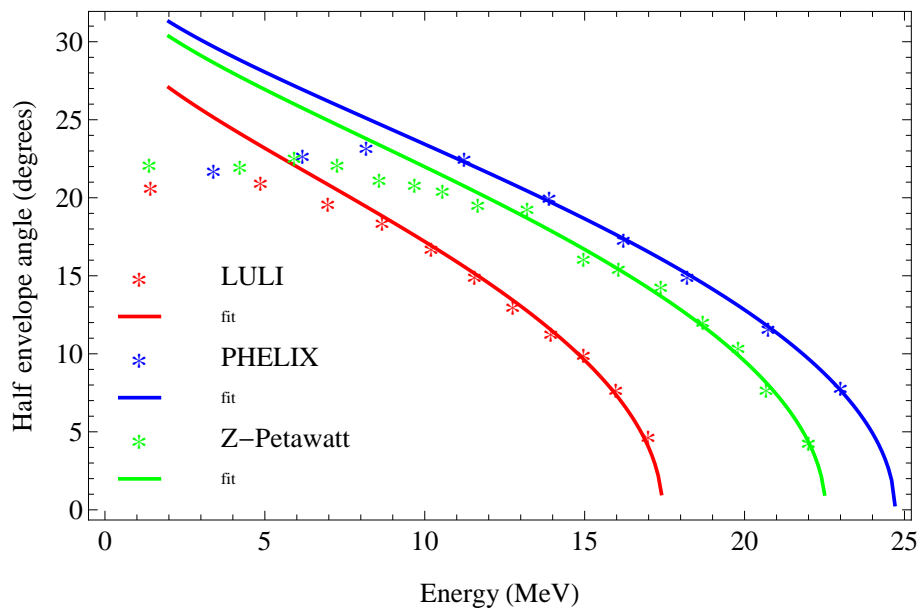


Figure 6.24: The analytical expression Eq. 6.12 fitted to the experimental data using the parameters shown in table 6.2.

7 Conclusions

The aim of this work was the numerical study of the TNSA mechanism by the means of a particle-in-cell code. Our tool was the VORPAL [56] plasma simulation software, which is a fully relativistic electro-magnetic PIC code. Simulation data were analyzed and compared to analytical models and scaling laws. First we studied the interaction of a laser pulse with a pure proton plasma and the consequent plasma expansion in 1D. In the next step the double layer structure of the target has been considered, which is more realistic.

We tested the convergence and stability of the 2D simulations in VORPAL for our physical problem. Because of the small scale lengths in the high density plasma the TNSA simulation in general requires very high resolution. Therefore we had to find what are the acceptable numerical parameters, which lead to reliable, but not too time consuming simulations.

In the first part of our work we focused on the 1D view of the acceleration. First the laser-plasma interaction was studied. We found that the energy absorption of the laser pulse is only about 20 % and it slightly depends on the preplasma scale-length. The mass of the ions have an impact on the hot electron temperature. If the ions are heavier, then the hot electrons can achieve higher temperature, because they do not loose energy at the laser-plasma interface (front side of the target). With protons the lower hot electrons temperature results in a weaker acceleration at the rear side (TNSA) [2]. However, by using protons the time scale of acceleration is rather short, thus the simulations need less time.

The consequent acceleration from a purely proton plasma was studied and compared with the isothermal plasma expansion theory [9] showing an acceptable agreement. The hot electron temperature and density are not constant during the laser pulse, therefore it is difficult to compare the process to an idealized model, where everything is fixed and only hot electrons are included. We have shown that the hot electrons become co-moving with the ions after some cooling time, which means that their mean velocity is higher the thermal velocity.

Because of the uncertainty of the hot electron parameters, the plasma expansion simulation was considered a better option. In these simulations a thermal plasma is initialized with well-known electron parameters and with one (protons) or two ion species (protons and heavy ions arranged in a layered structure). In the simulations with only protons we found a perfect agreement between the results and the model [9] in the isothermal phase of the expansion. The difference between the one- and two-temperature (with hot and cold electrons) plasma has been studied and the expansion model could be generalized for the two-temperature case.

The next step was the investigation of a more realistic plasma, with two-ion species: bulk heavy target and a thin proton layer (contamination layer in the reality). We could obtain a semi-analytical equilibrium distribution of the electrons around the plasma surface, where they trigger the charge-separation. By loading the electrons into the simulation with a density according to these expressions, we start with an equilibrium electric field and we skip the initial perturbations which would occur if we started with a step-like density profile. The electrons have a non-relativistic Maxwell momentum distribution with a given temperature.

The longitudinal energy spectrum and velocity phase-space has been investigated in a dependence on the proton layer thickness. A new dimensionless parameter has been introduced, the

normalized layer thickness (D), which characterizes the layer and helps to identify the acceleration regime. If the layer is very thin ($D \ll 1$) the quasi-static acceleration (QSA) takes place in the Debye sheath [46], but if the layer is thick ($D \gg 1$) the protons get accelerated via plasma expansion. In the latter the maximum energy scales as the square of the time logarithm, while in the QSA regime it scales as the logarithm of the length of the electron sheath, which depends on the maximum hot electron energy.

With this plasma expansion simulation technique we could get an insight into the longitudinal dynamics of the proton layer detached from the heavy target. By monitoring the self-consistent electric field we could derive an analytical expression for the energy conversion from the electrons to the protons as a function of layer thickness and electron parameters. The simulation show that after detachment a potential-drop evolves between the proton bunch and the heavy target, which stays constant after the bunch is neutralized. The electrons with energy smaller than this potential-drop can not contribute to the acceleration, which determines the amount of energy transferred to the protons, if the electron energy spectrum is known.

The dependence of the proton beam properties on the layer thickness has been studied also in the 2D Cartesian geometry using a Gaussian laser pulse. We need the source of hot electrons, because they can escape transversally from the hot spot, not like in 1D. A series of 2D simulations have been performed in order to investigate the transverse acceleration in a dependence on D . We found that the longitudinal acceleration is similar to the 1D case. Due to numerical limitations the thin layer regime could not be simulated accurately, because the electric field profile inside the target has an extremely small scale length. In 2D we observed a more constant hot electron density, because they can move and escape transversally and are replaced by new laser-produced electrons with a constant flux. Their longitudinal temperature basically depends on the laser pulse shape (Gaussian), which is time-dependent, but initially it also stays constant.

In the transversal dimension the acceleration has opposite direction in the two extreme cases. For $D \ll 1$ the protons feel the space-charge field created by the hot electron cloud, which accelerates them towards the center. If $D \gg 1$ the quasi-neutral proton plasma expands, where the peak electric field at the Gaussian proton front has a transversal component proportional to the tangent of the proton surface. This field accelerates the protons outwards. In both cases the focusing force inversely proportional to the width of the hot-spot. In the intermediate regime there is a layer thickness for which the divergence of the protons is minimal. The large divergence and the exponential longitudinal energy spectrum measured in experiments can not be explained in the thin layer regime, therefore in particular for the thick layers we derived a simple envelope model which describes the 2D plasma expansion in the case of hot-spot-width much larger than the hot electron Debye-length. This analytical model shows good agreement with the simulation and the transverse beam parameters can be calculated.

The model is applied also for the experimental measurements and we found that by using realistic fitting parameters the energy resolved divergence can be reasonably well reproduced in the high energy limit, close to the center of the Debye-sheath. The width of the Gaussian hot electron density profile and the its absolute maximum value determine the divergence and the cut-off energy respectively. Only these two parameters are needed to perform the fitting. The temperature can be assumed to be uniform in space and its value is estimated [65], while for the acceleration time we can take the well-known and widely used relation: 1.3 times the laser pulse duration.

The energy conversion in higher dimensions is lower because the hot electrons can escape transversally.

The study of the TNSA using PIC simulation codes can help in the optimization of the laser and target parameters in order to achieve more efficient acceleration and better bunch beam parameters. According to our study, once the layer parameters are known the energy conversion can be estimated and the divergence can be understood. By extending our 2D model to 3D we can obtain the full velocity phase-space and density distribution of the proton bunch, which makes possible to connect the third and fourth stages of the LIGHT project, as it is illustrated in Fig. 1.5.

List of symbols

| | |
|------------------|--|
| α | Correction factor of the electron distribution inside the plasma |
| $\bar{\gamma}$ | Cycle average gamma factor of the laser, $\bar{\gamma} = \sqrt{1 + a_L^2/2}$ |
| χ_f | The normalized proton front position, $\chi_f = x_f/\lambda_D$ |
| Δx | Grid size |
| δ_E | Scale length of the electric field inside the plasma |
| ϵ_0 | Electric permittivity in vacuum |
| ϵ_{max} | Maximum electron energy normalized to T_h |
| λ_D | Hot electron Debye-length, $\lambda_D = \sqrt{\epsilon_0 T_h / (q_e^2 n_{h0})}$ |
| λ_L | Laser wave length |
| λ_{Dc} | Cold electron Debye-length, $\lambda_{Dc} = \sqrt{\epsilon_0 T_c / (q_e^2 n_{c0})}$ |
| ω_L | Laser frequency |
| ω_{pi} | Ion plasma frequency, used for the protons, $\omega_{pi} = C_s / \lambda_D = \sqrt{n_{h0} q_e^2 / (m_p \epsilon_0)}$ |
| ω_p | Electron plasma frequency, $\omega_p = \sqrt{n_e q_e^2 / m_e \epsilon_0}$ |
| Φ | Electric potential |
| Φ_d | Potential-drop between the bulk plasma and the detached proton layer |
| Φ_p | Ponderomotive potential, $\Phi_p = mc^2 (\sqrt{1 + a_L^2/2} - 1)$ |
| Σ | The normalized RMS width of the hot spot, $\Sigma = \sigma / \lambda_D$ |
| σ | Standard deviation of the Gaussian hot electron density profile |
| σ_L | σ of the transversal intensity profile of the laser |
| τ | Normalized time, $\tau = \omega_{pi} t$ |
| τ_{acc} | Normalized acceleration time, $\tau_{acc} = \omega_{pi} t_{acc}$ |
| Θ | Envelope opening angle of the protons |
| v | The normalized transversal coordinate in 2D, $v = y / \sigma$ |
| φ | Normalized electric potential, $\varphi = q_e \Phi / T_h$ |
| φ_0 | Normalized electric potential at the plasma surface |

| | |
|-----------------|--|
| φ_{max} | The lowest normalized potential value at the end of the Debye-sheath |
| a | A parameter of the 2T plasma, which defines the speed of the rarefaction wave, $a = \sqrt{1 + n_{c0}/n_{h0}}/r$ |
| a_L | Normalized laser electric field amplitude, $a_L^2 = \frac{I_{L0}[W/cm^2]\lambda_L^2[\mu m^2]}{1.37 \cdot 10^{18}}$ |
| C | Energy conversion from electrons to protons |
| c | Speed of light |
| C_s | Acoustic speed of the protons in a 1T plasma, $C_s = \sqrt{T_h/m_p}$ |
| C_{s2} | Velocity of the rarefaction wave in a 2T plasma, $C_{s2} = aC_s$ |
| C_{thick} | Energy conversion from electrons to protons in the thick layer regime |
| C_{thin} | Energy conversion from electrons to protons in the thin layer regime |
| D | Normalized layer thickness, $D = \sqrt{1 + \frac{n_{c0}T_h}{n_{h0}T_c} \frac{d}{\lambda_D}}$ |
| d | Thickness of the proton layer |
| E | Electric field |
| E_0 | Peak electric field at the plasma surface, $E_0 = \sqrt{n_{h0}T_h/\epsilon_0}$ |
| E_f | Peak electric field at the ion front |
| I_{L0} | The peak laser intensity |
| L_e | Length of the Debye-sheath |
| L_n | Density scale length |
| L_p | Total length of the plasma slab |
| l_s | Laser skin depth |
| L_t | Target thickness |
| m_e | Electron mass |
| n_0 | Plasma density, $n_0 = n_{h0} + n_{c0}$ |
| n_p | Proton density |
| n_{c0} | Cold electron density inside the plasma |
| n_{cr} | Critical density |
| n_{h0} | Hot electron density, inside the plasma |
| P_e | Electron pressure |
| q_e | Elementary charge, in the figures its symbol is e . |

| | |
|-----------------|---|
| r | A parameter of the 2T plasma, which defines the scale length potential profile inside the plasma, $r = \sqrt{1 + (n_{c0}/n_{h0})(T_h/T_c)}$ |
| S_{FWHM} | Spot size of the laser |
| T_c | Cold electron temperature |
| T_h | Hot electron temperature |
| t_L | Laser pulse duration |
| t_{acc} | Acceleration time in an expanding plasma, $t_{acc} = L_p/C_s$ |
| t_{acc}^{1D} | Acceleration time in the expansion of a plasma heated by a laser, 1D case, $t_{acc}^{1D} = t_L + \frac{L_t}{2C_s}$ |
| t_{acc}^{exp} | Effective acceleration time used in the experiments, $t_{acc}^{exp} = 1.3t_L$ |
| u | Velocity of the proton shock in the hole boring |
| v_f | Proton front velocity |
| v_p | Proton velocity |
| v_{th} | Thermal velocity of electrons |
| W | Kinetic energy of the protons |
| W_e | Kinetic energy of the electrons |
| x_f | Position of the proton front |

List of figures

| | | |
|------|--|----|
| 1.1 | Sketch of the TNSA process. | 9 |
| 1.2 | Layout of the Z6 experimental area at the GSI. | 12 |
| 1.3 | A picture of the solenoid used in the experiment. Courtesy of Simon Busold. | 13 |
| 1.4 | Experimentally measured proton spectrum | 14 |
| 1.5 | Diagram of the different stages of the LIGHT project. | 16 |
| 2.1 | Potential and electron density profiles around the plasma surface | 25 |
| 2.2 | Electric field in the charge separation | 25 |
| 2.3 | Electric field profiles for different layer density | 27 |
| 2.4 | Density profile of the expanding plasma | 29 |
| 2.5 | Comparison of the peak electric field at the proton front in 1T and 2T plasma | 30 |
| 2.6 | Electron cooling during plasma expansion | 31 |
| 2.7 | Rarefaction shock solutions | 32 |
| 3.1 | Sketch of one cycle of a PIC simulation. | 35 |
| 3.2 | Time integration scheme of the field and particle quantities in an EM simulation. | 37 |
| 3.3 | The dispersion curve of an EM wave on the grid for different time steps. | 38 |
| 3.4 | The layout of a 2D simulation box, including the boundaries. | 39 |
| 3.5 | The performance of the parallel 2D simulation as a function of the number of nodes. | 40 |
| 3.6 | Simulation convergence with changing Δx and PPC | 41 |
| 3.7 | Cherenkov radiation in simulation | 42 |
| 3.8 | Convergence study of the simulation of a laser-plasma interaction | 42 |
| 3.9 | The hot electron temperature over time for different spatial resolutions in 1D simulation. | 43 |
| 3.10 | A sketch to illustrate the possibilities of increasing the cold electron Debye-length. | 44 |
| 4.1 | Velocity phase-space of electrons (left) at 51 fs and of the protons (right) at 178 fs from the simulation with the Pulse 1. | 46 |
| 4.2 | The maximum proton velocity during acceleration for Pulse 1 (left) and Pulse 2 (right). The dashed lines represent Eq. (2.27). | 47 |
| 4.3 | The energy spectrum of protons for Pulse 1 (left) and Pulse 2 (right). The full lines represent Eq. (2.28) and (2.29). | 48 |
| 4.4 | Electron energy spectrum and cooling | 48 |
| 4.5 | Spatial profile of the thermal speed of hot electrons | 49 |
| 4.6 | Time evolution of the hot electron temperature and density during the laser-plasma interaction with Pulse 2. | 50 |
| 4.7 | Intensity profile of the laser pulses: constant Eq. (4.9) -black, Gaussian Eq. (4.7) -red, shifted Gaussian Eq. (4.8) -blue. | 51 |

| | | |
|------|--|----|
| 4.8 | Left: The time evolution of the hot electron density and temperature. Right: Proton front velocity compared to Eq. 2.27. The color legend is the same as in Fig. 4.7. | 52 |
| 5.1 | Double layer concept | 54 |
| 5.2 | Proton front velocity in the extreme cases | 56 |
| 5.3 | 1T vs 2T plasma expansion, density and velocity profiles | 57 |
| 5.4 | Effect of the layer thickness on the proton energy spectrum | 57 |
| 5.5 | Left: Density profiles of electrons (dotted line) and protons (full line). Right: The corresponding electric field. Simulation parameters are: $D = 1$, $n_p/n_{h0} = 4$, $T_h/T_c = 20$ | 58 |
| 5.6 | Time evolution of the potential and the final value of the potential-drop | 58 |
| 5.7 | Potential-drop as a function of layer thickness | 59 |
| 5.8 | Energy conversion from hot electrons to protons | 60 |
| 5.9 | Energy spectrum of electrons from the laser-plasma simulation and plasma expansion simulation, where the analytical momentum distribution was used, Eq (5.10). | 61 |
| 5.10 | Time evolution of the mean kinetic energy of the hot electrons when a laser interacts with a proton plasma (black) and with an immobile ion plasma (red). | 62 |
| 5.11 | Energy conversion in a laser-plasma interaction | 63 |
| 6.1 | The longitudinal electric field behind the target for $D = 0.5$ (left), $D = 6$ (middle) and $D = 50$ (right). The rear surface is at $x = 9\mu\text{m}$ | 65 |
| 6.2 | The longitudinal (upper row) and transversal (lower row) components of the proton velocity for $D = 0.5$ (left column), $D = 6$ (middle column) and $D = 50$ (right column). The rear surface is at $x = 9\mu\text{m}$ | 66 |
| 6.3 | Left: The average and RMS angle (in radian) at the proton front at different times. Right: The time evolution of the RMS angle for different layer thicknesses. | 67 |
| 6.4 | Simulation with immobile ions showing the electric fields: the longitudinal (upper row) and transversal (lower row) components at 45 fs (left) and at 76 fs (right). The rear surface is at $x = 10\mu\text{m}$ | 68 |
| 6.5 | The longitudinal (red line), transversal (black line) temperature and density (blue line) of hot electrons. The plots are made for the same time instances as in Fig. 6.4. | 68 |
| 6.6 | Electric potential in a QSA and the resulting proton velocity phase-space | 69 |
| 6.7 | Comparison of the longitudinal and transversal velocity components of the protons at the outer surface of the expanding plasma at the end of the laser pulse duration. | 70 |
| 6.8 | The self-similar electric field (E_0) calculated from the measured hot electron parameters during the acceleration. The green dashed line shows the analytical fit Eq. (6.2), with $\sigma = 4.6\mu\text{m}$ | 71 |
| 6.9 | The longitudinal (left) and transversal (right) electric field in a 2D TNSA simulation with a thick layer, $D = 50$ | 72 |
| 6.10 | Longitudinal and transversal velocities for Sim1 at the time moments: 50, 100, 200 fs. | 74 |

| | |
|---|----|
| 6.11 Longitudinal and transversal velocities for Sim2 at the time moments: 80, 200, 320 fs. | 74 |
| 6.12 Longitudinal and transversal velocities for Sim3 at the time moments: 90, 150, 240 fs. | 75 |
| 6.13 Direction of the proton velocity vector inside the plasma | 76 |
| 6.14 Velocity phase-space of protons from Sim3 at $\omega_{pi}t = 19.2$. In the left plot the analytical prediction Eqs. (6.7,6.9) is shown and in the right one is the simulation result. | 76 |
| 6.15 Energy-dependent envelope angle, model and simulation | 77 |
| 6.16 Transversal velocity at different longitudinal positions | 77 |
| 6.17 Contour plot of the opening angle | 78 |
| 6.18 Comparison of the normal (left) and shifted Gaussian (right) pulses in 2D. | 78 |
| 6.19 Comparison of the simulation results with 2 different laser pulses. | 79 |
| 6.20 Comparison of the proton velocity with 2 different laser pulses. | 79 |
| 6.21 Energy conversion in 2D | 80 |
| 6.22 The initial longitudinal (left) and radial (right) velocity distribution of protons on the surface. | 81 |
| 6.23 Velocity phase space of protons at the beginning (red) and 2 ps later (black). | 81 |
| 6.24 The analytical expression Eq. 6.12 fitted to the experimental data using the parameters shown in table 6.2. | 83 |

Bibliography

- [1] S. C. Wilks, A. B. Langdon, T. E. Cowan, M. Roth, M. Singh, S. Hatchett, M. H. Key, D. Pennington, A. MacKinnon, and R. A. Snavely. Energetic proton generation in ultra-intense laser-solid interactions. *Physics of Plasmas*, 8(2):542–549, August 2001.
- [2] S. C. Wilks, W. L. Kruer, M. Tabak, and A. B. Langdon. Absorption of ultra-intense laser pulses. *Physical Review Letters*, 69(9):1383–1386, August 1992.
- [3] J. Fuchs, Y. Sentoku, S. Karsch, J. Cobble, P. Audebert, A. Kemp, A. Nikroo, P. Antici, E. Brambrink, A. Blazevic, E. M. Campbell, J. C. Fernández, J.-C. Gauthier, M. Geissel, M. Hegelich, H. Pépin, H. Popescu, N. Renard-LeGalloudec, M. Roth, J. Schreiber, R. Stephens, and T. E. Cowan. Comparison of laser ion acceleration from the front and rear surfaces of thin foils. *Phys. Rev. Lett.*, 94:045004, Feb 2005.
- [4] J. Fuchs, P. Antici, E. d’Humières, E. Lefebvre, M. Borghesi, E. Brambrink, C. A. Cecchetti, M. Kaluza, V. Malka, M. Manclossi, S. Meyroneinc, P. Mora, J. Schreiber, T. Toncian, H. Pépin, and P. Audebert. Laser-driven proton scaling laws and new paths towards energy increase. *Nature Physics*, 2:48–54, December 2005.
- [5] M. Tampo, S. Awano, and et al. P. R. Bolton an K. Kondo. Correlation between laser accelerated mev proton and electron beams using simple fluid model for target normal sheath acceleration. *Physics of Plasmas*, 17(7):073110– 073115, July 2010.
- [6] M. Kaluza, J. Schreiber, M. I. K. Santala, G. D. Tsakiris, K. Eidmann, J. Meyer-ter Vehn, and K. J. Witte. Influence of the laser prepulse on proton acceleration in thin-foil experiments. *Phys. Rev. Lett.*, 93:045003, Jul 2004.
- [7] T. Grismayer and P. Mora. Influence of a finite initial ion density gradient on plasma expansion into a vacuum. *Physics of Plasmas*, 13(3):032103–032110, May 2006.
- [8] T. Ceccotti, A. Lévy, H. Popescu, F. Réau, P. D’Oliveira, P. Monot, J. P. Geindre, E. Lefebvre, and Ph. Martin. Proton acceleration with high-intensity ultrahigh-contrast laser pulses. *Phys. Rev. Lett.*, 99:185002, Oct 2007.
- [9] P. Mora. Plasma expansion into a vacuum. *Phys. Rev. Lett.*, 90:185002–185006, May 2003.
- [10] Claudio Perego, Alessandro Zani, Dimitri Batani, and Matteo Passoni. Extensive comparison among target normal sheath acceleration theoretical models. *Nuclear Instruments and Methods in Physics Research Section A: Accelerators, Spectrometers, Detectors and Associated Equipment*, 653(1):89 – 93, 2011.
- [11] M. Passoni and M. Lontano. Theory of light-ion acceleration driven by a strong charge separation. *Phys. Rev. Lett.*, 101:115001, Sep 2008.

-
- [12] L. Romagnani, J. Fuchs, M. Borghesi, P. Antici, P. Audebert, F. Ceccherini, T. Cowan, T. Grismayer, S. Kar, A. Macchi, P. Mora, G. Pretzler, A. Schiavi, T. Toncian, and O. Willi. Dynamics of electric fields driving the laser acceleration of multi-mev protons. *Phys. Rev. Lett.*, 95:195001, Oct 2005.
- [13] O Jäckel, J Polz, S M Pfotenhauer, H-P Schlenvoigt, H Schwoerer, and M C Kaluza. All-optical measurement of the hot electron sheath driving laser ion acceleration from thin foils. *New Journal of Physics*, 12(10):103027, October 2010.
- [14] P. Antici, J. Fuchs, M. Borghesi, L. Gremillet, T. Grismayer, Y. Sentoku, E. d’Humières, C. A. Cecchetti, A. Mančić, A. C. Pipahl, T. Toncian, O. Willi, P. Mora, and P. Audebert. Hot and cold electron dynamics following high-intensity laser matter interaction. *Phys. Rev. Lett.*, 101:105004, Sep 2008.
- [15] B. M. Hegelich, B. J. Albright, J. Cobble, K. Flippo, S. Letzring, M. Paffett, H. Ruhl, J. Schreiber, R. K. Schulze, and J. C. Fernández. Laser acceleration of quasi-monoenergetic mev ion beams. *Nature Physics*, 439:441–444, January 2006.
- [16] H. Schwoerer, S. Pfotenhauer, O. Jäckel, K.-U. Amthor, B. Liesfeld, W. Ziegler, R. Sauerbrey, K. W. D. Ledingham, and T. Esirkepov. Laser-plasma acceleration of quasi-monoenergetic protons from microstructured targets. *Nature Physics*, 439:445–448, January 2006.
- [17] G. Hoffmeister, C. Bellei, K. Harres, D. Ivanov, D. Kraus, A. Pelka, B. Rethfeld, G. Schaubmann, and M. Roth. Influence of fs-laser desorption on target normal sheath accelerated ions. *Phys. Rev. ST Accel. Beams*, 16:041304, Apr 2013.
- [18] B. Zielbauer et al. Project report: Light- laser ion generation, handling and transport.
- [19] Frank Nürnberg. Phd thesis: Laser-accelerated proton beams as a new particle source, September 2010.
- [20] I. Alber I. Hofmann, editor. *Laser accelerated ions and their potential for therapy accelerators*, Jun 6-9, 2009.
- [21] F. Nürnberg, M. Schollmeier, E. Brambrink, A. Blazevic, D. C. Carroll, K. Flippo, D. C. Gautier, M. Geissel, K. Harres, B. M. Hegelich, O. Lundh, K. Markey, P. McKenna, D. Neely, J. Schreiber, and M. Roth. Radiochromic film imaging spectroscopy of laser-accelerated proton beams. *Review of Scientific Instruments*, 80(3):033301, 2009.
- [22] M. Schollmeier, K. Harres, F. Nurnberg, A. Blazevic, P. Audebert, E. Brambrink, J. C. Fernandez, K. A. Flippo, D. C. Gautier, M. Geissel, B. M. Hegelich, J. Schreiber, and M. Roth. Laser beam-profile impression and target thickness impact on laser-accelerated protons. *Physics of Plasmas*, 15(5):053101, 2008.
- [23] Marius Schollmeier, M. Roth, A. Blazevic, E. Brambrink, J.A. Cobble, J.C. Fernandez, K.A. Flippo, D.C. Gautier, D. Habs, K. Harres, B.M. Hegelich, T. Hessling, D.H.H. Hoffmann, S. Letzring, F. Nuernberg, G. Schaubmann, J. Schreiber, and K. Witte. Laser ion acceleration with micro-grooved targets. *Nuclear Instruments and Methods in Physics Research Section A: Accelerators, Spectrometers, Detectors and Associated Equipment*, 577(1-2):186 – 190, 2007.
- [24] Peter Schmidt. Master thesis: Transport und fokussierung laserbeschleunigter protonstrahlen, October 2012.

-
- [25] O. Deppert, K. Harres, F. Nürnberg, G. Schaumann, M. Schollmeier, and M. Roth. Gsi annual scientific report: Divergence control with optimized targets for laser proton acceleration.
- [26] O. Deppert, K. Harres, F. Nürnberg, S. Busold, V. Bagnoud, G. Schaumann, M. Schollmeier, M. Geissel, D. Neely, and M. Roth. Gsi annual scientific report: Annular shaped laser-accelerated proton beams.
- [27] T. Burriss-Mog, K. Harres, F. Nürnberg, S. Busold, M. Bussmann, O. Deppert, G. Hoffmeister, M. Joost, M. Sobiella, A. Tauschwitz, B. Zielbauer, V. Bagnoud, T. Herrmannsdoerfer, M. Roth, and T. E. Cowan. Laser accelerated protons captured and transported by a pulse power solenoid. *Phys. Rev. ST Accel. Beams*, 14:121301, Dec 2011.
- [28] T. E. Cowan, J. Fuchs, H. Ruhl, A. Kemp, P. Audebert, M. Roth, R. Stephens, I. Barton, A. Blazevic, E. Brambrink, J. Cobble, J. Fernández, J.-C. Gauthier, M. Geissel, M. Hegelich, J. Kaae, S. Karsch, G. P. Le Sage, S. Letzring, M. Manclossi, S. Meyroneinc, A. Newkirk, H. Pépin, and N. Renard-LeGalloudec. Ultralow emittance, multi-mev proton beams from a laser virtual-cathode plasma accelerator. *Phys. Rev. Lett.*, 92:204801, May 2004.
- [29] M. Roth, D. Jung, K. Falk, N. Guler, O. Deppert, M. Devlin, A. Favalli, J. Fernandez, D. Gautier, M. Geissel, R. Haight, C. E. Hamilton, B. M. Hegelich, R. P. Johnson, F. Merrill, G. Schaumann, K. Schoenberg, M. Schollmeier, T. Shimada, T. Taddeucci, J. L. Tybo, F. Wagner, S. A. Wender, C. H. Wilde, and G. A. Wurden. Bright laser-driven neutron source based on the relativistic transparency of solids. *Phys. Rev. Lett.*, 110:044802, Jan 2013.
- [30] D. Richter, N. Saito, P. Steidl, M. Haertig, O. Jaekel, M. Durante, and C. Bert. Gsi annual scientific report: Simulation of uncompensated and gated treatments of a liver cancer patient with scanned carbon ions.
- [31] A. Frank, A. Blažević, P. L. Grande, K. Harres, T. Heßling, D. H. H. Hoffmann, R. Knobloch-Maas, P. G. Kuznetsov, F. Nürnberg, A. Pelka, G. Schaumann, G. Schiwietz, A. Schökel, M. Schollmeier, D. Schumacher, J. Schüttrumpf, V. V. Vatulín, O. A. Vinokurov, and M. Roth. Energy loss of argon in a laser-generated carbon plasma. *Phys. Rev. E*, 81:026401, Feb 2010.
- [32] J. E. Crow, P. L. Auer, and J. E. Allen. The expansion of a plasma into a vacuum. *Journal of Plasma Physics*, 14:65–76, August 1975.
- [33] J. Denavit. Collisionless plasma expansion into a vacuum. *Physics of Fluids*, 22:1384–1393, July 1979.
- [34] S. Betti, F. Ceccherini, F. Cornolti, and F. Pegoraro. Expansion of a finite-size plasma in vacuum. *Plasma Physics and Controlled Fusion*, 47(3):521, February 2005.
- [35] P. Mora. Thin-foil expansion into a vacuum. *Phys. Rev. E*, 72:056401–056406, Nov 2005.
- [36] T. Grismayer, P. Mora, J. C. Adam, and A. Héron. Electron kinetic effects in plasma expansion and ion acceleration. *Phys. Rev. E*, 77:066407–066418, Jun 2008.
- [37] P. Mora and T. Grismayer. Rarefaction acceleration and kinetic effects in thin-foil expansion into a vacuum. *Phys. Rev. Lett.*, 102:145001–145005, April 2009.

-
-
- [38] B. Bezzerides, D. W. Forslund, and E. L. Lindman. Existence of rarefaction shocks in a laser-plasma corona. *Physics of Fluids*, 21:2179–2186, December 1978.
- [39] V T Tikhonchuk, A A Andreev, S G Bochkarev, and V Yu Bychenkov. Ion acceleration in short-laser-pulse interaction with solid foils. *Plasma Physics and Controlled Fusion*, 47(12B):B869, 2005.
- [40] A. Diaw and P. Mora. Rarefaction shock in plasma with a bi-maxwellian electron distribution function. *Phys. Rev. E*, 84:036402–036411, Sep 2011.
- [41] A. Diaw and P. Mora. Thin-foil expansion into a vacuum with a two-temperature electron distribution function. *Phys. Rev. E*, 86:026403–026410, Aug 2012.
- [42] A. P. L. Robinson, A. R. Bell, and R. J. Kingham. Effect of target composition on proton energy spectra in ultraintense laser-solid interactions. *Phys. Rev. Lett.*, 96:035005–035009, Jan 2006.
- [43] V. Yu. Bychenkov, V. N. Novikov, D. Batani, V. T. Tikhonchuk, and S. G. Bochkarev. Ion acceleration in expanding multispecies plasmas. *Physics of Plasmas*, 11(6):3242–3251, May 2004.
- [44] B. J. Albright, L. Yin, B. M. Hegelich, Kevin J. Bowers, T. J. T. Kwan, and J. C. Fernández. Theory of laser acceleration of light-ion beams from interaction of ultrahigh-intensity lasers with layered targets. *Phys. Rev. Lett.*, 97:115002–115006, Sep 2006.
- [45] A. V. Brantov, V. T. Tikhonchuk, V. Yu. Bychenkov, and S. G. Bochkarev. Laser-triggered ion acceleration from a double-layer foil. *Physics of Plasmas*, 16(4):043107–043115, April 2009.
- [46] Maurizio Lontano and Matteo Passoni. Electrostatic field distribution at the sharp interface between high density matter and vacuum. *Physics of Plasmas*, 13(4):042102–042109, April 2006.
- [47] M. Passoni and M. Lontano. One-dimensional model of the electrostatic ion acceleration in the ultraintense laser–solid interaction. *Laser and Particle Beams*, 22:163–169, May 2004.
- [48] M. Passoni, V. T. Tikhonchuk, M. Lontano, and V. Yu. Bychenkov. Charge separation effects in solid targets and ion acceleration with a two-temperature electron distribution. *Phys. Rev. E*, 69:026411, Feb 2004.
- [49] Holger Schmitz. Target normal sheath acceleration sheath fields for arbitrary electron energy distribution. *Physics of Plasmas*, 19(8):083115, August 2012.
- [50] J. Schreiber, F. Bell, F. Grüner, U. Schramm, M. Geissler, M. Schnürer, S. Ter-Avetisyan, B. M. Hegelich, J. Cobble, E. Brambrink, J. Fuchs, P. Audebert, and D. Habs. Analytical model for ion acceleration by high-intensity laser pulses. *Phys. Rev. Lett.*, 97:045005, July 2006.
- [51] Emmanuel d’Humières, Erik Lefebvre, Laurent Gremillet, and Victor Malka. Proton acceleration mechanisms in high-intensity laser interaction with thin foils. *Physics of Plasmas*, 12(6):062704–062717, Jun 2005.

-
- [52] M. Carrié, E. Lefebvre, A. Flacco, and V. Malka. Influence of subpicosecond laser pulse duration on proton acceleration. *Physics of Plasmas*, 16(5):053105–053112, May 2009.
- [53] A. Flacco, F. Sylla, M. Veltcheva, M. Carrié, R. Nuter, E. Lefebvre, D. Batani, and V. Malka. Dependence on pulse duration and foil thickness in high-contrast-laser proton acceleration. *Phys. Rev. E*, 81:036405, Mar 2010.
- [54] E. d’Humieres, A. Brantov, V. Yu. Bychenkov, and V. T. Tikhonchuk. Optimization of laser-target interaction for proton acceleration. *Physics of Plasmas*, 20(2):023103, 2013.
- [55] Yong sheng Huang, Xiao fei Lan, Xiao jiao Duan, and Zhi xin Tan et al. Hot-electron recirculation in ultraintense laser pulse interactions with thin foils. *Physics of Plasmas*, 14(10):103106–103112, Oct 2007.
- [56] C. Nieter and J. R. Cary. Vorpal: a versatile plasma simulation code. *Journal of Computational Physics*, 196(2):448 – 473, 2004.
- [57] Paul Gibbon. *Short Pulse Laser Interactions with Matter*. Imperial College Press, 2007.
- [58] Peter Mulser and Dieter Bauer. *High Power Laser-Matter Interaction*, volume 238 of 238. 2010.
- [59] F. Brunel. Not-so-resonant, resonant absorption. *Phys. Rev. Lett.*, 59:52–55, Jul 1987.
- [60] F. Brunel. Anomalous absorption of high intensity subpicosecond laser pulses. *Physics of Fluids*, 31(9):2714–2719, 1988.
- [61] V. S. Rastunkov and V. P. Krainov. Electron stochastic heating in the interaction of a short laser pulse with overdense plasma. *Laser Physics*, 15(2):262–267, 2005.
- [62] F. N. Beg, A. R. Bell, A. E. Dangor, C. N. Danson, A. P. Fews, M. E. Glinsky, B. A. Hammel, P. Lee, P. A. Norreys, and M. Tatarakis. A study of picosecond laser–solid interactions up to 10^{19} W/cm². *Physics of Plasmas*, 4(2):447–457, 1997.
- [63] M. G. Haines, M. S. Wei, F. N. Beg, and R. B. Stephens. Hot-electron temperature and laser-light absorption in fast ignition. *Phys. Rev. Lett.*, 102:045008, Jan 2009.
- [64] Erik Lefebvre and Guy Bonnaud. Nonlinear electron heating in ultrahigh-intensity-laser–plasma interaction. *Phys. Rev. E*, 55:1011–1014, Jan 1997.
- [65] T. Kluge, T. Cowan, A. Debus, U. Schramm, K. Zeil, and M. Bussmann. Electron temperature scaling in laser interaction with solids. *Phys. Rev. Lett.*, 107:205003, Nov 2011.
- [66] M. Sherlock. Universal scaling of the electron distribution function in one-dimensional simulations of relativistic laser-plasma interactions. *Physics of Plasmas*, 16(10):103101, 2009.
- [67] Thomas Kiefer, Theodor Schlegel, and Malte C. Kaluza. Plasma expansion into vacuum assuming a steplike electron energy distribution. *Phys. Rev. E*, 87:043110, Apr 2013.
- [68] W. D. Jones, A. Lee, S. M. Glemann, and H. J. Doucet. Propagation of ion-acoustic waves in a two-electron-temperature plasma. *Phys. Rev. Lett.*, 35:1349–1352, Nov 1975.

-
- [69] Y. Sentoku, T. E. Cowan, A. Kemp, and H. Ruhl. High energy proton acceleration in interaction of short laser pulse with dense plasma target. *Physics of Plasmas*, 10(5):2009–2015, 2003.
- [70] J. Denavit. Absorption of high-intensity subpicosecond lasers on solid density targets. *Phys. Rev. Lett.*, 69:3052–3055, Nov 1992.
- [71] L. YIN, B. J. ALBRIGHT, B. M. HEGELICH, and J. C. FERNÁNDEZ. GeV laser ion acceleration from ultrathin targets: The laser break-out afterburner. *Laser and Particle Beams*, 24:291–298, 5 2006.
- [72] M Shoucri, B Afeyan, and M Charbonneau-Lefort. Numerical simulation for ion acceleration in an intense laser wave incident on an overdense plasma. *Journal of Physics D: Applied Physics*, 41(21):215205, 2008.
- [73] B. Qiao, M. Zepf, M. Borghesi, B. Dromey, M. Geissler, A. Karmakar, and P. Gibbon. Radiation-pressure acceleration of ion beams from nanofoil targets: The leaky light-sail regime. *Phys. Rev. Lett.*, 105:155002, Oct 2010.
- [74] Estelle Cormier-Michel, B. A. Shadwick, C. G. R. Geddes, E. Esarey, C. B. Schroeder, and W. P. Leemans. Unphysical kinetic effects in particle-in-cell modeling of laser wakefield accelerators. *Phys. Rev. E*, 78:016404, Jul 2008.
- [75] C. K. Birdsall and A. B. Langdon. *Plasma physics via computer simulation*. Imperial College Press, 1991.
- [76] Andrew D. Greenwood, Keith L. Cartwright, John W. Luginsland, and Ernest A. Baca. On the elimination of numerical cerenkov radiation in pic simulations. *Journal of Computational Physics*, 201(2):665 – 684, 2004.
- [77] A. A. Andreev, K. Yu. Platonov, T. Okada, and S. Toraya. Nonlinear absorption of a short intense laser pulse in a nonuniform plasma. *Physics of Plasmas*, 10(1):220–226, 2003.
- [78] N. Sinenian, G. Fiksel, J. A. Frenje, C. G. Freeman, M. J.-E. Manuel, D. T. Casey, P. M. Nilson, C. Stoeckl, W. Theobald, D. D. Meyerhofer, and R. D. Petrasso. Heavy-ion emission from short-pulse laser-plasma interactions with thin foils. *Physics of Plasmas*, 19(9):093118, 2012.
- [79] Matthew Allen, Pravesh K. Patel, Andrew Mackinnon, Dwight Price, Scott Wilks, and Edward Morse. Direct experimental evidence of back-surface ion acceleration from laser-irradiated gold foils. *Phys. Rev. Lett.*, 93:265004, Dec 2004.
- [80] David Cubero, Jesús Casado-Pascual, Jörn Dunkel, Peter Talkner, and Peter Hänggi. Thermal equilibrium and statistical thermometers in special relativity. *Phys. Rev. Lett.*, 99:170601, Oct 2007.
- [81] E. Brambrink, J. Schreiber, T. Schlegel, P. Audebert, J. Cobble, J. Fuchs, M. Hegelich, and M. Roth. Transverse characteristics of short-pulse laser-produced ion beams: A study of the acceleration dynamics. *Phys. Rev. Lett.*, 96:154801, Apr 2006.

-
-
- [82] Andreas J. Kemp, J. Fuchs, Y. Sentoku, V. Sotnikov, M. Bakeman, P. Antici, and T. E. Cowan. Emittance growth mechanisms for laser-accelerated proton beams. *Phys. Rev. E*, 75:056401, May 2007.
- [83] Marius S. Schollmeier. Phd thesis: Optimization and control of laser-accelerated proton beams, December 2008.
- [84] J. J. Santos, F. Amiranoff, S. D. Baton, L. Gremillet, M. Koenig, E. Martinolli, M. Rabec Le Gloahec, C. Rousseaux, D. Batani, A. Bernardinello, G. Greison, and T. Hall. Fast electron transport in ultraintense laser pulse interaction with solid targets by rear-side self-radiation diagnostics. *Phys. Rev. Lett.*, 89:025001, Jun 2002.
- [85] K. B. Wharton, S. P. Hatchett, S. C. Wilks, M. H. Key, J. D. Moody, V. Yanovsky, A. A. Offenberger, B. A. Hammel, M. D. Perry, and C. Joshi. Experimental measurements of hot electrons generated by ultraintense laser-plasma interactions on solid-density targets. *Phys. Rev. Lett.*, 81:822–825, Jul 1998.

Acknowledgments

I owe many thanks to Prof. Dr. rer. nat. Oliver Boine-Frankenheim for accepting me as a PhD student in his group three years ago and for providing a high-performance plasma simulation code, which led to the results presented in this thesis. It was a great opportunity for me to collect knowledge and experience in scientific work among professional colleagues.

I would like to thank Prof. Dr.-Ing. Thomas Weiland and Dr. Theodor Schlegel for their useful comments and for the discussions during the PhD committee meetings held in every six months at the TEMF.

I address many thanks to the experimental group of Prof. Dr. Markus Roth for giving me measured data when I needed and for the interesting collaboration with Oliver Deppert concerning the PIC simulations at the beginning of my PhD.

I also want to thank Dr. rer. nat. Erion Gjonaj for the fruitful discussions about the physical problem and numerical aspects of the simulations.

Special thanks go to Dr. Vladimir Kornilov, my true advisor, who guided and helped me throughout the years with endless patience and support, showing real interest in my work. Without his advices and supervision this work could not have been carried out.

Finally I would like to thank all of my TEMF and GSI colleagues for being nice to me and listening to all of my questions, problems and helping in answering, solving them in the shortest possible time.

Curriculum vitae

Zsolt Lécz

Born in Romania, Székelyhíd

Birth date: 06. July, 1986



Studies:

- | | |
|-----------|---|
| 2000-2004 | Petőfi Sándor Theoretic High School, branch of study: Nature Science, Székelyhíd |
| 2004-2008 | Bábes-Bolyai University, faculty of physics, Physics-Informatics, Kolozsvár -Bachelor level |
| 2008-2010 | Bábes-Bolyai University, faculty of physics, Computational Physics, Kolozsvár - Master level, in 2009, 5 months abroad study at ATOMKI research center in Debrecen, Hungary |
| 2010-2013 | Technical University of Darmstadt (TUD), PhD student, work at the GSI, accelerator department |

Computer skills:

Operating systems: Windows, Linux

Programming languages: C++, Java, Bash, Assembler

Applications: IDL, Mathematica, MathLab, Microsoft Office, L^AT_EX

Publications, Proceedings, Reports:

Biri, S.; Racz, R.; Imrek, J.; Derzsi, A.; Lecz, Z., Imaging of ECR Plasma by Computer Simulation, Plasma Science, IEEE Transactions on , vol.39, no.11, pp.2474,2475, Nov. 2011, doi: 10.1109/TPS.2011.2160363

Submitted and accepted for publication to Nuclear Inst. and Methods in Physics Research, A: **Z. Lecz**, V. Kornilov, O. Boine-Frankenheim, Target normal sheath acceleration for arbitrary proton layer thickness, Reference Nr.: NIMA-D-13-00401, 2013

Proceedings of IPAC2012, New Orleans, Louisiana, USA: **Z. Lecz**, V. Kornilov, O. Boine-Frankenheim, SIMULATION STUDY OF THE EFFECT OF THE PROTON LAYER THICKNESS ON TNSA, ISBN 978-3-95450-115-1

Proceedings of ICAP2012, Rostock-Warnemünde, Germany: **Z. Lecz**, V. Kornilov, O. Boine-Frankenheim, PIC SIMULATIONS OF LASER ION ACCELERATION VIA TNSA, ISBN 978-3-95450-116-8

GSI SCIENTIFIC REPORT 2011: Simulation study of TNSA from a double-layer target, PHN-ACC-RD-60

GSI SCIENTIFIC REPORT 2010: Simulation study of plasma expansion in the early stage of TNSA, PHN-ACC-RD-55